ETH zürich

Laboratory for Solid State Physics

Annual Report 2013

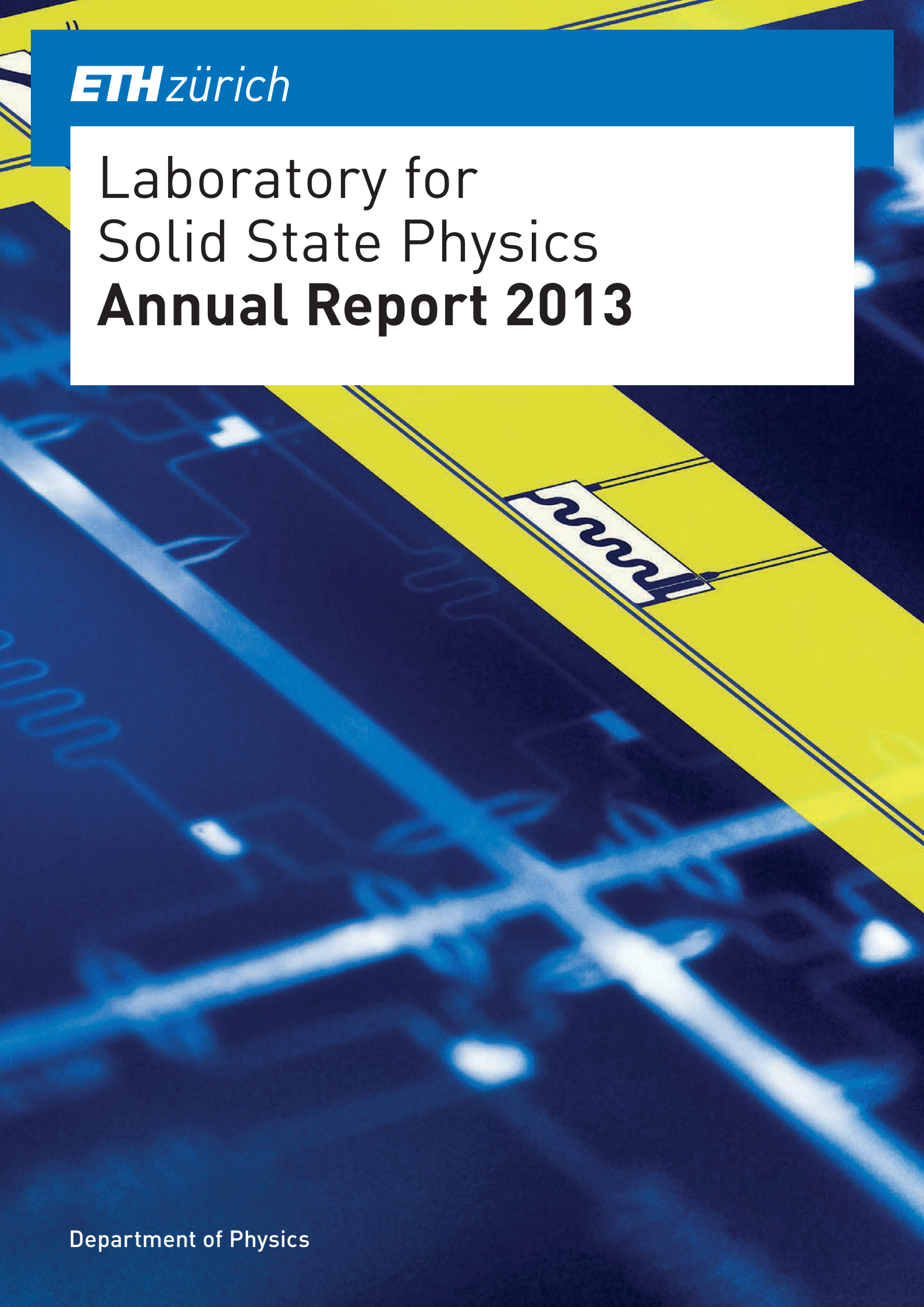

Department of Physics

ANNUAL REPORT
2013

Solid State Physics Laboratory (LFKP)
ETH Zurich

Cover page:

Photograph of optical lithography mask (blue structure in the background) used to fabricate superconducting circuits in which quantum interactions between microwave photons and superconducting qubits (yellow structure in the foreground) are investigated. Similar circuits were used for the experimental demonstration of quantum teleportation in a solid-state system (Steffen et al., Nature 500, 319-322 (2013)).

This annual report was edited by: Philip Moll

PREFACE

The Laboratory for Solid State Physics at ETH Zurich presents its Annual Report for 2013. Our report displays the diverse foci in research, which led to numerous publications in high-ranking journals and presentations at international conferences. The members of the Laboratory are also committed to all aspects of teaching. They strive at conveying the fascination of physics in general and in particular of state-of-the-art solid state physics at all levels. Bachelor and Master level courses were offered for physics students as well as for students of other departments. The portfolio of research directions carried out at LFKP covers a rather wide range including the application and development of novel instruments, the synthesis of highest-quality materials and the fabrication of nanoscale quantum devices as summarized below.

The Ensslin group performed scanning gate experiments on highest-mobility electron gases. Quantum point contacts are standard building blocks of most quantum devices. By scanning a biased metallic tip across a gate defined quantum point contact a rich pattern is observed in such scanning gate images which can be understood in detail by modeling the potential landscape with a network of constriction in parallel and series to each other. Such a setup allows for the investigation of the crossover from ballistic to diffusive transport.

The Quantum Device Lab headed by Andreas Wallraff enjoyed a number of breakthroughs in their research on quantum electronic circuits and their applications in quantum information processing and quantum optics during 2013. Most widely recognized was an experiment in which they teleported quantum information between two distant qubits for the first time in an electronic circuit. The teleportation protocol worked with large success probability at a rate of 10 kHz over a distance of 6 millimeters and is expected to be important future quantum information processing and communication protocols. In the same year photon mediated dipole-dipole coupling between distant artificial atoms was observed in one-dimensional free space and non-abelian geometric phases were used to perform quantum logic gates, both using superconducting quantum electronic circuits. In addition the first Hong-Ou-Mandel experiment was performed with microwave frequency photons, explicitly demonstrating their bosonic nature and also creating possibilities for generating entanglement over larger distances. In the same year Andreas Wallraff received an ERC Advanced Grant to pursue research on quantum communication using microwave photons.

In 2013, one of the most interesting developments in the Zheludev group was the discovery of two subsequent pressure-induced quantum phase transitions in the prototypical organic spin-liquid material PHCC. The first transition was a quantum critical point. It was particularly interesting due to its surprising connection to Higgs boson physics. The second was an unusual incommensurate to commensurate transformation, associated with a Lifshitz point on the phase diagram. These phenomena were found and studied in muon spin rotation experiments under pressures of up to 20 kBar performed at Paul Scherrer Institut. The work was performed by our Master student Mrs. Alexandra Mannig, under the guidance of our senior PhD student Mr. Matthias Thede. For this project, Mrs. Mannig received the ETH medal award. She has now started her PhD research in our group, and has since obtained preliminary data indicating that other prototypical quantum spin liquid compounds may be subject to similar transitions.

The spin physics group of Christian Degen, established in 2011, consolidated its efforts in ultrasensitive scanning probe microscopy. The group demonstrated several pioneering advances using diamond quantum sensors: The magnetic imaging of a nanoscale magnetic tip with < 10 nm spatial resolution, the detection of NMR signals from only ≈ 300 hydrogen atoms, and the implementation of a new quantum sensing protocol with extremely high frequency resolution ($< 0.1\%$). The group's effort in diamond-based sensing is now also supported by DIADEMS, a large-scale collaborative EU ICT grant.

The Batlogg group investigated a wide range of materials, covering novel classes of superconductors, organic semiconductors as well as the growth of lattice-mismatched crystals on pre-patterned substrates. Intrinsic Josephson Junctions as the result of the appropriately layered crystal structure were shown to exist in layered Fe-based superconductors, employing the micro-shaping of crystals by focused ion beam. Organic single crystal FETs with essentially trap free interface and bulk were fabricated, surpassing even the best Si/SiO_2 devices. In a further development of 3D monolithic integration of different semiconductor materials GaAs crystals were grown on Si pillars with a Ge spacer layer.

The Pescia's group demonstrated the existence of yet unsuspected scaling properties of electric field assisted tunneling. In addition, a novel instrument was developed for energy resolved electron scattering with nanometer lateral scale resolution. The collaboration with the group of Andreas Vaterlaus on time resolved experiment at the FLASH facility in Hamburg is continuing. Finally, novel topological properties of spintronic devices when working at finite temperatures were predicted.

The group of physics and education headed by Andreas Vaterlaus installed a new pulsed femto second laser source and did first time resolved Kerr effect measurements on magnetic systems. A model explaining ultrafast demagnetization based on transport was developed to describe earlier measurements and confirmed with recent Kerr effect results. Test tools for our educational project on formative assessment were refined and validated using a larger number of classes. These are online multiple choice tests which allow to monitor the understanding of basic concepts in kinematics.

The coexistence as well as the competition of broken-symmetry ground states, like the prominent examples of charge-density-wave (CDW) and superconductivity (SC), have been ever since at the center of interest in solid state physics. Particularly in low-dimensional materials, the peculiar charge ordering, given by the CDW formation, and SC may be seen as specific quantum states originating from Fermi-surface instabilities, the interplay of which leaded to interesting phase diagrams. Degiorgi's group provided an optical study of both Ni- and Cu-doped $ZrTe_3$, deploying their complete excitation spectrum over a broad spectral range and as a function of temperature. Ni and Cu intercalation of $ZrTe_3$ leaded to the onset of bulk superconductivity at $T_c < T_{CDW}$. The charge dynamics of the CDW state displayed a polarization dependence within the ab-plane and gave evidence for a partial gapping of the Fermi surface along the crystallographic direction parallel to the a-axis. It was observed that the CDW-gap feature persisted at $T < T_c$, so that CDW and that superconductivity coexisted along the a-axis and consequently affected separate regions in the reciprocal space.

The group of Joël Mesot continued its studies on the influence of disorder, frustration and magnetic fields on the properties of one- and two-dimensional spin systems. Magnetic-field controlled soliton-soliton interactions were studied via ^{31}P NMR up to fields of 45 T at the National High Magnetic Field Laboratory (NHMFL) in Tallahassee, USA. Results of measurements probing both the field and temperature dependence of the magnetization and ^{29}Si NMR, complemented by quantum Monte Carlo simulations, were used to demonstrate that the disordered spin-chain compound $BaCu_2SiGeO_7$ adopts a random-singlet ground state. The latter was previously predicted theoretically for a model Hamiltonian describing a so-called random Heisenberg spin chain but had not been identified convincingly by experiment.

The Advanced Semiconductor Quantum Materials group headed by Werner Wegscheider concentrated on the synthesis and investigation of highest-purity III/V As- and Sb-based heterostructures. One highlight in 2013 was the realization of InAs/GaSb combined quantum wells, which represent, as a result of the broken band-alignment in this material system, tunable 2D topological insulators (Tis). Molecular beam epitaxial growth of such structures employing the incorporation of different levels of intentional impurities in the channel region led to the suppression of bulk conduction in the TI region. This is a promising route towards the investigation of helical edge channel transport. Another highlight was the fabrication of a sample which served in collaboration with the Glattli group (CEA Saclay, France) for electron quantum optics experiments using levitons.

The experimental research at the laboratory of solid state physics and our teaching activities benefit from the excellent infrastructure provided by ETH Zurich and in particular by the physics department. We thank the involved people for their dedication and solid support especially in all technical and administrative matters. We very gratefully acknowledge the continuous and substantial support by the Schulleitung of ETH Zurich, but also by the Swiss National Science Foundation, the Commission for Technology and Innovation (KTI), the European Research Council, industrial partners and all other sources.

For preparing this Annual Report, we would like to thank Mrs. Christina Egli and Mr. Ph. Moll for editing the report and Mrs. Amanda Eisenhut for the graphical design. As in the previous year, in order to avoid producing old-fashioned CDs we again simply print a postcard with a QR-Code on it so that last year's report can be easily downloaded.

Zürich, June 2014

Der Vorsteher

Prof. Dr. W. Wegscheider

Contents

Chapter 1

Physics of New Materials

(http://www.pnm.ethz.ch/)

Head
Prof. Dr. B. Batlogg

Academic Staff
Balthasar Blülle
Dr. Alfonso Gonzalez
Jakob Kanter
Dr. Philip Moll
PD Dr. Hans von Känel
Dr. Claudiu Falub
Jonathan Hanselmann
Thomas Kreiliger
Tobias Morf
Kristin Willa
Stanislaw Galeski
Roger Häusermann
Thomas Mathis
Dr. Yasmine Sassa
Tino Zimmerling

Master Students
Aline Fluri
Jeffrey Gehrig
Stanislaw Galeski
Sandra Jenatsch
Josua Stückelberger
Daniel Mazzone
Andrej Pustogow
Michael Wyss

Administrative Staff
Gabriela Strahm

Technical Staff
Kurt Mattenberger

High Pressure Synthesis

Academic Staff
Dr. Nikolai Zhigadlo

Academic Guests
Dr. Roman Puzniak, Polish Academy of Sciences, Warsaw (Poland)
Dr. Krzysztof Rogacki, Polish Academy of Sciences, Wroclaw (Poland)

1.1 Intrinsic Josephson junctions in the multi-band superconductor $(V_2Sr_4O_6)Fe_2As_2$

P.J.W. Moll, B. Batlogg, in collaboration with H.-H. Wen, Nanjing University, China

In layered superconductors such as the iron-pnictides or cuprates, Josephson junctions may be formed within the unit cell due to sufficiently low interlayer coupling. These intrinsic Josephson junction (iJJ) systems have attracted considerable interest for their application potential in quantum computing as well as efficient sources of THz radiation, closing the famous "THz gap". So far, iJJ have been demonstrated in single-band, copper-based high-T_c superconductors, mainly in Ba-Sr-Ca-Cu-O, while intrinsic Josephson coupling had not been found in iron-based superconductors so far.

We have observed clear experimental evidence for iJJ behavior in the iron-based multi-band superconductor $(V_2Sr_4O_6)Fe_2As_2$. The intrinsic junctions are identified by periodic oscillations of the flux flow voltage upon increasing a well aligned in-plane magnetic field. The periodicity is well explained by commensurability effects between the Josephson vortex lattice and the crystal structure, which is a hallmark signature of Josephson vortices confined into iJJ stacks. This finding adds $(V_2Sr_4O_6)Fe_2As_2$ as the first iron-based, multi-band superconductor to the copper-based iJJ materials of interest for Josephson junction applications, and in particular novel devices based on multi-band Josephson coupling may be realized.

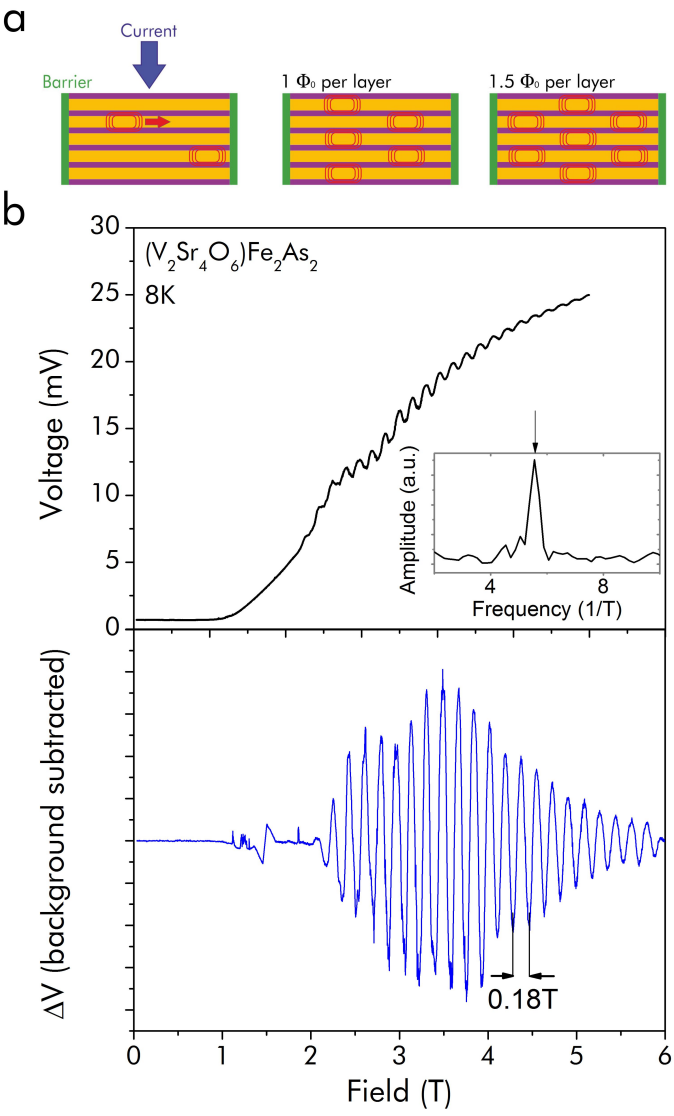

Figure 1.1: Periodic modulation of the flux flow voltage for magnetic fields well aligned with the FeAs layers. This observation is a hallmark of intrinsic Josephson systems: The oscillation period is directly related to the distance between two adjacent FeAs layers.

Of particular interest for application is the physical realization of an iJJ system in a multiband superconductor. The multi-band nature of the iron-based superconductors is expected to influence the junction behavior, thus novel effects and applications have been proposed that are inaccessible for single-band superconductors such as cuprates: Josephson vortices in intrinsic s$\pm$ junctions are predicted to show a significantly extended core region compared to single-gap materials due to destructive interference of the cooper pair tunneling channels. Therefore the vortex dynamics are expected to be distinct from single-band Josephson systems due to the different pinning of multi-band Josephson vortices. Additionally, the interactions of the different tunneling channels will influence the interlayer coupling, which have been proposed to assist the synchronization of junctions in a stack. The differences in evolution of the order parameter phase around the phase-core region of a Josephson vortex arising from the additional inter- and intra-band tunneling channels may also be exploited in phase sensitive iJJ applications such as quantum computing.

1.2 High frequency modulation calorimetry in high magnetic fields

S. Galeski, P.J.W. Moll, B. Batlogg

The possibility of extending the range of conditions available for experiments has always been the driving force for development in physics. With the recent development of high magnetic field pulsed magnets a new realm of magnetic fields ranging up to 100 T has become open for physicists.

In order to exploit this new possibility we are trying to develop a method enabling heat capacity measurements in magnetic field pulses lasting not more than several milliseconds. To perform such an experiment one has to achieve an over 10 kHz sampling frequency to precisely map the change of heat capacity with changing magnetic field.

The method we employ to accomplish this bases on the application of AC calorimetric principles with high modulation frequency to microscopic membrane based MEMS calorimeters and sub-micro gram single crystal samples.

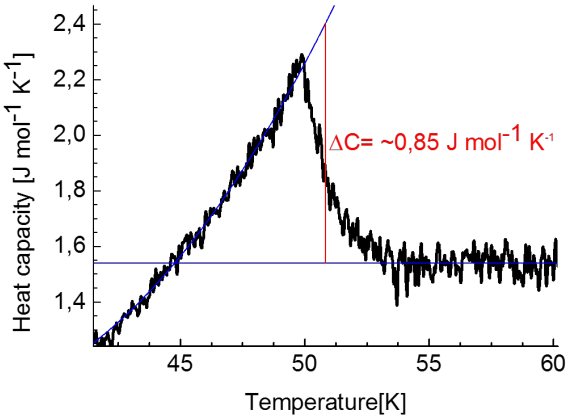

Figure 1.2: Specific heat anomaly of SmFeAs(O, F) single crystal measured at 100 Hz using a Xen-39399 calorimeter.

1.3 A cryogenic setup with optical access for low-noise electrical transport measurements under high pressures

M. Bachmann, J. Kanter, P.J.W. Moll, K. Mattenberger, B. Batlogg

The application of external pressure plays an important role in condensed matter research as it provides a direct way to change the interatomic distance, and hence the exchange and correlation effects in materials. Conducting experiments of this kind puts several demands on an experimental setup which include low temperatures, high pressures and the need of an in-situ pressure gauge which can be used at all temperatures. In addition transport measurements require low noise electrical access.
To generate high pressures and having an in-situ pressure gauge, the diamond anvil pressure cell (DAC) is a well suited tool, not only on account of diamonds compressive strength, but also because of its transparency to visible light. This advantage is exploited with the ruby fluorescence method of pressure measurement, the R_1-line (fig. 1.4a) of a ruby chip inside the sample space experiences a pressure dependent shift. The main benefit of this fluorescence-based manometer is the possibility to measure the pressure at any temperature.
To meet all the requirements a custom cryostat insert was build (fig. 1.3) with shielded, pre-amplified electrical wires and fiber optical access to the sample space. The setup was successfully tested down to 16 K.
The next step will be to use a focused ion beam (FIB) structured and contacted micrometer sized crystal (fig. 1.4b) to measure the transport anisotropy in SmFeAs(O,F) with the newly build setup.

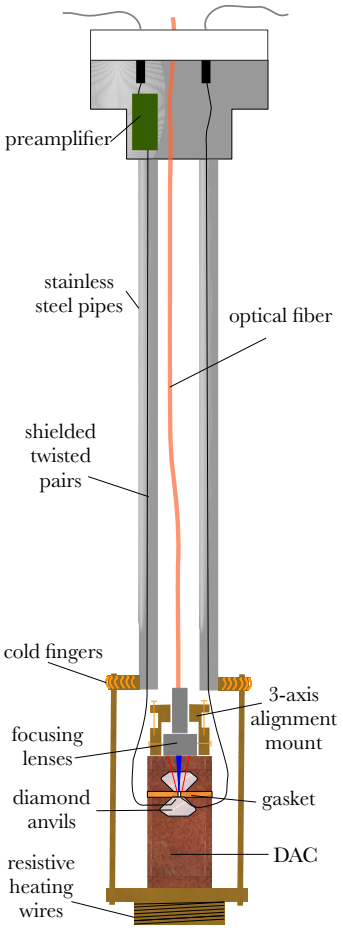

Figure 1.3: Sketch of the cryostat insert.

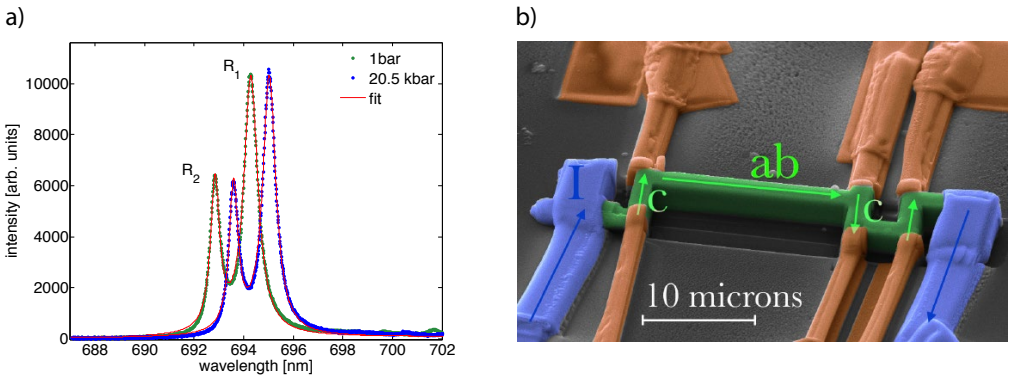

Figure 1.4: a) Shift of the ruby fluorescence between 1 bar and 20.5 kbar at room temperature. b) False colour SEM picture of the SmFeAs(O,F) crystal with indicated crystallographic directions.

1.4 Focused Ion Beam Sample Preparation for Electronic Transport Measurements under High Pressures

J. Kanter, P.J.W. Moll, M. Bachmann, S. Friedemann, P. Alireza, F. Ronning, E.D. Bauer & B. Batlogg

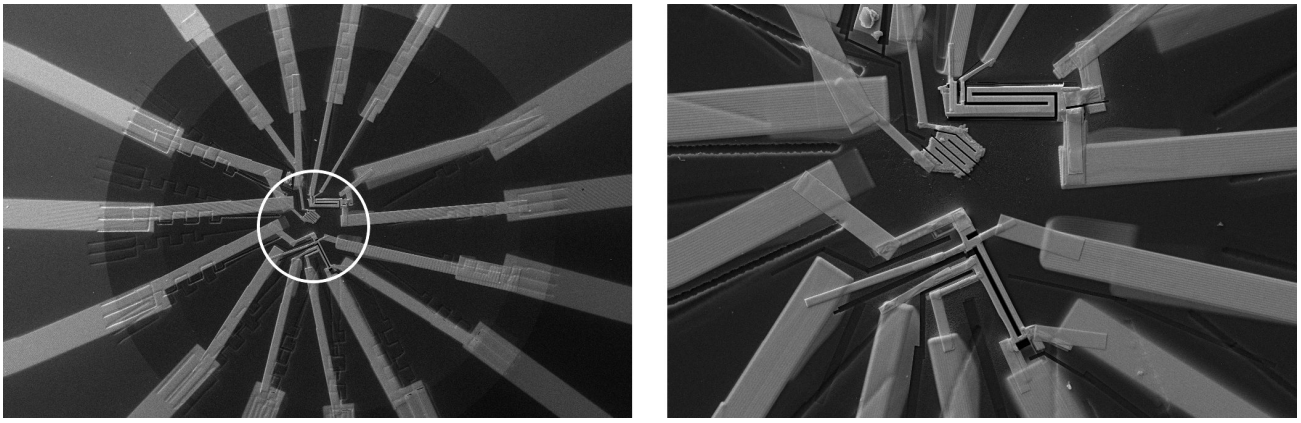

Figure 1.5: Left A pressure cell anvil showing three micro-structured samples on a sample space of about 300 μm in diameter, white circle, with 15 contacts. **Right** Close up of the anvil culet. The top and bottom sample are cut along different crystallographic axes, providing two different cuts through the Fermi surface in quantum oscillation measurements. In addition, the bottom sample is structured for measurements of the transport anisotropy.

Pressure is an important experimental parameter, as it allows to smoothly tune inter-atomic distances and orbital overlap, and can thereby strongly influence electronic correlation effects. However, transport measurements under high pressures pose several experimental challenges. The enormous forces acting on the electrical connections inside a diamond anvil cell together with the limited sample space, usually less than 400 μm in diameter, require special sample preparation techniques.

To this end we have applied the Focused Ion Beam technique, as it enables sample contacting and structuring down to a μm-scale. In addition a cryo-setup with optical access was built, enabling direct, precise pressure measurements at any given temperature. We have used the Focused Ion Beam sample preparation technique for preparation of quantum oscillation measurements on $CePt_2In_7$ and transport anisotropy measurements on high T_c superconductors. While quantum oscillation measurements can provide a wealth of information on the Fermi surface and electronic interactions, they usually exhibit only very small signal amplitudes. The micro-structuring allows to greatly enhance the length over cross-section ratio, substantially improving the signal to noise ratio of the measurement. In addition, the possibility to select different crystallographic axes, cut complex sample shapes and integrate several samples into one sample space, makes the Focused Ion Beam sample preparation an ideal tool for transport measurements under high pressures.

1.5 Organic single-crystal field-effect transistors with essentially trap-free interface and bulk

B. Blülle, R. Häusermann and B. Batlogg

The performance of field-effect transistors (FET) is strongly affected by localized states (trap states) between the valence and conduction transport levels. When a gate voltage is applied, these states are filled and thus affect the slope of the transfer characteristics. For today's electronics of decreasing size and increasing device density, steeply switching FETs are essential to reduce the power consumption. In conventional FET devices, the switching performance is improved by employing a high-κ dielectric and by reducing the amount of traps in the bulk and at the interface to the gate insulator.

We have measured organic rubrene single-crystal FETs fabricated by flip-crystal lamination on top of a hydrophobic gate dielectric (Cytop) with pre-evaporated gold contacts. These devices show textbook like transfer characteristics, as one would only expect for intrinsically trap-free semiconductors. Particularly, the high purity of our crystals and the defect-free interface are reflected in a high mobility of $14\,\mathrm{cm}^2/\mathrm{Vs}$ and in an unprecedentedly low subthreshold swing of $65\,\mathrm{mV/dec}$, remarkably close to the fundamental limit of $59\,\mathrm{mV/dec}$ at room temperature. From these measurements we have quantified the residual density of traps by a detailed analysis of the subthreshold regime, including a full numerical simulation. An exceedingly low trap density of $D_{bulk} = 1 \times 10^{13}\ \mathrm{cm}^{-3}\mathrm{eV}^{-1}$ at an energy of ~ 0.62 eV above the transport level was found. This corresponds to one trap per eV in 10^8 rubrene molecules. The equivalent density of traps located at the interface ($D_{it} = 3 \times 10^9\ \mathrm{cm}^{-2}\mathrm{eV}^{-1}$) is as low as in the best crystalline SiO_2/Si field-effect transistors, where typical trap densities are in the range of $D_{it} = 10^{10}\ \mathrm{cm}^{-2}\mathrm{eV}^{-1}$. [Zhuo et al., *Current Applied Physics* **12**, S57 (2012)]

These findings may come as a surprise considering the straightforward flip-crystal fabrication of the organic FETs which does not involve any UHV equipment. In fact, the low trap density is an immediate consequence of the electronically inert and chemically stable surface of the van der Waals bonded molecular semiconductor as well as its intrinsically trap-free interface with the gate dielectric.

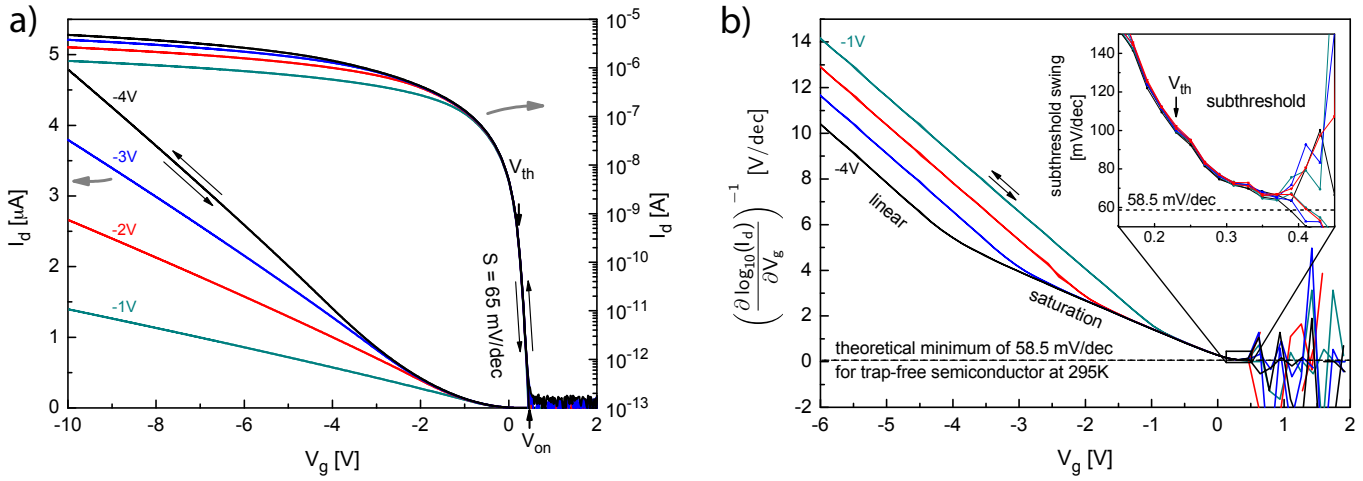

Figure 1.6: a) Measured transfer curve of a rubrene single crystal FET using a Cytop layer as gate dielectric. The device exhibits no hysteresis and its on-off ratio is larger than 10^7. The hole mobility is $14\,\mathrm{cm}^2/\mathrm{Vs}$.
b) Inverse logarithmic slope of the transfer curve (Fig. a). The inset shows the subthreshold region, where the swing approaches a value very close to the theoretical limit of 59 mV/decade.

1.6 Improving charge injection in high-mobility rubrene crystals: From contact-limited to channel-dominated transistors

T. Zimmerling and B. Batlogg

With progressively improving charge carrier mobility in organic semiconductors and miniaturization of organic field-effect transistors (OFETs), low contact resistances become ever more important. The contact resistance, which quantifies the efficiency of charge injection and extraction, tends to be high in OFETs, ranging typically between $10^4 - 10^7$ Ωcm. Thus, understanding and reducing the contact resistance is of great interest.

To study the capabilities of metal electrodes in OFETs and to explore the transition from contact-limited to channel-dominated transistor operation, we used flip-crystal FETs with gold electrodes having different contact resistances R_c to high-quality rubrene crystals. 4-terminal transfer and output measurements reveal that R_c decreases from $10^5 - 10^6$ Ωcm for 15 minutes air exposure to 3×10^3 Ωcm for at least 5 hours air exposure of the gold electrodes before the flip-crystal FET is assembled (Fig. 1.7 left). We conclude the reduction of R_c to be caused by a growing contamination layer on the gold electrodes that weakens the electrostatic coupling between rubrene crystal and gold electrode. The injection behavior in transistors with low R_c shows a much weaker diode characteristic than in transistors with high R_c (Fig. 1.7 right). These changes strongly influence the apparent mobility calculated from 4-terminal transfer measurements: In channel-dominated (low R_c) FETs the mobility is in the range of $10 - 17$ cm^2/(Vs); in contrast, in contact-limited (high R_c) FETs the apparent mobility decreases significantly with increasing contact resistance. The apparent $\mu - R_c$ dependence is not intrinsic, but rather the result of incorrect assumptions of the potential and the charge carrier density in the channel region. Thus, the development of high-mobility organic semiconductors requires further efforts to improve contacts beyond traditional metal electrodes.

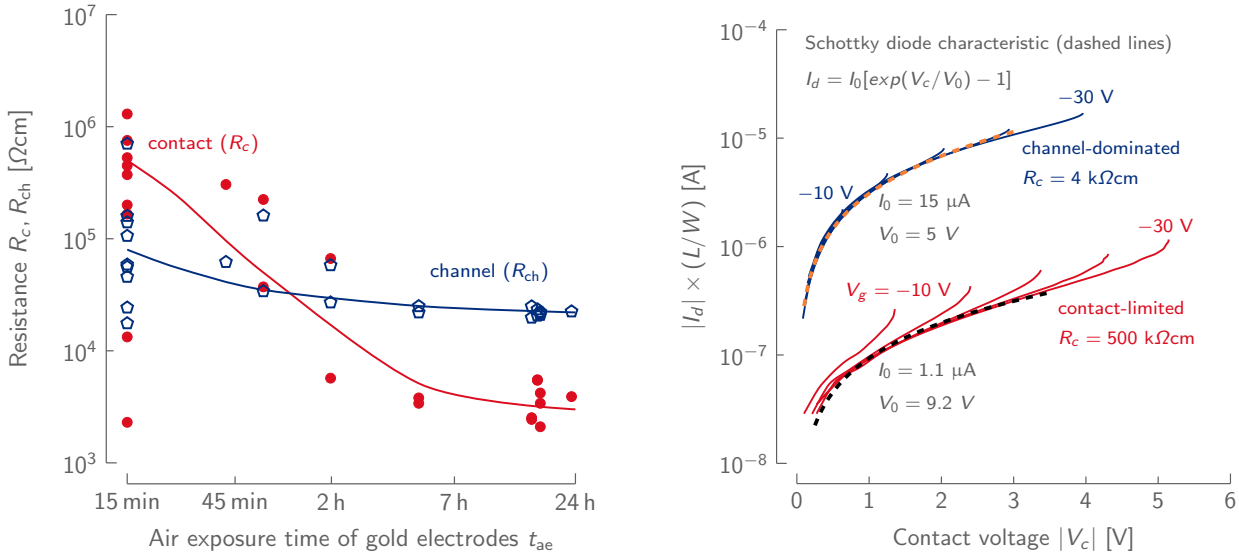

Figure 1.7: **Left:** The influence of exposing gold electrodes to air on contact resistance and channel resistance is shown for 24 rubrene flip-crystal FETs. **Right:** Diode-like injection at the gold-rubrene contact. The dependence of the drain current I_d on the contact voltage V_c is shown for V_g varying from -10 V to -30 V in steps of -5 V.

1.7 Stable organic field-effect-transistors with high mobilities unaffected by supporting dielectric based on phenylene-bridged thienobenzothiophene

T. Mathis

In collaboration with Y. Liu[1], L. Ai[1], Z. Ge[1], D. Lumpi[2], E. Horkel[2], B. Holzer[2] and J. Froehlich[2]

[1]Ningbo Institute of Material Technology and Engineering, Chinese Academy of Science, 315201 Ningbo, China

[2]Institute of Applied Synthetic Chemistry, Vienna University of Technology, 1060 Vienna, Austria

We explore on the electrical properties of organic field-effect transistors (FET) based on a new class of organic semiconductors. The molecules consist of the same thieno[2,3-*b*][1]benzothiophene (TBT) building blocks, connected by different π-bridge spacers (ethylene, phenylene and fluorophenylene), shown in figure 1.8. Molecular orbitals and HOMO/LUMO energies were calculated and compared with results from cyclic voltammetric and UV-vis absorption measurements. In order to study the influence of the bridge groups on the molecular arrangement and surface interaction, the transistor performance on a wide range of dielectrics has been investigated in detail. These include as grown SiO_2 and Al_2O_3 and also treated with OTS and ODPA, as well as Cytop and Parylene C. An extended study of the multitude of combinations of these materials (figure 1.9) produce a remarkable high mobilities up to $\sim$1 cm^2/Vs for devices made of the phenylene-bridged compound. Surprisingly the mobility was quite independent of the supporting gate dielectric. Stability over time has been observed with no degradation after 5 month. By eliminating the hysteresis using Cytop we were able to show that some of the molecules form films without long-term charge carrier trapping. These are interesting properties for practical industrial processing of organic electronics.

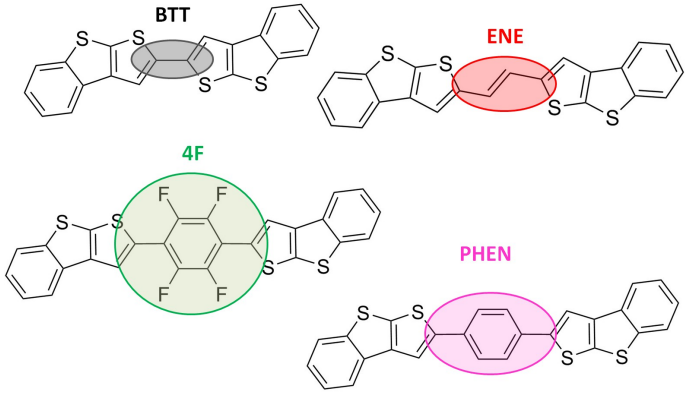

Figure 1.8: Molecular structure of the TBT building blocks connected by four different π-bridge spacers: direct linkage of TBT units (black, BTT), an ethene double bond (red, ENE), a fluorinated phenyl ring (green, 4F) and a phenyl ring (pink, PHEN).

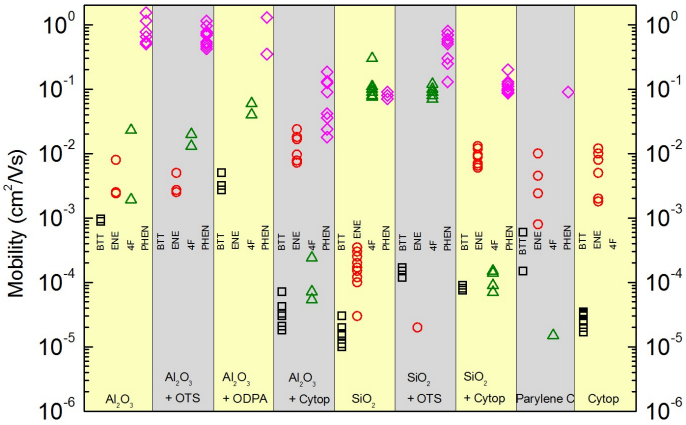

Figure 1.9: Summary of the hole mobility for OFETs produced by evaporating the four semicoducting materials on nine different gate dielectric stacks. Values as high as $\sim$1 cm^2/Vs and above are recorded for PHEN, and systematic trends are revealed for the other semiconductors.

1.8 Gating organic field-effect transistors using a re-attachable ionic liquid tape

C. Stelzer, B. Blülle, T. Mathis and B. Batlogg

In organic field-effect transistors, solid dielectric materials are traditionally used as gate insulators, and a highly hydrophobic gate dielectric (e.g. Cytop) can significantly improve the device performance. In these solid state dielectrics, however, the capacitance is limited by the dielectric constant and the film thickness. In electrolytes, on the other hand, and in particular in ionic liquids, the mobile ions can form electrical double layers upon application of an electric field, thus leading to high electric fields in the vicinity of the gate electrode and the semiconductor. A very high capacitance can be reached, independent of the insulator thickness, which can be used to accumulate charge carriers in a field-effect device.

To allow for a convenient fabrication of ionic liquid gated FETs, we saturated the ionic liquid EMIM-TCB in a copolymer (PVDF-HFP) to form mechanically stable ionic liquid tapes. The capacitance of these ionic tapes was measured by means of impedance spectroscopy and turned out to be as high as $C_{\mathrm{tape}} \approx 5\mu\mathrm{F/cm}^2$. This would correspond to a $\sim$ 0.4 nm thin dielectric Cytop layer, which is unrealistic thin for a film. The tapes can easily be cut, peeled off from the substrate and placed on top of a semiconducting crystal. Such a device is shown in Fig. 1.10a). A rubrene single crystal bottom gate FET was fabricated by flip-crystal lamination on a SiO_2/Cytop dielectric. The measured transfer curve of this device is shown in Fig. 1.10b) (black curve). The ionic tape was then laminated on top of the crystal and contacted by a gold wire. Not surprisingly, the currents seen in the measured transfer curve (red line in Fig. 1.10b) are at least one order of magnitude higher due to the much higher charge density accumulated in the conducting channel.

With this powerful method the Fermi level in the semiconductor can be pushed close to the transport level and thus the trap density of states near the band edge can be studied. This may also enable us to induce an insulator-to-metal transition.

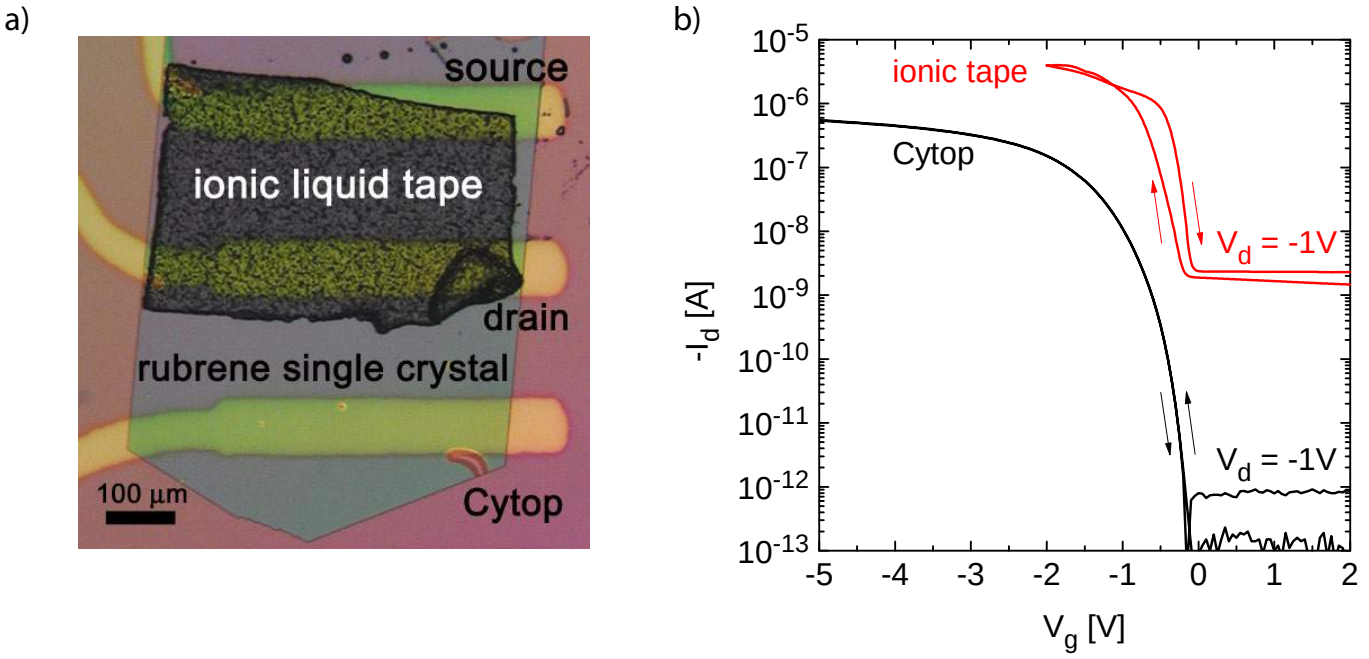

Figure 1.10: a) Rubrene single crystal laminated on a Cytop dielectric layer and covered by a strip of ionic liquid tape.
b) Transfer characteristics of the device shown in a): The transfer curve obtained by gating from the bottom (Cytop, black line) and using the ionic liquid tape as gate (red line). The high capacitance of the tape leads to a larger carrier density in the conducting channel, and thus to much higher drain currents.

1.9 Perfect crystals grown from imperfect interfaces

C.V. Falub, M. Meduna, D. Chrastina, F. Isa, A. Marzegalli, T. Kreiliger, A.G. Taboada, G. Isella, L. Miglio, A. Dommann, and H. von Känel

With the advent of nanofocused X-ray beams at third-generation synchrotrons it has become possible to address individual crystals down to the nanoscale non-destructively by X-ray scattering. Here we show by scanning nanodiffraction how misfit and thermal strain of a highly mismatched layer-substrate system may evolve when the substrate is deeply patterned at a micron scale. We show that space-filling arrays of highly perfect single crystals can grow from heavily dislocated interfaces, provided that epitaxial growth conditions and substrate patterns are carefully matched. As an example we take Ge-crystals on top of tall Si-pillars a few microns in width. For this system, the lattice mismatch amounts to 4.2%, while the difference of thermal expansion coefficients is 130% at 300 K. We demonstrate how elastic relaxation of the thermal strain leads to diminishing lattice bending as the crystals gain in height. We evaluate the net tilts of individual crystals emerging during the plastic relaxation of the misfit strain. Finally, by mapping the crystal quality on a nanometer scale, we provide evidence for perfect epitaxial single crystal growth from a heavily disordered interface.

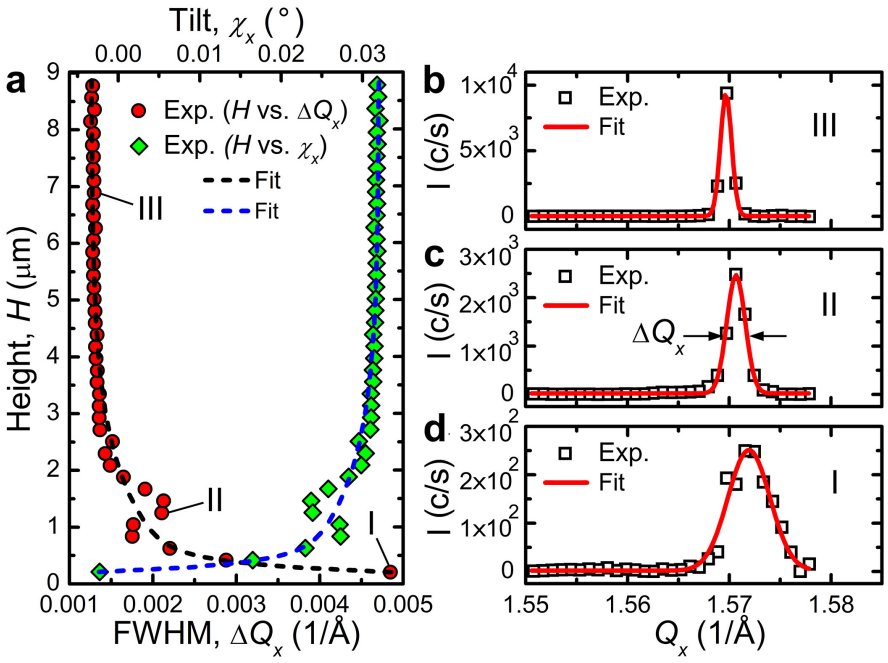

Figure 1.11: Full-width-at-half-maximum (FWHM) of the Ge(115) peak (ΔQ_x) and tilt (χ_x) along the Q_x direction vs. crystal height. The experimental data are fitted with asymptotic exponential functions, $y(x) = y_0 + a \cdot \exp(-b \cdot x)$, where a is positive and negative for $y = \Delta Q_x$ and $y = \chi_x$, respectively (dashed black and blue lines). b-d, Cross-sections through the Ge(115) peak along Q_x at 3 different crystal heights I, II and III indicated in (a). The experimental data are fitted to single Gaussians.

1.10 3D germanium crystal array on silicon readout chip for X-ray detection

T. Kreiliger, C.V. Falub, A.G. Taboada, F. Isa and H. von Känel in collaboration with: Y. Arroyo, R. Erni, P. Gröning (EMPA, Dübendorf, Switzerland), R. Kaufmann, P. Niedermann, A. Pezous, S. Mouaziz, A. Dommann (CSEM, Neuchatel, Switzerland), G. Isella (L-NESS, Politecnico di Milano, Italy)

Monolithic integration of different semiconductor materials on to silicon (Si) substrates has recently attracted high interest in micro technology industry. It would allow adding new functionalities to the well-established and widely used Si chip technology, such as optical emitters or detectors. Following this approach, we focused on the development of an innovative X-ray imaging detector where an efficient absorber is monolithically integrated onto Si-CMOS readout circuits, rather than using complex soldering techniques. It is based on a novel method to grow a crack- and defect-free crystalline germanium (Ge) absorber onto a Si substrate despite the large lattice (4.2%) and thermal expansion (130%) mismatches of the two materials involved. We use deeply patterned Si substrates in the form of pillars and deposit epitaxial Ge in a unique "Low-Energy Plasma-Enhanced Chemical Vapor Deposition" (LEPECVD) reactor. This results in arrays of individual, closely spaced, high-quality Ge crystals up to dozens of microns in height. Electrical characterization of hetero-junction diodes formed by these p-Ge crystals and the n-Si substrate was carried out inside a scanning electron microscope (SEM) chamber. The individual Ge crystals were electrically contacted by a conductive tungsten micro-manipulator. Our structures feature a very high surface-to-volume ratio compared to regular, film-based Si-Ge diodes. Therefore, the effect of Si pillar sidewall passivation onto the diode characteristics was investigated. To prevent surface leakage currents through the sidewalls, wet chemical etching techniques were optimized to remove the defected Ge material in the substrate trenches. Our micron-sized diodes exhibit reverse dark-currents below 1 mA/cm^2 at -10 V, which compare favorably with existing Si-Ge diodes and are promising for the development of a novel X-ray detector.

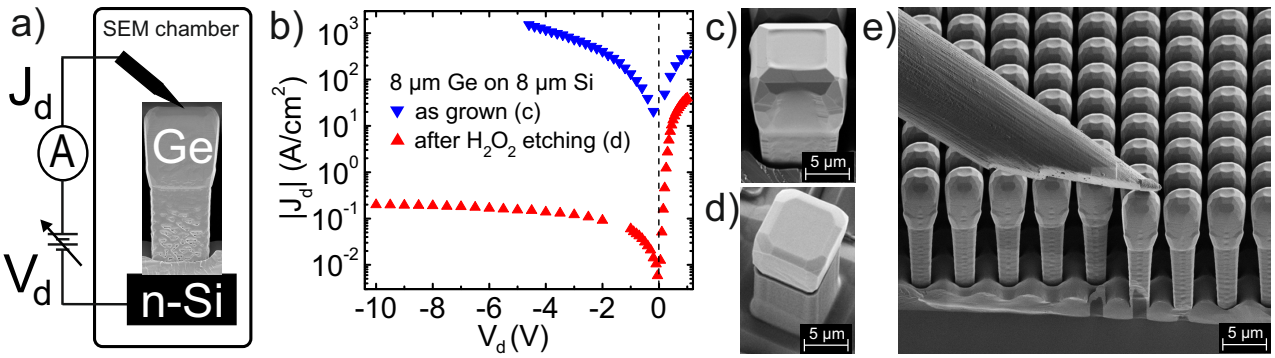

Figure 1.12: (a) Schematic view of the measurements setup inside the SEM chamber. (b) Comparison of dark current-voltage diode characteristics of single Ge crystals on Si pillars, before and after etching in H_2O_2, as shown in perspective view SEM (c) and (d) respectively. (e) Perspective view SEM of the tungsten micro-manipulator contacting one of the Ge crystals.

1.11 Strain relaxation of GaAs/Ge crystals grown on Si substrates

A.G. Taboada, T. Kreiliger, F. Isa, E. Gini, C.V. Falub and H. von Känel in collaboration with: L. Wewior, D. Fuster, B. Alen (IMM-SCIC, Spain), G. Isella (L-NESS, Politecnico di Milano, Italy), L. Miglio, M. Salvalaglio (L-NESS, Universita di Milano Bicocca, Italy), F. Mancarella (CNR-IMM, Bologna, Italy), M. Richter, E. Uccelli (IBM Research, Switzerland), P. Niedermann, A. Neels, A. Dommann (CSEM, Neuchatel, Switzerland)

Integration of direct bandgap semiconducting materials, such as GaAs, on Si CMOS platforms will be a key milestone for future optoelectronic device development. The main drawbacks to overcome in order to monolithically integrate GaAs on Si are the mismatch both of lattice parameters and thermal expansion coefficients. In addition, the growth of a polar material (GaAs) on top of non-polar one (Si) leads to the formation of antiphase domains at the interface. In order to solve these problems, we chose to adapt the concept of 3-dimensional (3D) hetero-epitaxy to this material system.[1][2] Our approach involves the use of a Ge spacer on top of 8-μm-tall Si pillars. This is a substitute for Ge substrates which are characterized by a very small lattice mismatch (0.07%) and comparable thermal expansion coefficients (15%) with respect to GaAs. Figure 1(a) shows a top view of 4-μm-tall GaAs crystals grown by MOVPE on 15x15 μm^2 wide Si pillars, previously coated with 2 μm of Ge. The asymmetrical distribution of $\{111\}$ facets and the top (001) surface results both from the substrate 6° miscut and the different facet growth rates. The asymmetry is even more apparent in the (1-10) and (110) cross sections of Fig. 1(b) and (c). Figures 1(d, e) show 2Θ-ω XRD scans measured on GaAs/Ge crystals grown on Si pillars ranging from 2 μm to 40 μm in width compared with reference material grown on a planar Ge/Si substrate. The strain relaxation as a function of the crystal aspect ratio, displayed in fig 1(e), is in good agreement with the strain values calculated by Finite Element Method simulations (Fig. 1(f)). The optical response of the GaAs crystals was mapped by micro photoluminescence at the nanoscale (Fig. 1(g)).

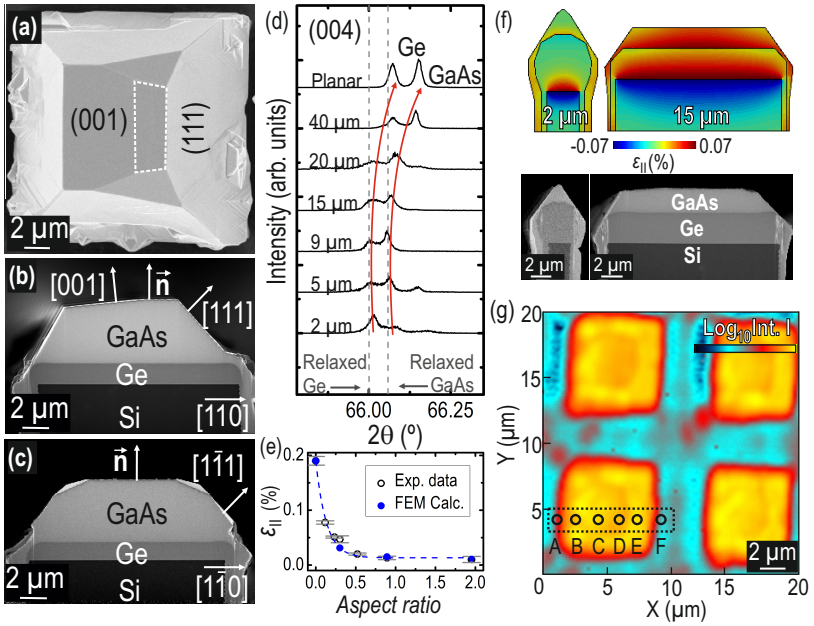

Figure 1.13: (a) SEM image of the top surface of 4-μm-tall GaAs crystals grown on 15-μm-wide Si pillars and cross sections parallel to the (1-10) (b) and (110) (c) planes. (d) 2Θ-ω XRD scans corresponding to the different GaAs/Ge/Si microstructure sizes (from 2 μm to 40μm wide) compared with a reference epitaxy grown on a planar Ge/Si substrate. (e) Strain values for the different sizes compared with the volume strain calculated from the FEM strain relaxation simulations, displayed in (f) together with their correspondent cross-sections. (e) Micro-PL integrated intensity map of a 20x20 μm^2 area containing four GaAs crystals grown on Ge coated 9x9 μm^2 Si pillars.

Chapter 2

Physics of mesoscopic structures, semiconductor nanostructures

(http://www.nanophys.ethz.ch)

Head
Prof. Dr. K. Ensslin
Prof. Dr. T. Ihn

Academic Staff

J. Arrieta	S. Baer	Dr. C. Barraud
Dr. J. Basset	D. Bischoff	B. Braem
P. Butti	T. Choi	T. Frey
S. Hellmüller	A. Hofmann	A. Jacobsen
Dr. A. Kozikov	T. Krähenmann	S. Müller
F. Nichele	Dr. A. Pal	N. Pascher
Dr. C. Rössler	P. Simonet	R. Steinacher
A. Stockklauser	Y. Tian	A. Varlet
M. Walser		

Master Students

R. Gaudenzi (FS2013)	S. Burkhard (FS2013)	B. Bissig (FS2013)
S. Butz Sebastian (FS2013)	A. Hofmann (FS2013)	F. Timpu (HS2013)

Technical Staff

C. Barengo	P. Märki	P. Studerus

Administrative Staff

C. Vinzens	C. Egli

Academic Guests
Timothe Faivre, University Joseph Fourier, Grenoble, France, (April 1 - May 1, 2013)
Georgia Tsoukleri, University of Patras, Greece, (May 9 - August 8, 2013)
Yoshitaka, Nishihara, Kyoto University, Japan, (October 1 - 31, 2013)
Hiske Overweg, Ecole Normale Superieur, Paris (February 4 - June 6, 2013)
Pavel Prochazka, University of Technology, Brno, Czech Republic (July 1 - December 18, 2013)

NCCR QSIT

Dr. I. Blatter	S. Künzel	Dr. J. Rössler

2.1 Cyclic depopulation of edge states in a large quantum dot

S. Baer, C. Rössler, T. Ihn, and K. Ensslin, in collaboration with C. Reichl and W. Wegscheider

Two-dimensional electron systems at low temperatures and in strong magnetic fields show a rich spectrum of highly degenerate, incompressible ground states. Fractional quantum Hall states, occurring at a fractional filling factor ν with an odd denominator, are well described by the Laughlin wavefunction. There exists a prominent exception from this hierarchy: the $\nu = 5/2$ state, which is believed to obey non-Abelian statistics. This remarkable property could make it an interesting candidate for the realization of a topological qubit. Theoretical ideas on probing the statistics of the $\nu = 5/2$ state rely on the use of quantum dots (QDs), which are operated as Fabry-Pérot interferometers.

We have investigated a large QD with a quantum point contact (QPC) serving as a charge detector (CD). When the QD is operated as a Fabry-Pérot interferometer, we find resonances with a slope in the voltage-magnetic field space and a periodicity characteristic of a Coulomb dominated effect, as already observed in previous experiments. When the system is operated at a lower transmission where the barriers are in the tunneling regime, the amplitude modulation can be observed over a large parameter range for different filling factors, allowing the direct measurement of the charge stability diagram of capacitively and tunnel-coupled edge states. As a consequence, we can estimate the width of the incompressible region separating the edge channels inside the QD. In contrast to previous experiments, this is accomplished by using capacitances directly extracted from the measured charge stability diagram. Furthermore, we are able to investigate the CB amplitude modulation by using (time-resolved) charge detection techniques, where it shows up as an increased/decreased tunneling rate. To our knowledge, single-electron counting has never been performed with a QD of a similar size. Direct transport measurements do not always reflect the full complexity of the edge state substructure inside a QD. In future experiments, single-electron counting might provide additional important insight into charge localization and transport in micron-sized Fabry-Pérot interferometers. Most of the proposed Fabry-Pérot interferometry experiments for probing the properties of fractional quantum Hall states assume edge states to be one-dimensional electron or composite fermion channels with negligible interaction between compressible regions. We show that when the edge states are confined to the QD, a complex behavior with compressible and incompressible regions is observed. The observed tunnel coupling between the different compressible regions, i.e. the presence of tunnel-coupled alternative paths, might influence the outcomes of the proposed interferometry experiments.

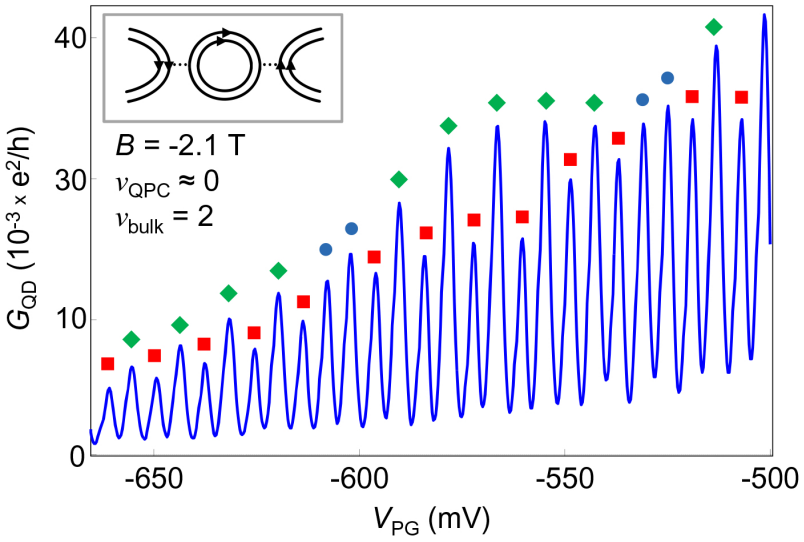

Figure 2.1: Coulomb blockade peaks for a bulk filling factor of 2. When depleting the dot, Coulomb peaks with a high/low peak current (diamonds/squares) are observed, interrupted by two peaks of a similar magnitude (filled circles).

2.2 Interference of electrons in backscattering through a quantum point contact

A. A. Kozikov, C. Rössler, T. Ihn, and K. Ensslin, in collaboration with C. Reichl and W. Wegscheider

Scanning gate microscopy (SGM) is a scanning probe technique in which the conducting tip of an atomic force microscope (AFM) acts as a moveable gate locally changing the electron density beneath it. It allows the investigation of the electron behavior beyond conventional transport measurements. Its successful implementation started about 16 years ago and was followed a few years later by the pioneering experiment to image the electron backscattering through a narrow constriction in a high-mobility two-dimensional electron gas (2DEG). Since then the SGM technique has become widely used for local studies of electron transport in different nanostructures . Back in the year 2001 when electron backscattering through the quantum point contact (QPC) was imaged by Topinka et al., it was unexpectedly found to be dominant along narrow branches decorated by interference fringes about half the Fermi wavelength apart. The branching behavior has been studied for several years since then. It was found that classical mechanics could explain the formation of branches, whereas quantum mechanics was needed to account for their stability upon initial conditions. Local electron transport through a QPC was used to study electron–electron interactions or to map the local carrier density.

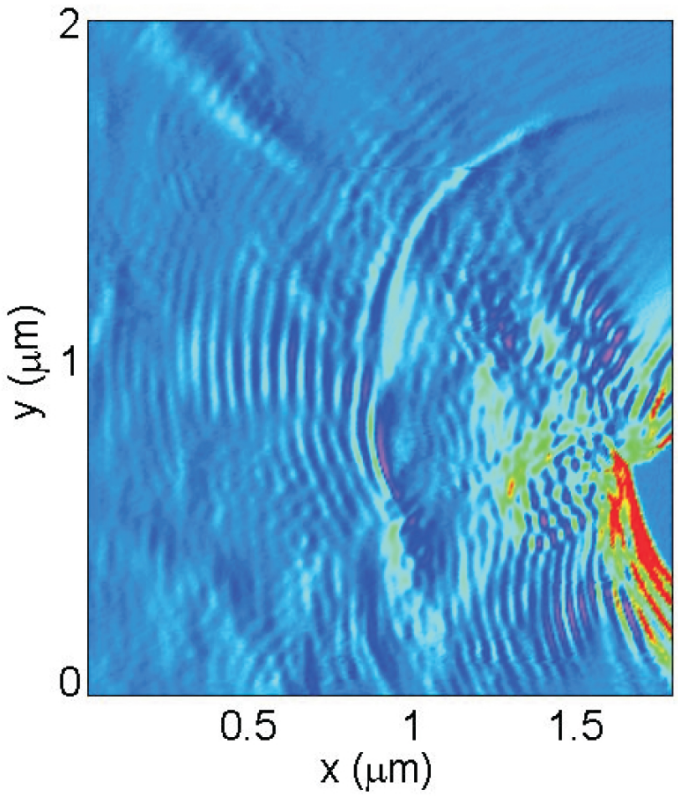

Figure 2.2: Electron backscattering through the QPC imaged using a gating compensating technique when the QPC is biased on the fourth plateaus. The color code is the conductance of the device as a function of tip position.

We performed SGM experiments of electron backscattering through a quantum point contact fabricated on a high-mobility GaAs heterostructure. A branching behavior was observed together with interference fringes that decorate the branches. We imaged its evolution at several points on a plateau as well as between plateaus. We found that for a fixed lateral position of the QPC the number and the intensity of branches change only when the QPC conductance becomes lower than an integer multiple of $2e^2/h$. When it is equal to or higher than an integer multiple of $2e^2/h$, the electron backscattering pattern remains stable. A lateral shift of the QPC, which changes the injection conditions, affects the branching pattern. The branches are thus related to the random disorder potential in the 2DEG.

Measurement of the QPC conductance as a function of the gate voltages at different tip biases, tip positions and

low perpendicular magnetic fields showed that the conductance at the plateaus was restored when the B-field was applied. At the same time, in the images of electron backscattering the branches of the pattern and the interference fringes gradually disappeared. This illustrated that backscattering is important for the observation of the branches and interference fringes. Some of them faded away faster than others, which means that different mechanisms of fringe formation are present.

2.3 Tunable charge detectors for semiconductor quantum circuits

C. Rössler, T Krähenmann, S. Baer, T. Ihn, and K. Ensslin, in collaboration with C. Reichl and W. Wegscheider

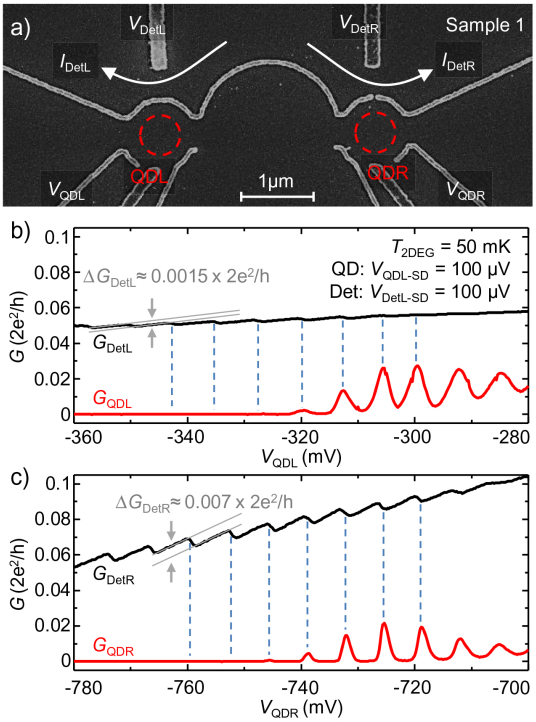

Figure 2.3: (a) Scanning electron micrograph of the sample. Schottky gates appear bright and the crystal surface appears dark. Applying negative voltages to gates depletes the underlying electron gas and defines two QDs (dashed circles) and two constrictions serving as charge detectors (white arrows). The left and right half of the structure is identical with the exception of a gap in the gates between the right QD and its detector. (b) Gate voltage VQDL controls the number of electrons in the left QD, giving rise to Coulomb blockade oscillations in the differential conductance (red). Each change of the electron occupation number is accompanied by a kink in the differential conductance of the detector (black trace). (c) Differential conductance of the right QD and the right detector , plotted as a function of gate voltage VQDR. The high detector sensitivity is attributed to the particular geometry of the detector gates.

Clean low-dimensional electron systems exhibit a rich spectrum of interaction-induced effects such as the formation of composite fermions, the $\nu = 5/2$ state, the 0.7 anomaly or the Kondo effect, which are the subject of current fundamental research. By confining interaction-induced states via quantum point contacts (QPCs), interferometers or quantum dots (QDs), one hopes to utilize experimental techniques such as coherent charge- and spin manipulation, full counting statistics or controllable coupling to other two-level systems to gain further insight into the underlying physics. Many of these experiments rely on detecting changes of a localized charge state via an adjacent QPC serving as the charge detector. Its detection fidelity poses a fundamental limit to the readout speed of qubits and has, therefore, been subject of several investigations. It was found that the detection fidelity can be improved by maximizing both the detectorÕs pinch-off slope and the capacitance between QD and QPC. The detector slope was increased by employing single electron transistors or QDs as detectors. The capacitive coupling can be improved by placing QD and detector in close proximity to each other by avoiding metal gates in-between QD and detector and/or by employing a floating gate on top of QD and detector.

We investigated several methods for improving the sensitivity of charge detectors. The capacitive coupling between QD and detector was increased by using a floating gate. However, the increased sensitivity comes at the cost of charge rearrangements, making this technique difficult to handle in a typical gate-defined nanostructure. Introducing a gap in the barrier gates between QD and detector, we find a strongly enhanced sensitivity which is attributed to reduced screening, reduced lateral distance between QD and detector and a steeper detector slope due to the formation of a localized state. Formation and lateral shifting of the localized state was investigated and demonstrates that the detector can be tuned gradually from QPC-like to QD- like characteristics. Finally, the technique of using a localization for sensitive charge-readout was applied to a large QD in the quantum Hall regime.

2.4 Aharonov–Bohm rings with strong spin–orbit interaction: the role of sample-specific properties

F. Nichele, Y. Komijani, S. Hennel, T. Ihn, and K. Ensslin, in collaboration with D. Reuter, A. D. Wieck, C. Gerl, W. Wegscheider

Semiconductor nanostructures implemented in two-dimensional systems with large spin–orbit interaction (SOI) are considered as potential building blocks for the realization of quantum information processing and various spintronic devices. In this framework, nanodevices implemented in p-type GaAs/AlGaAs heterostructures have been subject to intense theoretical and experimental studies concerning physical phenomena related to carrier–carrier Coulomb interaction and SOI.

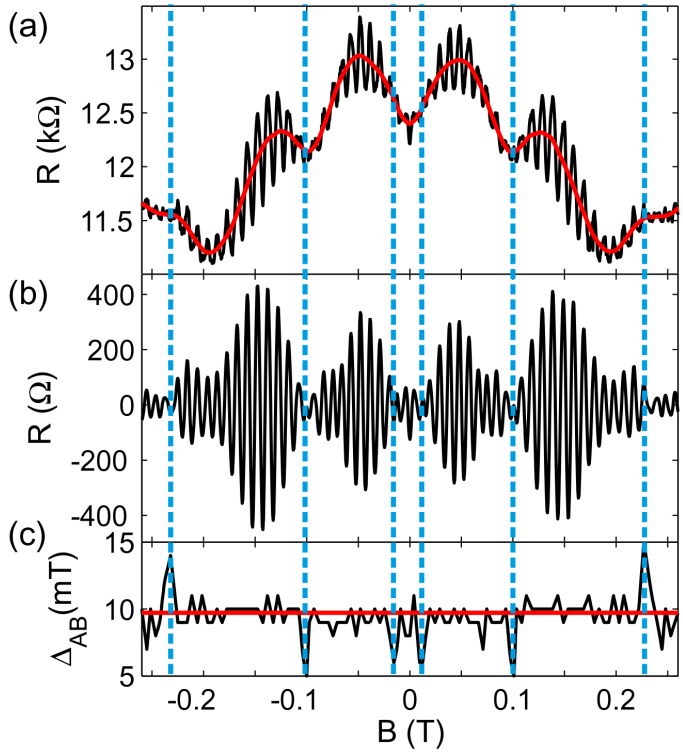

Figure 2.4: (a) Measured four terminal magnetoresistance of the ring (black curve) together with the low frequency background which is subtracted from the data (red curve). (b) Extracted h/e oscillations. (c) Period of the h/e oscillations calculated from the separation between two successive extrema. The position of the phase jumps in the h/e oscillations is indicated by the blue dashed lines.

A two-dimensional hole gas (2DHG) in the valence band of GaAs is characterized by wave functions whose symmetry is reminiscent of atomic p-orbitals. Due to the non-zero angular momentum and to the confinement in the growth direction, carriers are effectively described as spin 3/2 particles, for which SOI corrections (cubic in the momentum) are expected to be stronger than for their electronic counterpart. Furthermore, holes in GaAs have a very high effective

mass, several times larger than that of the electrons in the conduction band. The smaller Fermi energy makes the carrier–carrier Coulomb interactions more pronounced, allowing the study of many-body related effects. It is predicted that, in a ring-shaped nanostructure penetrated by a magnetic field, the strong SOI would induce, in addition to the conventional AB phase, a second geometrical phase term. This additional term, that in the adiabatic limit is commonly referred to as a Berry phase, acts on the spin part of the particle wave function. The interplay between AB phase and geometrical phase is expected to result in a complex beating-like behavior of the oscillatory magnetoresistance.

We have reported measurements of large-amplitude AB oscillations in highly tunable p-type GaAs rings. In our experiments we can qualitatively reproduce various features observed in previous work (splitting of Fourier peaks, beatings, gate-dependent phase jumps) that were interpreted as signatures of SOI induced effects. Based on the discussion of the gate voltage and the temperature dependence of the features, we propose an alternative origin that does not involve SOI. In particular we focus our attention on transverse mode mixing, energy averaging and interplay of the AB phase with the phase coherent conductance fluctuations. We point out that the temperature is a parameter to be taken into account, since a small energy averaging can lead to a substantial modification of the beatings. Finally we have tried to extract traces of SOI induced effects from the average of Fourier spectra taken in large ensembles of data. The results indicate that in our case most features can at least qualitatively be explained by sample-specific features.

2.5 Electronic triple-dot transport through a bilayer graphene island with ultra-small constrictions

D. Bischoff, A. Varlet, P. Simonet, T. Ihn, and K. Ensslin

Since becoming experimentally available in 2004, graphene has triggered a wide range of research due to its many special properties. Graphene was suggested for building spin qubits early on, as long spin coherence times are expected: in nature, predominantly the $^{1}2$C isotope occurs which does not have a nuclear spin. Furthermore carbon has a low atomic number which should lead to small spin orbit coupling. Both effects are known to limit spin coherence times in, for example, GaAs. In the past, graphene single electron transistors and quantum dots were fabricated in different ways: structures were etched by reactive ion etching, and defined by gates or alternative methods. Single constrictions showing a Coulomb-blockade were fabricated, single dots were fabricated and double dot systems were investigated. These structures were fabricated from single layer graphene bilayer graphene or multilayer graphene.

Compared to electrostatically defined GaAs nanostructures, etched graphene devices are strongly influenced by disorder, which limits both the control as well as the reproducibility of the performed experiments. Desired properties such as, for example, tunneling rates that are monotonically tunable by gate voltage or spin-blockade have so far not been observed. Other expected effects such as, for example, the observation of excited electronic states, reliable identification of few electron and hole states, shell filling or the Kondo effect have only rarely been observed and are hard to reproduce.

We have fabricated a bilayer graphene quantum dot where both the dot size and the constriction size are at the limit of our currently employed technology. Even for these short and narrow constrictions, single electron charging inside the constrictions plays an important role for transport. As the device was designed such that it exhibits a high symmetry, it was possible to triangulate the positions of the different sites of localized charge: one quantum dot is formed in the island and at least one quantum dot is formed in each of the constrictions. While the quantum dot in the island is rather stable in shape and position, the dots in the constrictions vary in size and position. We have shown that depending on which gates are swept, either one slope or three slopes are visible in plots of the conductance in the plane of two gate voltages. In this regime where three sites of localized charge are arranged in series, we measured many consecutive and non-overlapping Coulomb diamonds. We discussed this behavior within the framework of higher order cotunneling processes. In a system as presented in this paper it might be hard to observe certain effects as for example single dot Kondo physics: the Kondo effect itself occurs in the cotunneling regime of a dot coupled to Fermi leads. If these leads happen to be dots themselves with a level being populated with a spin (up or down)

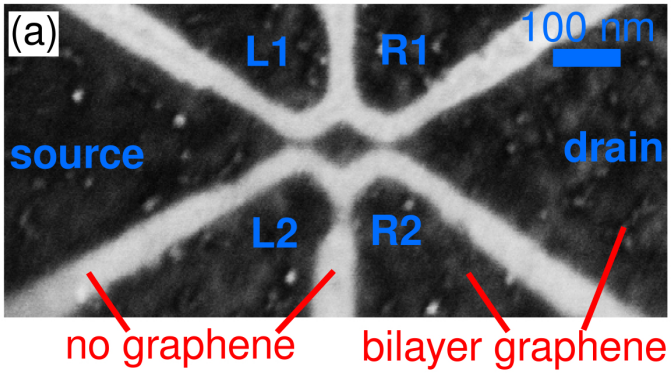

Figure 2.5: (a) Scanning electron microscopy image of the investigated device.

electron, then the concept of a screening cloud can not easily be applied. In order to create better controllable single graphene quantum dots, we believe that alternative fabrication methods need to be investigated in more detail. One promising candidate are the split-gated bilayer graphene structures where the edges are defined electrostatically.

2.6 Single-electron double quantum dot dipole-coupled to a single photonic mode

J. Basset, D.-D. Jarausch, A. Stockklauser, T. Frey, T. M. Ihn, and K. Ensslin, in collaboration with C. Reichl, W. Wegscheider, and A. Wallraff

Recent theoretical work on coupling semiconductor quantum dots with superconducting transmission line resonators has promised novel research avenues towards a well-controlled coherent interface between electronic quantum dot excitations and quantized microwave frequency fields. On the experimental side, pioneering experiments have demonstrated electrical dipole coupling between electrons confined into quantum dots and the microwave photons stored into a resonator by measuring dispersive and dissipative effects in the resonant transmission of photons through the resonator. These experiments demonstrated a quantum dot cavity coupling up to 50 MHz, much smaller than the extracted decoherence rates of 1–3 GHz. Further research is now needed to reduce the decoherence rate to such an extent that the strong-coupling regime can be reached.

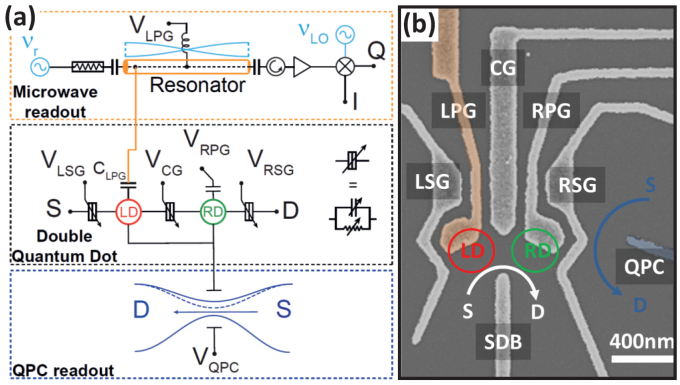

Figure 2.6: (a) Circuit diagram of a double dot (center panel) coupled to a resonator (top panel) and a quantum point contact (bottom panel). The double dot is tuned with gate voltages VLPG, VRPG, VCG, VSDB, VLSG ,VRSG. It is coupled to the resonator via the capacitance CLPG. The resonator is driven with a microwave signal at frequency ν_r. The transmitted signal passes through a circulator, is amplified, and is mixed with the local oscillator to obtain the field quadratures I and Q. The QPC is tuned with voltage VQPC. (b) Scanning electron microscope picture of a double dot gate design similar to the one used in the experiment. The gate extending from the resonator is shown in orange. The gate QPC used for charge detection is shown in blue.

We have realized a device in which the dipole coupling of a single-electron double quantum dot charge qubit to a superconducting resonator was investigated. A master equation calculation of the coupled system based on the

Jaynes-Cummings Hamiltonian allowed determining the tunnel coupling between the dots which we compared to values extracted from a well-established quantum point contact based charge measurement. The two techniques are found to be equivalent with a higher precision using the resonator when tunneling rates approach the resonator eigenfrequency.

We have compared the coherence properties of the double dot system in the single and in the many-electron regime. A reduction of the dephasing rates by a factor of 2 was observed over the entire tunneling range in the single-electron compared to the many-electron regime. Qubit dephasing rates are very large (GHz) compared to the coupling to the resonator in both cases highlighting the limited role of the excited states spectrum in the decoherence of our GaAs based heterostructure.

2.7 Imaging magnetoelectric subbands in ballistic constrictions

A. A. Kozikov, C Rössler, T. Ihn, and K. Ensslin, in collaboration with D. Weinmann, C. Reichl, and W. Wegscheider

Quantum point contacts (QPC) are the basic building blocks of many mesoscopic circuits. Quantized conductance requires ballistic transport with an elastic mean free path exceeding the dimensions of the QPC. In a series arrangement of two QPCs the total conductance depends on how electron waves couple into and out of the region between the QPC. If this region is a cavity, then interference of electron waves can also play an important role. In mesoscopic devices the gate arrangement and therefore the dominant features of the potential landscape are usually fixed. A moving gate, as it is provided by the metallic tip of an atomic force microscope (AFM), allows us to vary the potential landscape in real space and enables the investigation of ballistic and coherent transport properties of networks of QPC. Not only the tip-sample bias voltage but also the tip-surface distance and the in-plane tip position can be changed in order to control the strength and gradient of the tip-induced potential and thereby influence the electron wave pattern.Here we present local study of ballistic and coherent transport properties of networks of QPCs.

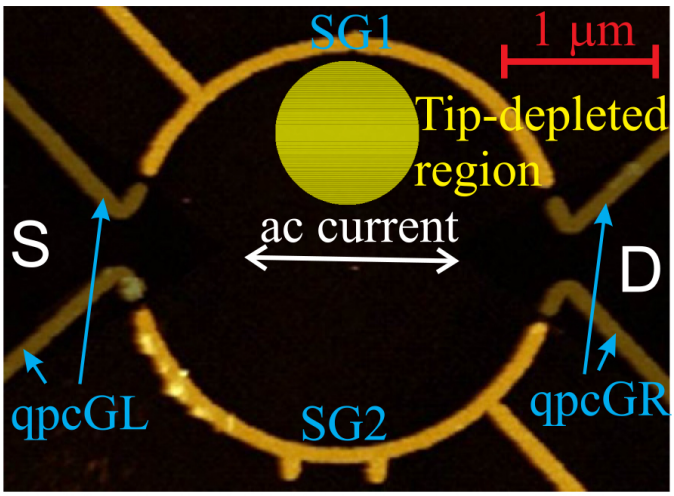

Figure 2.7: A room temperature AFM image of the sample. The stadium gates, SG1 and SG2, are biased, which is indicated by bright yellow metal. At the entrance and exit of the stadium there are two narrow QPCs (dark yellow metal) formed by the gates on the left, qpcGL, and on the right, qpcGR. The QPC top gates are grounded in this experiment. A double arrow in the centre of the stadium corresponds to the ac current flowing between source (S) and drain (D). The tip-depleted disc is schematically represented by a filled yellow circle and placed as an example in the region (III) of enhanced conductance.

We have presented experimental results of local studies of the conductance through a ballistic cavity connected to the leads by two constrictions using SGM in the presence of small perpendicular magnetic fields. We observed strong tip-position dependent fluctuations of the conductance when the tip was scanned inside the cavity, regions where the conductance was increased above the unperturbed conductance of the structure and checker board shaped fringe patterns when the tip was close to one of the constrictions. These patterns allowed to precisely control the number of

transmitted modes in the channels formed between the tip potential and the confinement caused by the top gates, which may in the future be used to image Aharonov-Bohm oscillations in the quantum Hall regime. Investigating the fringe patterns in a perpendicular magnetic field we observed a transition from the electrostatic to magnetic depopulation of subbands. This effect was seen in spatially resolved images where narrow fringes were present at low magnetic fields, which gradually transformed into wide conductance plateaus at higher B-fields. The plateaus corresponded to integer filling factors. Classical and quantum simulations described very well most of our observations.

The observed features in the tip-induced conductance changes and the comparison with the model calculations clearly indicate that our device was operated in the coherent quantum transport regime. Moreover, our modeling allowed to understand in detail the origin of the observed conductance changes. Most of the local features seen in our experimental conductance images cannot directly be interpreted in terms of a corresponding local current flow as it was suggested in the context of single QPCs operated on a quantized conductance plateau. Though we cannot measure the local current density in the absence of the tip, it seems obvious that the checker board fringe patterns observed close to the QPCs and the tip-induced enhancement of the conductance above the unperturbed value do not reflect the behavior of local current flow in the unperturbed device. Since our data do not show a well-defined conductance plateau, the absence of an interpretation of the conductance change in terms of local current flow is consistent with a recent theoretical study, perturbative in the tip potential, where the conductance change could be unambiguously related to the local current density only in the case of a structure having spatial symmetry and being operated on a quantized conductance plateau.

Chapter 3

Dynamics of strongly correlated materials

(http://www.dscm.ethz.ch)

Head
Prof. Dr. Joël Mesot
Prof. Dr. Hans-Rudolf Ott

Academic Staff
Dr. Toni Shiroka
Marek Pikulski

Master Students
Lukas Korosec (HS 2013)
Federico Eggenschwiler (HS 2013)

Administrative Staff
Gabriela Strahm
Claudia Vinzens

3.1 Impact of strong disorder on the static magnetic properties of spin-chains

T. Shiroka, F. Casola, H.-R. Ott, and J. Mesot
in collaboration with K. Prša (EPF Lausanne), and W. Lorenz, A. Zheludev (ETH Zurich)

Although Heisenberg spin-$1/2$ chain materials have been extensively studied over the years, much less is known about the behaviour of such 1D systems in the presence of disorder. A particularly interesting case is that of random Heisenberg chains (RHC), which feature a *random* distribution of exchange parameters. Theoretical predictions on their ground state [1, 2], the so-called random-singlet state (RSS), have only scarcely been investigated experimentally.

In our work we considered the disordered quasi-1D magnet, $BaCu_2SiGeO_7$, acknowledged to be one of the best candidates for the physical realization of the RHC model. Our study included both experimental and numerical methods [3]. Based on extensive ^{29}Si NMR and magnetization measurements on $BaCu_2SiGeO_7$, combined with numerical Quantum Monte Carlo (QMC) simulations, we obtain *remarkable quantitative agreement* with theoretical predictions of the random Heisenberg-chain model, as well as strong evidence about the formation of a random-singlet state [2] at low temperatures in the spin chains of this compound.

As a local probe, NMR is a well-adapted technique for studying the magnetism of disordered systems. In this case, the results reveal the formation of an additional local transverse staggered field, which significantly affects the low-temperature properties of the RSS. The proposed model Hamiltonian satisfactorily accounts for the temperature dependence of the NMR line shapes and positions (see Fig. 3.1). Likewise, a comparison of the experimental data of the temperature- and field-dependence of the magnetization with QMC simulations of the magnetic response, reveal that our approach is superior to previously suggested models, which are inadequate in capturing the magnetism of randomly-disordered spin-chain systems.

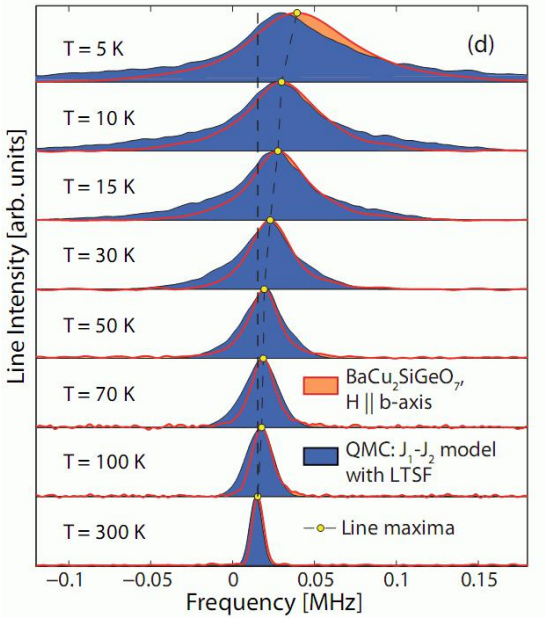

Figure 3.1: Simulated NMR line shapes (blue), as deduced from QMC simulations of an alternated J_1-J_2 model of a spin chain with 6000 sites placed in an external field of 7 T. The comparison with the ^{29}Si NMR experimental data (orange) shows an excellent agreement once the effects of a local transverse staggered magnetic field (induced by the main longitudinal field) are taken into account.

References

1. C. Dasgupta and S. K. Ma, Phys. Rev. B **22**, 1305 (1980).
2. D. S. Fisher, Phys. Rev. B **50**, 3799 (1994).
3. T. Shiroka, F. Casola, W. Lorenz, K. Prša, A. Zheludev, H.-R. Ott, and J. Mesot, Phys. Rev. B **88**, 054422 (2013).

3.2 Development of an all-digital NMR spectrometer

M. Pikulski, T. Shiroka, H.-R. Ott, and J. Mesot

Conventional nuclear-magnetic-resonance (NMR) spectrometers rely on analog components to down-convert the narrow-band high-frequency signals to frequencies which are suitable for data acquisition and analysis ($< 10\,\mathrm{MHz}$). Likewise, the synthesis and shaping of the excitation pulses usually requires dedicated circuits.

The recent availability of high-speed radioprocessor devices with user-accessible field-programmable gate arrays (FPGAs), however, offers an alternative approach. By employing this type of hardware, all the aspects of an NMR experiment, such as time structure (pulsing), signal synthesis, data acquisition, and down-conversion, are *exclusively* performed in the digital domain. This innovative concept offers several advantages. Most importantly, the absence of dedicated radio-frequency (RF) hardware allows for a fast replication of different measurement setups, while maintaining component reusability. Both these features encourage an easy implementation of an NMR setup in physics laboratories.

Following the ideas outlined above, we developed a firmware-defined NMR spectrometer in our laboratory. The spectrometer operates at frequencies up to $400\,\mathrm{MHz}$ and has a signal bandwidth of over $10\,\mathrm{MHz}$. The data with 16-bit resolution are processed in real-time using an on-board FPGA. Fast data transfers and high repetition rates are possible due to the use of a PCI Express interface. Finally, the signals are sampled directly, eliminating completely (except for amplification) analog signal processing. To our knowledge, our spectrometer is the first to combine all these characteristics in a single device.

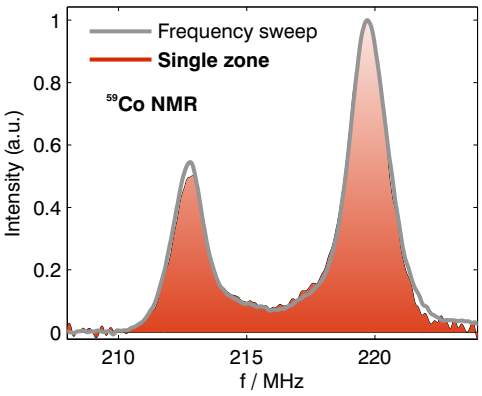

Figure 3.2: Zero-field ^{59}Co NMR spectrum in cobalt powder, measured at room temperature using the new digital spectrometer.

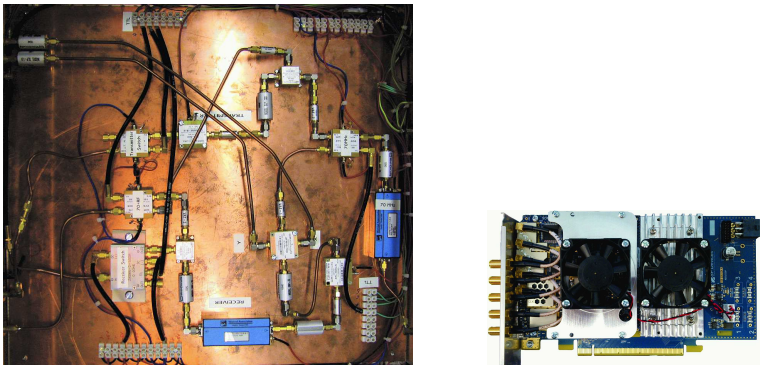

Figure 3.3: Hardware required for the construction of a conventional (left) and an all-digital (right) NMR spectrometer. The relative scaling is 1:2.

3.3 Symmetry of pairing in the optimally-doped BiS_2-based superconductors

T. Shiroka

in collaboration with G. Lamura and M. Putti (CNR-SPIN and Università di Genova, Italy)

P. Bonfà and R. De Renzi (Dipartimento di Fisica and Unità CNISM, Università di Parma, Italy)

J. Kajitani, Y. Mizuguchi, and O. Miura (Dept. of Electrical and Electronic Eng., Tokyo Metropolitan University, Japan)

K. Deguchi, S. Demura, and Y. Takano (National Institute for Materials Science, Tsukuba, Japan)

Next to the cuprate- and iron-based materials, BiS_2 compounds represent a recently discovered family of layered superconductors (SC) [1, 2]. A comparison with the existing classes of SC is particularly interesting in order to clarify the role played by the BiS_2 layers on the nature of the pairing mechanism in these compounds.

This comparison, however, relies on the knowledge of many key SC parameters such as: the type of pairing (s-, p-, or d-wave), its mechanism (phononic or via electronic correlations), the kind of gap (with or without nodes), the penetration-depth and the coherence-length values. By extensive zero- and transverse-field μSR experiments we traced the field- and temperature-behavior of $LaO_{0.5}F_{0.5}BiS_2$ and provide answers to most of the above questions [3].

Contrary to iron-based superconductors, we could not detect magnetically ordered phases in our case. The temperature and field dependences of the superfluid density suggest an s-wave character, compatible with a reduced isotropic SC gap, or a slightly anisotropic gap in the strong-coupling limit, in full agreement with theoretical predictions [4]. The very low superfluid density hints at a 2D character for the superconductivity also in the BiS_2 compounds.

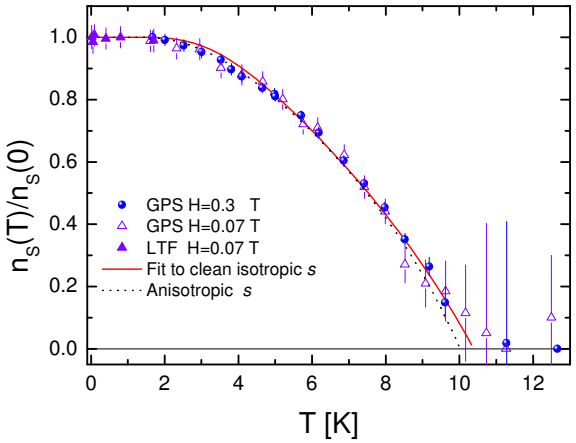

Figure 3.4: Temperature dependence of the normalized superfluid density (as from μSR penetration depth) at $\mu_0 H = 0.3\,\mathrm{T}$ (solid circles) and at 0.07 T (open triangles). The low-temperature ($T < 1.7\,\mathrm{K}$) data at 0.07 T are shown by solid triangles. The solid and the dotted black lines represent best fits to an s-wave gap in the clean limit and a numerical calculation with an s-wave anisotropic gap.

References

1. Y. Mizuguchi et al., Phys.Rev. B **86**, 220510(R) (2012).
2. S. Demura et al., J. Phys. Soc. Jpn. **82**, 033708 (2013).
3. G. Lamura, T. Shiroka, et al., Phys. Rev. B **88**, 180509(R) (2013).
4. X. Wan, H.-C. Ding, S. Y. Savrasov, and C.-G. Duan, Phys. Rev. B **87**, 115124 (2013).

Chapter 4

Nanoscale imaging, Nanoscale Magnetism

Head
Prof. Dr. D. Pescia

Academic Staff

L. De Pietro (PhD Student)	H. Cabrera (PhD student)	D. Zanin (PhD student)
Dr. U. Ramsperger (Postdoc)	Dr. A. Vindigni(Postdoc)	Prof. Dr. M. Erbudak

Technical Staff
Th. Bähler (80%)

Academic Guests
Prof. T. Gredig, Departement of Physics, California State University Long Beach,(01.10.-31.12 2013)

4.1 Field emission STM

The physical process leading to the emission of electrons from a sharp metallic tip placed at a well defined distance d from a planar electrode depends on d. If d is less than about 1 nm the current is produced by direct tunneling between emitter tip and planar collector. This type of tunnel junction is used e.g. in Scanning Tunneling Microscopy(STM). At larger distances, the current is dominated by electric field assisted tunneling of electrons into the region between emitter and collector through the classically forbidden zone. This is the type of junction underlying e.g. an instrument called the topographiner, a precursor of STM technology. One can also speak of STM in the field emission regime.

Achievements

1. We have continued our research on developing a new instrument based on field emission STM by reaching what we think is the ultimate lateral spatial resolution that can be achieved in this mode: 1 nm (see the Masterwork by Anna-Lena Redmann). A publication of this result is in preparation.

2. We have been able to perform energy resolved field emission STM by letting the secondary electrons emerging from the surface enter an energy selective analyzer. A publication of this result is in preparation.

3. **Scale invariance of a diodelike tunnel junction**

H. Cabrera, D.A. Zanin, L.G. De Pietro, Th. Michaels, P. Thalmann, A.L. Redmann, U. Ramsperger, A. Vindigni, D. Pescia, A. Kyritsakis and J.P. Xanthakis (Electrical and Computer Engineering Department, National Technical University of Athens, Zografou Campus, Athens 15700, Greece), Fuxiang Li and Ar. Abanov (Department of Physics, MS 4242, Texas A&M University, College Station, TX 77843-4242), Phys. Rev. B **87**, 115436 (2013)

We have systematically measured the current–voltage characteristics of a junction in the electric field assisted regime, whereby the distance d between tip and collector is varied from few millimeters to few nanometers. We observe that the family of curves describing the current I as a function of the two independent variables V *and* d can be "collapsed" onto one single scaling curve when I is plotted as a function of the single scaling variable $Vd^{-\lambda}$. This collapsing by a power law of d implies that the physical law governing the flow of current is invariant with respect to changes of the length scale d. We argue that the exponent λ originates within the solution of the Laplace equation of electrostatics in the vicinity of a singular point and undergoes crossovers to different values depending on whether d is comparable to the total length L of the tip, $d \ll L$ and, finally, whether d is comparable to the radius of curvature of the tip. A model of the tunneling process and of the electrostatic potential within the classically forbidden tunneling barrier for a "realistic" tip also shows both the experimentally observed scaling behavior and the experimentally detected small but significant deviations from scaling.

Chapter 5

Optical and Magneto-optical Spectroscopy

Head
Prof. Dr. L. Degiorgi

Academic Staff
Dr. C. Mirri
A. Dusza

Administrative Staff
I. Mettler

5.1 Excitation Spectrum in Ni- and Cu-doped $ZrTe_3$

C. Mirri, A. Duzsa and L. Degiorgi
work in collaboration with C. Petrovic, Brookhaven National Laboratory, Upton, U.S.A.

The coexistence as well as the competition of broken-symmetry ground states, like the prominent examples of charge-density-wave (CDW) and superconductivity (SC), have been ever since at the center of interest in solid state physics. Particularly in low-dimensional materials, the peculiar charge ordering, given by the CDW formation, and SC may be seen as specific quantum states originating from Fermi-surface instabilities, the interplay of which leads to interesting phase diagrams. This has led to a vigorous research activity also because the issue of their coexistence and competition has far more generic theoretical implications with respect to ideas foreseeing quantum criticality.

A revival of interest about issues related to the interplay of CDW and SC has emerged since the discovery of broken-symmetry, competing ground states in the pseudogap phase of the high-temperature superconducting cuprates. Indeed, the importance of CDW order in cuprates has been recently recognized on several occasions. The CDW instability in cuprates was found in close proximity to superconductivity. This is quite astonishing on its own, since the resistance-free movement of charge carriers in a superconductor may interplay with the rather opposite state characterized by spatial ordering of charges. This brings up the more general issue, whether such opposite states could macroscopically coexist or give rise to a phase separation in real space.

It is therefore of paramount relevance to study the emergence of SC from the CDW order, which motivated the search for new prototypical materials. The layered MX_2 as well as the chain-type MX_3 (M= transition metal and X=S, Se or Te) are well-known examples of CDW chalcogenide superconductors. The efforts in investigating chalcogenide superconductors have been motivated in part by the fact that they represent a weak coupling limit of melting of stripe (or smectic) order observed in cuprates. Furthermore, the intercalation by Ag, Cu and Ni of $ZrTe_3$ has been foreseen as an alternative to externally applied pressure in order to induce superconductivity. Recent reports on $Cu_{0.05}ZrTe_3$ and $Ni_{0.05}ZrTe_3$ single crystals indeed bring up evidence for bulk superconductivity below 4 K, apparently coexisting with a CDW state.

We provide an optical study of both Ni- and Cu-doped $ZrTe_3$, deploying their complete excitation spectrum with respect to both CDW and SC transitions. Even though the SC energy gap lies outside the measurable energy range of our laboratory-based infrastructure, we wish to approach the SC state from $T > T_c$ and its indirect signatures in the optical response (i.e., incipient onset of the SC gap) when measuring at $T \leq T_c$. It is of interest to establish whether SC is due to a dimensionality crossover upon doping, destabilizing the CDW and tipping the balance in favor of superconductivity, or if SC emerges from the CDW state because of electron count on doping. While the optical method, applied here, does not allow either a real or a reciprocal space resolution but rather an average and integrated view of the real space and Brillouin zone, respectively, it is nonetheless a further goal of this work to exploit the polarized electromagnetic radiation in order to approach the topic of competition/coexistence of broken-symmetry states. In fact, the polarization dependence of the optical conductivity gives direct access to the joint density of states reflecting the excitation spectrum for selected directions in real space. Since there are no indications so far for spatial phase separation in the title compounds, the presence of signatures for both collective states in the optical response for a specific polarization would mean that they coexist on a macroscopic scale along a preferential spatial direction but should separate in reciprocal space, such that the charge carriers of both condensates affect different portions or fractions of the Fermi surface.

The real part $\sigma_1(\omega)$, achieved via KK transformation of the measured optical reflectivity, is shown at 250 K from FIR to UV in the insets of Fig. 5.1 for the a- and b-axis. Along both polarization directions the MIR peaks at about 700 and 1000 cm^{-1} for the Ni- and Cu-doped $ZrTe_3$, respectively, strongly dominate the low frequency response, almost overcasting the metallic contribution of $\sigma_1(\omega \rightarrow 0)$. We may remark that $\sigma_1(\omega)$ along the b-axis is generally similar to the data collected on the parent $ZrTe_3$ compound, which is indeed expected, since intercalation only affects crystallographic directions perpendicular to the chain b-axis. For the Cu-doped $ZrTe_3$, the anisotropy in $\sigma_1(\omega)$ is particularly strong in the MIR and FIR spectral range. For the Ni-doped $ZrTe_3$, $\sigma_1(\omega)$ along both a- and b-axis has a limited energy interval between 2000 and 4000 cm^{-1}, where the conductivity goes to unphysical negative values.

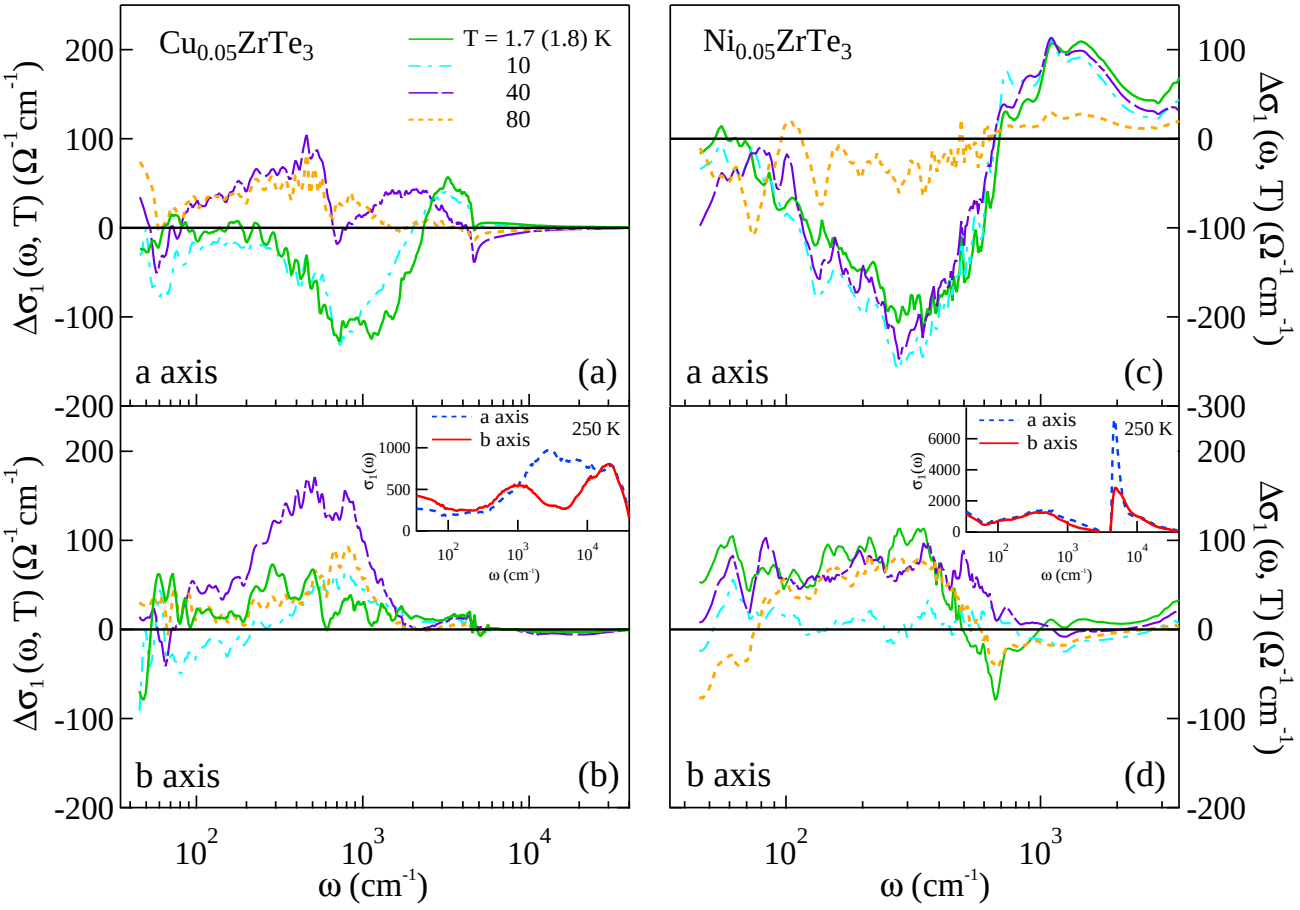

Figure 5.1: Relative difference $\Delta\sigma_1(\omega,T) = \sigma_1(\omega,T) - \sigma_1(\omega,100\text{ K})$ at selected temperatures below 100 K for both compounds and polarization directions. Insets (b) and (d): $\sigma_1(\omega)$ spectra at 250 K from FIR up to UV for both crystallographic axes. All panels and insets are in logarithmic energy scale. The lowest measured temperature was 1.7 K for the Cu-doped and 1.8 K for the Ni-doped $ZrTe_3$.

This is usually the case for materials affected by transparency, an aspect not properly taken into account by the KK transformations. As noticed most recently in $BaNi_2As_2$, this issue leads to overestimations of the phase shift and thus to incorrect values of both ϵ_1 and ϵ_2. However, we trust that, apart from the energy interval plagued by transparency, the features of interest are not badly affected, thus allowing some discussion. This is particularly true at low frequencies, well below the range affected by transparency, where the temperature dependence of $\sigma_1(\omega)$ evolves.

In order to emphasize the temperature dependence of $\sigma_1(\omega)$, we plot the relative difference $\Delta\sigma_1(\omega,T) = \sigma_1(\omega,T) - \sigma_1(\omega,$100 K) at selected temperatures for both compounds and polarization directions in the main panels of Fig. 5.1. We choose 100 K as reference temperature, since it is close enough to T_{CDW} and $\sigma_1(\omega)$ at this temperature can well represent the normal state situation, when approaching the transitions from high temperatures. This representation thus enhances the changes in the excitation spectra when crossing the CDW and superconducting phase transitions.

For the Cu-doped $ZrTe_3$, $\sigma_1(\omega)$ along the a-axis acquires intensity (i.e., $\Delta\sigma_1(\omega,T) > 0$) in FIR from 100 K down to 40 K prior getting depleted at 40 K below 100 cm^{-1} and even more so at 10 K. The trend of $\Delta\sigma_1(\omega,T)$ between 100 and 40 K may first indicate a piling up of spectral weight in an incoherent-like contribution to $\sigma_1(\omega)$ and second the narrowing of the effective metallic (Drude-like) component of $\sigma_1(\omega)$. At 10 K there is furthermore a strong depletion of $\sigma_1(\omega)$ below 2000 cm^{-1} (i.e., $\Delta\sigma_1(\omega,T) < 0$), which is quite reminiscent for the opening of a gap-like feature. The FIR depletion of $\Delta\sigma_1(\omega,T)$ at $T \leq 10$ K gives rise to the overshoot of $\Delta\sigma_1(\omega,T)$ between 2000 and 5000 cm^{-1}. We ascribe this depletion in $\sigma_1(\omega)$ to the CDW single-particle excitation ($2\Delta_{CDW}$). At 1.7 K ($T \sim 0.5T_c$), $\sigma_1(\omega)$ yet displays a similar depletion below 2000 cm^{-1} as at 10 K with a somehow steeper onset of the gap-like edge but tends to be more enhanced below 200 cm^{-1}. Within the measured spectral range we do not observe the fully developed SC-gap but there is evidence for an incipient down-turn of $\sigma_1(\omega)$ below 70 cm^{-1} instead of the Drude narrowing

observed at $T > T_c$. Along the b-axis, the incoherent part of $\sigma_1(\omega)$ at $T > T_c$ gets more strongly enhanced at 40 K. The depletion of $\sigma_1(\omega)$ (i.e., $\Delta\sigma_1(\omega, T) < 0$) appearing below 200 cm^{-1} at 10 K is possibly due to the narrowing of the metallic contribution or to a small CDW-induced effect along the b-axis. Except for that, there is no clear signature of CDW gap-like excitations. Similar to the a-axis response, $\sigma_1(\omega)$ at $T < T_c$ possibly hints to a down-turn below 60 cm^{-1}.

For the Ni-doped $ZrTe_3$, on the other hand, $\Delta\sigma_1(\omega, T)$ indicates the presence of a gap-like feature at 600 cm^{-1} along the a-axis, which opens up below 80 K and is fully developed from 40 to 1.8 K. This is again accompanied by the overshoot (i.e., $\Delta\sigma_1(\omega, T) > 0$) above 600 cm^{-1}. The narrowing of the metallic component moves outside our spectral range for $T < 80$ K. Along the b-axis, there is an enhancement of the incoherent part of $\sigma_1(\omega)$ below 600 cm^{-1} from 100 to 40 K. At 10 K we observe first a depletion of $\sigma_1(\omega)$, so that it is comparable to the data at 100 K, prior its enhancement in FIR when further lowering the temperature to 1.8 K. In the Ni-compound there is not any optical fingerprint of superconductivity along both axes in the spectral range covered by our experiment. Although SC in $Ni_{0.05}ZrTe_3$ is supposed to be more homogeneous than in Cu-doped $ZrTe_3$, the lower T_c may shift the onset of the SC gap, as observed in $Cu_{0.05}ZrTe_3$, totally outside our measurable spectral range.

In summary, the charge dynamics of the CDW state displays a polarization dependence within the ab-plane and gives evidence for a partial gapping of the Fermi surface, which affects almost exclusively the crystallographic direction parallel to the a-axis. The CDW transition reinforces a correlated state along the Zr-Zr chains, characterized by a narrow coherent Drude-like component in $\sigma_1(\omega)$ at low temperatures. While we cannot observe any clear-cut signature of the SC gap but at most an incipient onset (like in $Cu_{0.05}ZrTe_3$), our data indicate that, by assuming a homogeneous sample, the CDW and superconducting condensates seem to coexist in real space along the a-axis and consequently to affect separate regions in the reciprocal space.

Chapter 6

Solid-State Dynamics and Education

(http://www.eduphys.ethz.ch/)

Head
Prof. Dr. A. Vaterlaus

Academic Staff
Dr. Yves Marc Acremann
Dr. Audra Baleisis
Andreas Fognini
Rafael Gort
Andreas Lichtenberger
Dr. Thomas Uli Michlmayr
Gerard Salvatella Orgills
Dr. Guillaume Schiltz
Dr. Clemens Wagner

Master Students
Christian Stieger (HS2012)

Technical Staff
Thomas Bähler

6.1 E-Learning and teaching support

G. Schiltz

Strategic activities

27 lectures have been supplemented by the learning management system Moodle in 2013, reaching more than 4'000 students. Moodle was mainly used to support the course organization and to serve as a repository for course material. For some lectures, however, supplementary pedagogical scenarios, such as self-assessment tests, formative evaluations and collaborative tasks have been set up. More than 80 new episodes of the summary podcasts (audio/visual weekly summary) have been produced (6 lectures) and peer instruction was extensively used (8 lectures) as well. 2013 has been subject to a range of new teaching&learning activities:

- Participation to the TORQUE-initiative, which is the ETHZ interpretation of MOOCs (massive open online courses). Students in one physics service lecture (Danilo Pescia) were supplemented by weekly videos covering lecture topics.
- Online-assessment with multiple-choice questions. A compulsory midterm-test (Danilo Pescia) has been implemented as a proctored exam, where students use computers to fill-in their responses.
- Besides providing printed master-solutions, selected exercises have been supplemented with video recorded solutions (Leonardo Degiorgi). Videos offer better possibilities to explain, justify and illustrate the shown solution (fig. 6.1).
- Due to the repeal of the "Testat", exercise classes in three lectures (Wallraff, Wegscheider, Meyer) have been restructured as an exercise-market. Depending on their preference students now can choose between different types of exercise classes. Some classes focus on the lecture topics, some on the exercises. This new structure was highly approved by students and by teaching assistants.

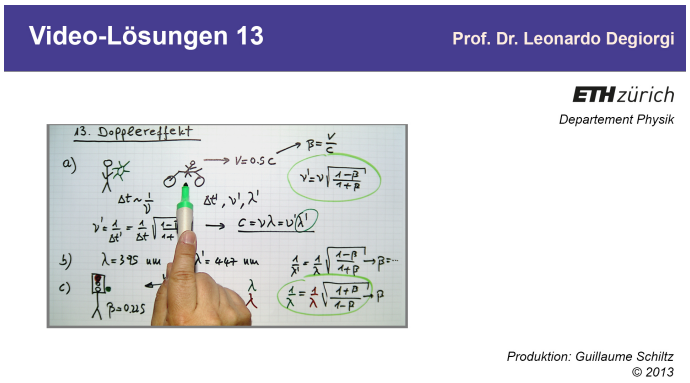

Figure 6.1: Video solutions (available from youtube, channel EduPhys)

Innovedum projects

The project on concept questions started in 2012 (Wallny) has successfully ended with a collection of 306 questions. Those concept questions are now used in several introductory lectures.

Promotion and Network

The teaching activities pursued at the department have been communicated to a greater public (2 presentations at international conferences, 1 community presentation).

6.2 Ultrafast magnetism

Y. Acremann

Demagnetization of a ferromagnet can be achieved on the 100 fs timescale by heating up a ferromagnet with an ultrashort laser pulse. Since the first observation by Beaurepaire et al. (PRL **76**, 4250 (1996)) no unifying explanation regarding the origin of this phenomenon could been established. The difficulty is to explain the ultrafast transport of spin angular momentum to the lattice. This problem is not only of great fundamental interest, but also of technological relevance: Future hard disk designs will use thermally assisted writing concepts in order to combine the long data retention time, small bit size and high writing speed requested by the user.

Laser system

A femtosecond laser system has been purchased, installed and commissioned. The femtosecond laser system consists of an oscillator, regenerative amplifier and pulse compressors. It delivers 1 mJ pulse energy with a pulse length of 25 fs and a repetition rate of 10 kHz. The relatively high repetition rate combined with a fourth harmonic generator is intended to be used for pump-probe experiments using photoelectron spectroscopy for detection. The system's low noise allows for time resolved magneto optical Kerr experiments. The laser system is operational and currently used in femtosecond pump-probe experiments using the magneto-optical Kerr effect to study magneto-dynamics.

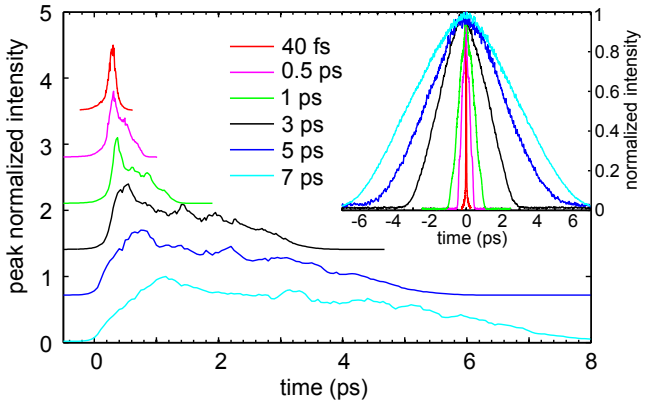

Figure 6.2: Pump pulses of variable length samples by probe pulses. The inset shows the auto-correlation of the pump pulses as a function of the auto correlation peak width.

Transport model of ultrafast demagnetization

We developed a model describing ultrafast demagnetization as a transport effect: The pump laser pulse causes a temperature gradient within the first surface layers of the sample. This gradient can be as large as 100 GK/m. The chemical potentials for minority- and majority electrons are altered by the temperature, leading to a gradient of the chemical potentials. It turns out, that the chemical potential of the majority electrons is affected most, leading to a chemical potential gradient, which favors a spin current from the hot surface towards the substrate. The spin current can be large enough to account for a significant part of the demagnetization effect. The model is similar in spirit to the super-diffusion model from Battiato et al. (PRL **105**, 027203 (2010)), yet it is based on a thermodynamic concept.

It therefore contains the basic process in an analytically solvable form. The model is tested by pump-probe Kerr experiments with variable pump pulse lengths and double pump pulses.

Spin detector

Together with the group of Prof. Schönhense (Uni Mainz) a novel spin detector was developed and tested. It allows for parallel detection of the spin polarization of electrons as a function of their emission angle and kinetic energy. We expect it to be significantly more efficient than the traditionally used Mott spin detector. We are currently building an improved version of the detector, which will be used for spin and time resolved photoemission experiments.

6.3 Physics Education

C. Wagner

Agent based simulation of group performance: diversity versus faultiness

In recent years agent based simulations of problem solving have received increased attention in order to find a better understanding of how the interactions between group members influence the group performance. Hong and Page (1) developed a model where single agents were trained to solve an optimization problem and then sorted due to their performance. Two groups were formed: a group consisting of the 10 best performers and a group where 10 agents were randomly selected from the pool. The performance of the group of best problem solvers is then compared to a group randomly selected from the set of all possible agents with different problem solving strategies. The outcome of the simulation was that the 10 best problem solvers perform worse on a new problem than the 10 randomly selected. The explanation for this result is due to the diversity of the group. Since the agents were trained on a specific problem the 10 best problem solvers use similar solution strategies. In contrast, the randomly selected group shows a much higher diversity and therefore performs better on a new problem. If we would like to apply the model to group work in education is has the drawback that the agents never make mistakes. Thus, in this work we investigate the effect of imperfect agents on the performance of the group using the optimization problem suggested by Hong and Page. The optimization problem is to find the maximum along a ring of 2000 numbers, which are between 1 and 100. Each agent has its own strategy to determine the maximum. The algorithm is designed in such a way that even the best agent never reaches the maximal, which would be 100. The minimum an agent can reach is the average over all numbers corresponding to 50.5. The results revealed that errors partially compensated the lack of diversity. Our simulation shows that the group of agents with a medium error probability but low diversity solves the optimization problem with the same performance as a group of perfect agents with high diversity (see Fig. 6.3). Moreover, the grade of the solution is equal to the grade of a group of randomly selected perfect problem solvers.

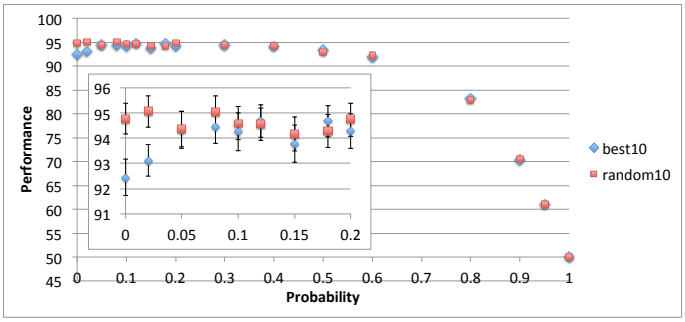

Figure 6.3: Performance versus error probability of agents. The performance of the low diversity group (diamonds) approaches with increasing probability the performance of the high diversity group (squares) for p approx. 0.1.

Fostering Concept Knowledge by Formative Assessment in High School Teaching of Physics

One of the major goals of formative assessment is to almost instantaneously evaluate students thinking and understanding of topics taught in class. In physics it is particularly important, that students grasp physics concepts right at the beginning of a new topic in order to get used to them and to learn how to apply these concepts in different contexts. Moreover, formative assessment is also helpful for the teacher since he can easily recognize if the students have understood the concept or not. In the latter case the teacher has to adapt the lessons to the level of understanding in class and to properly adjust teaching. To follow these ideas we have developed three strategies firstly, lectures have to be furnished with formative activities. These are activities, which allow for formative assessment. Secondly, students need to know whether they have understood the concept or not. Thus we designed a monitoring tool where students estimate their understanding of physics concepts. Thirdly, a diagnostic tool has been developed in order to evaluate studentÕs performance of conceptual problems. In our project formative activities are limited to clicker questions. The answering of a clicker question follows a strict procedure, which we think is important for the learning process and the understanding of physics concepts. During the formative activity student protocol their answers using the monitoring tool. It consists of a table to document the answers to the clicker questions and of a set of diagrams, for each concept one. The students also have to protocol if their answer is correct or not. The understanding of every concept is then illustrated in graph. For each correct answer the student moves one step up in the corresponding concept graph starting at zero and for a wrong answer one step down. There is a lower limiter at zero and an upper limiter, which depends on the number of questions asked. Therefore, if at the beginning the concept is not understood the student still has the chance to reach the top level (Fig. 6.4A lower panel). But also if the student got the concept at the beginning but starts to make mistakes maybe due to another concept the top level is left and the conflicting way of thinking is easily identified (Fig. 6.4 B lower panel).

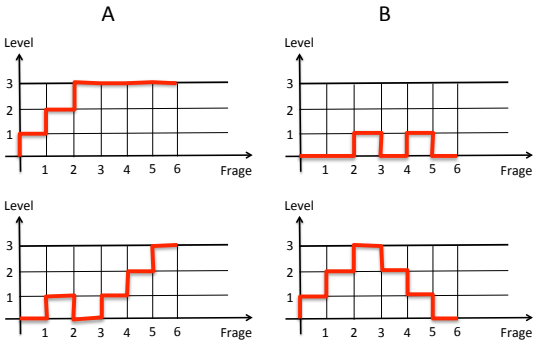

Figure 6.4: Monitoring tool for Clicker questions (x-axis: number of question, y-axis: level, which is related to the number of correct answers). The graphs represent possible time courses of student learning. (A) Students have learned the concept (upper panel: early learner; lower panel: late learner), (B) students are not able to apply the concept correctly (upper panel: concept never learned; lower panel: interfering concepts).

In our pilot study we have used our formative assessment approach in a Physics class at the Kantonsschule Romanshorn, where we have focused on the applicability of the monitoring tool. Three sets of clicker questions were developed with 12 questions each. We are in the process to validate the clicker questions in combination with the monitoring tool.

Analysis of Student Kinematics Concept Knowledge

We have developed a diagnostic test in kinematics to investigate the student concept knowledge at the gymnasium level. The 56 multiple-choice test items are based on seven basic kinematics concepts we have identified. We performed an exploratory factor analysis on a data set collected from 56 students at two Swiss high schools. For the analysis we used the program SPSS. We used the standard Pearson correlation function to calculate the correlation matrix and the maximum-likelihood method for the reduction. Before reducing the matrix, we determined the optimal number of factors using the eigenvalues of the correlation matrix in decreasing order. Scanning the graph from left to

right one can look for a knee. Then all the factors on the left of the knee are counted, while those factors, which fall in the ”scree” of the graph, are discarded (see Fig. 6.5).

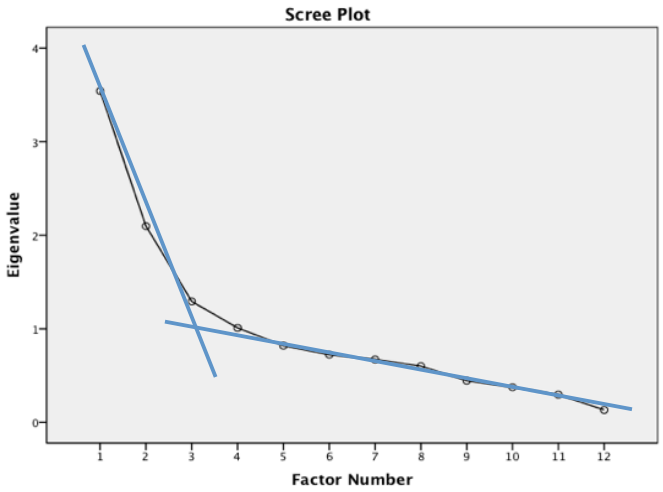

Figure 6.5: Scree Plot: The eigenvalues of the Pearson correlation matrix are depicted in decreasing order. The knee is between the factors three and four. This suggests a three-factor model.

The last step in factor analysis was to perform a rotation of the factor axes to see if there was another set of eigenvectors, which is more amenable to interpretation. We used this option choosing the prevalent Promax-method. The items can be analyzed at three levels of abstraction:

- Level A: Items with images (e.g. stroboscopic pictures)
- Level B: Items with tables of values
- Level C: Items with diagrams

The factor loadings for level A items are presented in Fig. 6.6.

Item	Factor			Corresponding Concept
	1	2	3	
2	.80			C1: Velocity as a rate
4	.75			
5	.95			
6		.38		C2: Velocity as a vector
7		.33		
8			.46	C3: Vector addition of velocities
9			1.01	
10			.42	
11	.57			C5: Acceleration as a rate
12	[.18]	[-.17]	[.18]	
13		.52		C6: Acceleration as a vector
14		.95		

Figure 6.6: Factor loadings for level A items.

From the data presented in Fig. 6.6 it is obvious that all items (except item 12) can be clearly assigned to one of the underlying factors. We note that all the items, which are grouped into factor 1, refer to the rate concepts C1 and C5. Furthermore, the items grouped into factor 2 refer to the vector concepts C2 and C6. Finally the items corresponding to concept C3 load on a separate factor 3. We may draw the conclusion that the association of items

seen by the students is in accordance with the association of questions seen by experts. Moreover the actual contents velocity and acceleration seem to play only a limited role. Much more relevant for answering the items correctly is the understanding of the mathematical concepts of rate and vector (including direction and addition). It is therefore tempting to interpret the underlying factors as ”rate concept”, ”direction concept” and “vector addition concept”.

Chapter 7

Quantum Device Lab

(http://qudev.ethz.ch/)

Head
Prof. Dr. A. Wallraff

Academic Staff

Dr. A. Abdumalikov	Dr. M. Allan	S. Berger
Dr. C. Eichler	M. Fadel	Dr. S. Filipp
Dr. T. Frey[1]	A. Hambitzer	L. Heinzle
C. Kern	P. Kurpiers	C. Lang
S. Miesch	J. Mlynek	Dr. M. Mondal
M. Oppliger	M. Pechal	Dr. G. Puebla-Hellmann
Dr. A. Safavi-Naeini	Y. Salathe	M. Stammeier
L. Steffen	A. Stockklauser	T. Thiele
A. van Loo	T. Walter	S. Zeytinoglu

[1]joint with Prof. Dr. K. Ensslin, ETH Zürich, Switzerland

Master Students

L. Hutmacher	L. Heinzle[2]	D.-D. Jarausch
P. Kurpiers	F. Lüthi	

[2]joint with Prof. Dr. O. Painter, California Institute of Technology, Pasadena, USA

Technical Staff

H. Aeschbach	S. Däster	J. Lütolf

Administrative Staff

Dr. F. Bay	G. Strahm

7.1 Experimental Realization of Non-Abelian Geometric Transformations

A. Abdumalikov, J. M. Fink, K. Juliusson, M. Pechal, S. Berger, A. Wallraff, and S. Filipp

Imagine, you plan for a Sundays hike along a splendid trail laid out in a figure-eight and you have to decide which of the two lobes you walk about first. Usually, it makes no difference and any choice leaves you afterwards in the same weary but contented state of mind. We have now demonstrated that in a quantum world you have to be more careful in your choice. Because of the non-abelian geometric effect the final state of a superconducting quantum device depends on which loop is traversed first.

The concept of non-abelian geometric transformations was introduced in 1984 by Wilczek and Zee. Despite intense theoretical study for almost 30 years, a clear experimental observation has been hindered by the prevailing constraints on slow, adiabatic evolution. We overcome these challenges, and the accompanying effects of decoherence, by realizing fast, non-adiabatic non-abelian geometric phases in a driven three-level superconducting artificial atom [1]. The variation of a single drive parameter leads to a deformation of the system's evolution path and results in non-commuting quantum operations which are analyzed by full process tomography shown in Figure 7.1. Applying two gates in series, we explicitly show – to our knowledge for the first time – their non-commuting character. Intriguingly, because such geometric operations depend only on the encircled area, but not on the evolution time, they may prove to be useful in realizing noise-resilient quantum algorithms based on solely geometric quantum operations.

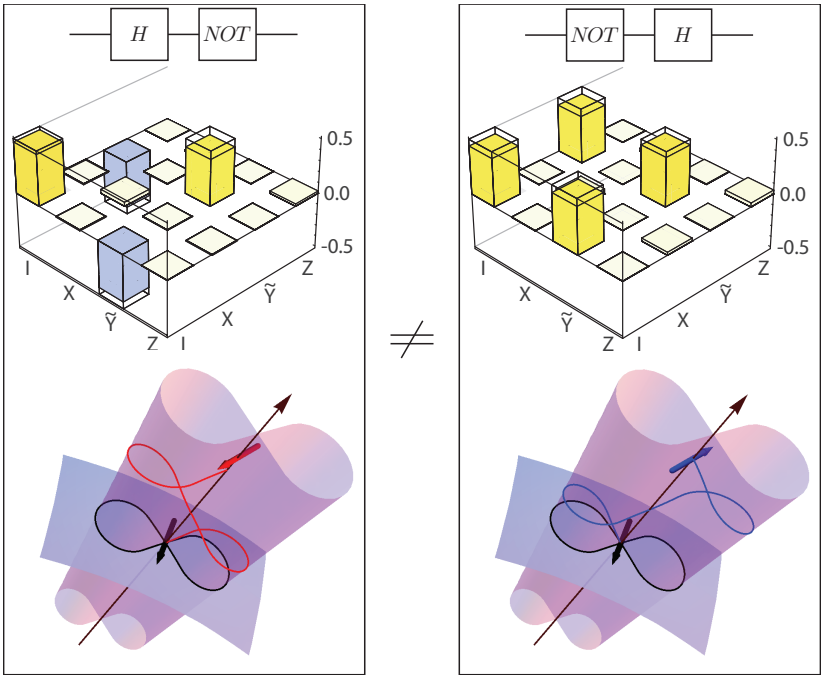

Figure 7.1: Process matrices of two geometric transformation executed in reverse order.

[1] A. A. Abdumalikov, J. M. Fink, K. Juliusson, M. Pechal, S. Berger, A. Wallraff, and S. Filipp, *Nature* **496**, 482 (2013)

7.2 Correlations, Indistinguishability and Entanglement in Hong-Ou-Mandel Experiments at Microwave Frequencies

C. Lang, C. Eichler, L. Steffen, J. M. Fink, M. J. Woolley, A. Blais, and A. Wallraff

We present a first measurement of the Hong-Ou-Mandel effect outside the domain of optical frequency photons. This genuinely quantum effect allows us to demonstrate the fundamental indistinguishability of single particles of light (photons) at microwave frequencies by measuring their coalescence into a photon pair at a beam splitter [1]. Our experiments open new possibilities for using this effect in quantum communication and information, e.g. for creating remote entanglement. The performed experimental analysis is one of the most complete and instructive studies of the Hong-Ou-Mandel effect performed in any physical system.

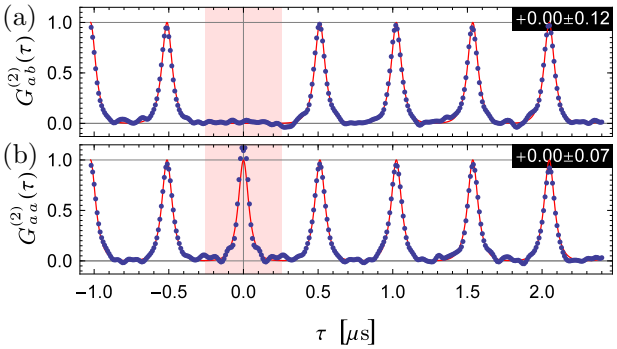

Figure 7.2: Second-order (a) cross- and (b) auto-correlation function measurements (dots) with theoretical expectations (lines).

In our experiments two individually triggered single-photon sources emit every $t_r = 512\,\mathrm{ns}$ two photons to the inputs of an on-chip beam splitter. For indistinguishable photons, which share the same frequency, temporal profile and arrival time, the two photons leave the beam splitter as a pair in either one of its two outputs. The generated state is the two-mode entangled two-photon NOON state $(|20\rangle + |02\rangle)/\sqrt{2}$.

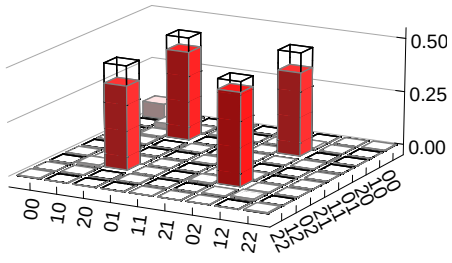

Figure 7.3: Real part of the measured density matrix (colored bars) compared to theoretical expectation (wire frame).

This is shown in the measurement of the second-order cross-correlation function displaying anti-bunching which proves that no photons are detected in both output arms of the beam splitter simultaneously ($\tau \approx 0$), see Figure 7.2(a). The bunching of the two photons is directly observed in the second-order auto-correlation function measurement, Figure 7.2(b). In both measurements at the times τ around $n\,t_r$ for all integer numbers $n \neq 0$ we observe the correlations between subsequent photon pairs that leave the beam splitter at random outputs. Finally, the measurement of the density matrix (Figure 7.3) demonstrates the entanglement of the two-mode state.

[1] C. Lang, C. Eichler, L. Steffen, J. M. Fink, M. J. Woolley, A. Blais, A. Wallraff, *Nat. Phys.* **9**, 345 (2013)

7.3 Exploring the Effect of Noise on the Berry Phase in Circuit QED

S. Berger, M. Pechal, A. A. Abdumalikov, Jr., C. Eichler, L. Steffen, A. Fedorov, A. Wallraff, and S. Filipp

A quantum mechanical system evolving under a time-dependent Hamiltonian acquires two kinds of phases: a dynamic phase, but also a geometric phase. The latter has the property of being independent of energy and total evolution time. This makes the geometric phase robust against certain fluctuations in the Hamiltonian [1,2].

In the present study, we build on our previous experiments where the adiabatic and cyclic geometric phase (termed Berry phase) was measured in a transmon-type superconducting qubit [3]. Here, the qubit is brought to acquire a geometric phase by applying an effective magnetic field $\mathbf{B}$ which describes a circle with constant B_z. Then, the Berry phase is half the solid angle enclosed by the loop described by the field. Fluctuations applied to this field in azimuthal direction [Fig. 7.4(a)] do not affect the Berry phase, and the coherence (the length of the qubit Bloch vector) is equal to one [green data in Fig. 7.4(c)]. However, fluctuations applied in radial direction [Fig. 7.4(b)] change the Berry

phase and the coherence diminishes [blue data in Fig. 7.4(c)]. For a system with known noise characteristics, the loop can be engineered to minimize the influence of noise on the Berry phase.

In order to compare the resilience of the dynamical phase and the Berry phase against noise, the coherence of the qubit was measured as a function of the total evolution time τ, cf. Fig. 7.4(b). The same noise was applied to measurements of both dynamic and Berry phase. The data presented in Fig. 7.4(d) show that the coherence of the dynamic phase decreases rapidly as τ increases. In contrast, the coherence of the Berry phase is seen to increase slightly with τ. This can be explained intuitively: As τ gets larger, the fluctuations in the effective magnetic field will lie equally inside and outside the undisturbed magnetic field, and therefore cancel each other out. As a consequence, the influence of the noise diminishes.

In future experiments, we plan to analyze the noise-resilience of non-adiabatic geometric gates, allowing for faster quantum gates, and to explore the feasibility of purely geometrical quantum algorithms.

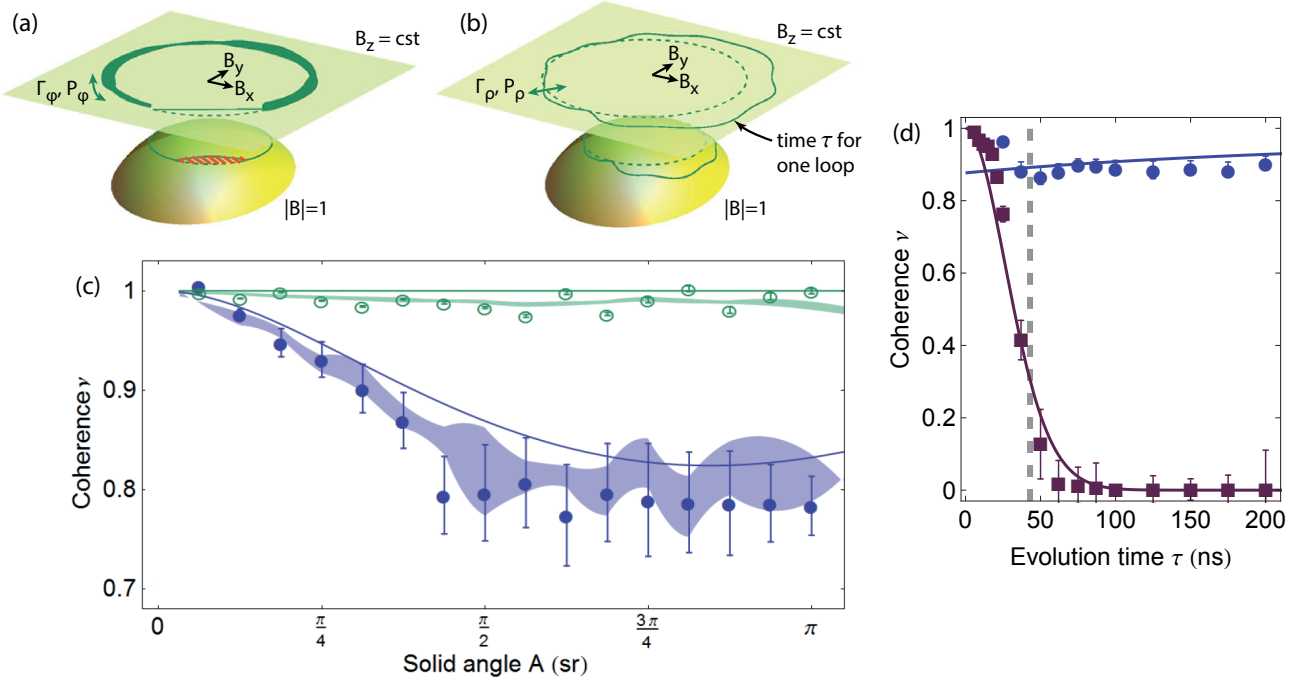

Figure 7.4: (a,b) The path of the effective field without noise (dashed green lines lying in the plane with constant B_z) is drawn alongside the same path exposed to two kinds of noise (solid green lines): angular noise in (a), where the velocity of precession is proportional to line thickness, and radial noise in (b). The projection of the paths on the unit sphere $|\mathbf{B}| = 1$ is also shown. (c) Coherence of the Berry phase as a function of solid angle for radial noise (blue circles) and angular noise (green circles). Experimental data points are shown alongside theory (solid lines) and the results from numerical simulations (shaded area indicates the standard deviation about the mean). (d) Coherence of the Berry phase (blue circles) and of the dynamic phase (purple squares) versus evolution time. The solid lines result from theory. The dashed grey line approximately separates the non-adiabatic from the adiabatic regime.

[1] G. De Chiara and G. M. Palma, *Phys. Rev. Lett.* **91**, 090404 (2003)

[2] S. Filipp, J. Klepp, Y. Hasegawa, C. Plonka-Spehr, U. Schmidt, P. Geltenbort, and H. Rauch, *Phys. Rev. Lett.* **102**, 030404 (2009)

[3] S. Berger, M. Pechal, S. Pugnetti, A. A. Abdumalikov Jr., L. Steffen, A. Fedorov, A. Wallraff, and S. Filipp, *Phys. Rev. B* **85**, 220502(R) (2012)

7.4 Deterministic Quantum Teleportation with Feed-Forward in a Solid State System

L. Steffen, Y. Salathe, M. Oppliger, P. Kurpiers, M. Baur, C. Lang, C. Eichler, G. Puebla-Hellmann, A. Fedorov, and A. Wallraff

Figure 7.5: In our chip-based superconducting circuit three qubits are coupled to three resonators to realize deterministic quantum teleportation.

Transferring the state of an information carrier between two parties is an essential primitive in both classical and quantum communication and information processing. Quantum teleportation describes the concept of transferring an unknown quantum state from a sender to a physically separated receiver without transmitting the physical carrier of information itself. Instead, teleportation makes use of the non-local correlations provided by an entangled pair shared between the sender and the receiver and the exchange of classical information. We have teleported information for the first time in a solid state system. In our chip-based superconducting circuit architecture we have realized the full deterministic quantum teleportation protocol using quantum-limited parametric amplifiers, a crossed quantum bus technology and flexible real-time digital electronics. The teleportation process succeeds with order unit probability for any input state, as we reliably prepare entangled states as a resource and are able to distinguish all four maximally entangled Bell states in a single measurement.

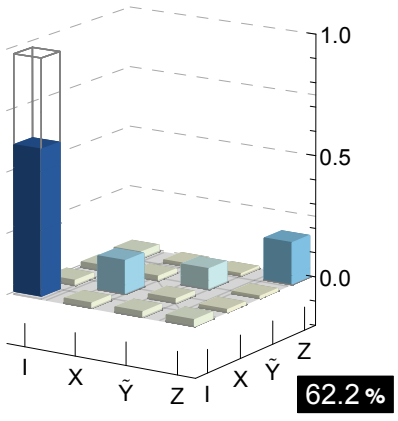

Figure 7.6: The solid bars show the experimentally obtained process matrix describing the state transfer from the sender to the receiver. The ideal process matrix, which is the identity operation, is shown by wire frames.

The success of the teleportation protocol in every instance with unit fidelity is counterintuitive from a classical point of view. The receiver's quantum bit (qubit) does not interact with any other qubit after it has been entangled with one of two qubits in the senders possession. The input state ($|\psi_{\mathrm{in}}\rangle$) is prepared afterwards at a second qubit in possession of the sender. The classical information sent by the sender is not sufficient to recreate $|\psi_{\mathrm{in}}\rangle$ perfectly at the receiver. Indeed, assuming no entanglement between sender and receiver one can replicate the sender's state at best with a process fidelity of $1/2$. To always recover the original state $|\psi_{\mathrm{in}}\rangle$ the sender performs a measurement in the basis of the Bell states, which projects the two qubits in the sender's possession randomly onto one of the four Bell states. As a consequence the receiver's qubit is projected instantaneously into a state related to $|\psi_{\mathrm{in}}\rangle$ without ever having interacted with the senders qubit. The receiver's qubit only differs from the input state by a single-qubit rotation which depends on the four possible measurement results. In the final step, the sender communicates the Bell measurement result as two bits of classical information via a classical channel and therefore the receiver can always obtain the original input state $|\psi_{\mathrm{in}}\rangle$. This final step is frequently referred to as feed-forward.

To identify simultaneously the four outcomes of the Bell-state measurement in a deterministic way we use two-qubit single-shot read-out for which we achieve a success probability of $(81.8 \pm 0.5)\,\%$. In the teleportation protocol we analyze the Bell-state measurement in real time by using fast electronics based on a field programmable gate array (FPGA) and realize the feed-forward step in about $500\,\mathrm{ns}$. We have achieved an average process fidelity of $(62.2 \pm 0.3)\,\%$ for the full quantum teleportation algorithm, which is clearly above the classical threshold (Fig. 7.6). We have demonstrated teleportation at a rate of 10,000 quantum bits per second between two macroscopic systems separated by $6\,\mathrm{mm}$.

[1] L. Steffen, Y. Salathe, M. Oppliger, P. Kurpiers, M. Baur, C. Lang, C. Eichler, G. Puebla-Hellmann, A. Fedorov, and A. Wallraff. *Nature* **500**, 319-322 (2013)

7.5 Single-Electron Double Quantum Dot Dipole-Coupled to a Single Photonic Mode

J. Basset, D.-D. Jarausch, A. Stockklauser, T. Frey, C. Reichl, W. Wegscheider, T. M. Ihn, K. Ensslin, and A. Wallraff

Recent theoretical work on coupling semiconductor quantum dots with superconducting transmission line resonators has promised novel research avenues towards a well-controlled coherent interface between electronic quantum dot excitations and quantized microwave frequency fields. On the experimental side, pioneering experiments [1] have demonstrated electrical dipole coupling between electrons confined in quantum dots and microwave photons stored in a resonator by measuring dispersive and dissipative effects in the resonant transmission of photons through the resonator. These experiments demonstrated a quantum dot cavity coupling up to 50 MHz, much smaller than the extracted decoherence rates of $1-3$ GHz. Further research is now needed to reduce the decoherence rate to such an extent that the strong coupling regime can be reached [2]. In particular, one of the suspicions put forward in previous work has been that low-energy excitations in a many-electron quantum dot could increase both dephasing and energy relaxation rates of the coupled system compared to the one-electron case. In our recent experiment we have explored the single-electron regime of a double quantum dot coupled to a strip-line resonator for which the internal excitation energies in the double quantum dot system are larger than in the many-electron regime [3]. We performed a quantitative comparison of dephasing rates in the single- and the many-electron regimes within the same device. Our results show that the dephasing rates of the double quantum dot cannot be reduced significantly by working in the single-electron regime. However, the quantitative comparison of the inter-dot tunneling rates, determined either using a quantum point contact based charge detector or the resonator using the Jaynes-Cummings model demonstrates that both methods agree very well.

In future experiments, we plan to optimize our dot/resonator coupling, use the spin-degree of freedom as a natural quantum bit with micro-magnets and analyze the link between the statistics of electron tunneling through the dots and the statistics of the microwave radiation emitted during out-of-equilibrium transport processes.

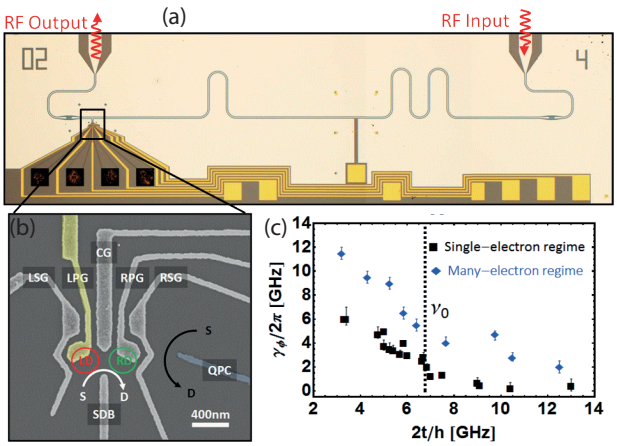

Figure 7.7: (a) Optical microscope picture of a superconducting transmission line resonator coupled to a semiconductor double quantum dot. A careful analysis of its transmission allows us to extract the dephasing properties of the dots-based charge qubit. (b) Scanning electron microscope picture of the e-beam defined split gate design used to define the qubit and readout the dots' charge state. (c) Dephasing rates $\gamma_\varphi/2\pi$ *vs* tunnel coupling between the dots t of the charge qubit in the single- and many-electron regimes. The dephasing rates are roughly reduced by a factor of 2 when lowering the number of confined electrons.

[1] T. Frey, P. J. Leek, M. Beck, A. Blais, T. Ihn, K. Ensslin, and A. Wallraff, *Phys. Rev. Lett.* **108**, 046807 (2012)

[2] J. Raimond, M. Brune, and S. Haroche, *Rev. Mod. Phys.* **73**, 565-582 (2001)

[3] J. Basset, D.-D. Jarausch, A. Stockklauser, T. Frey, C. Reichl, W. Wegscheider, T. M. Ihn, K. Ensslin, A. Wallraff, *Phys. Rev. B* **88**, 125312 (2013)

7.6 Photon-Mediated Interactions between Distant Artificial Atoms

A. F. van Loo, A. Fedorov, K. Lalumière, B. C. Sanders, A. Blais, and A. Wallraff

Suppose you leave your house in Zurich early in the morning, and you set off walking in a random direction, without a compass, GPS or looking at the signs. What is the probability of ending up in your lab at ETH Zurich's Hoenggerberg Campus? And what is your probability of ending up for example at the ETH main building? Either one is not very high, certainly. Now suppose you wake up in a tunnel directly connecting the two sites. How does this affect your chances to end up at either place?

Wanting to investigate the interactions between atoms in an open space caused by the exchange of photons, we realized that these interactions would likewise be greatly increased by putting the atoms and photons in a purpose-made tunnel. Superconducting qubits were used as artificial atoms and a coplanar waveguide transmission line as the tunnel. The qubits are physically separated by about 2 centimeters, but the separation between the qubits in units of their transition wavelength (λ_r) can be varied by tuning their transition frequencies. In this way, we have varied the effective distance between the qubits from $3\lambda_r/4$ to λ_r.

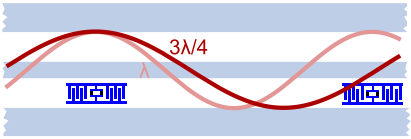

Figure 7.8: In a transmission line photons are forced to travel along the line connecting the two qubits, mediating interactions between the two. By tuning the qubit emission wavelength we tune the effective distance between two qubits.

We have demonstrated for the first time that strong interactions between two distant superconducting qubits in an open environment can be observed. When the two qubits are separated by multiples of $\lambda_r/2$, we observe the formation of super- and subradiant states. The subradiant state was found to have a lifetime more than 100 times as long as the lifetime of the superradiant state. For perspective, in initial experiments showing similar effects in ions, the subradiant state lived about 1.03 times as long as the superradiant state. Finding a two-qubit state in an open environment with a lifetime two orders of magnitude longer than a single qubit suggests that these systems could potentially be used as a quantum memory.

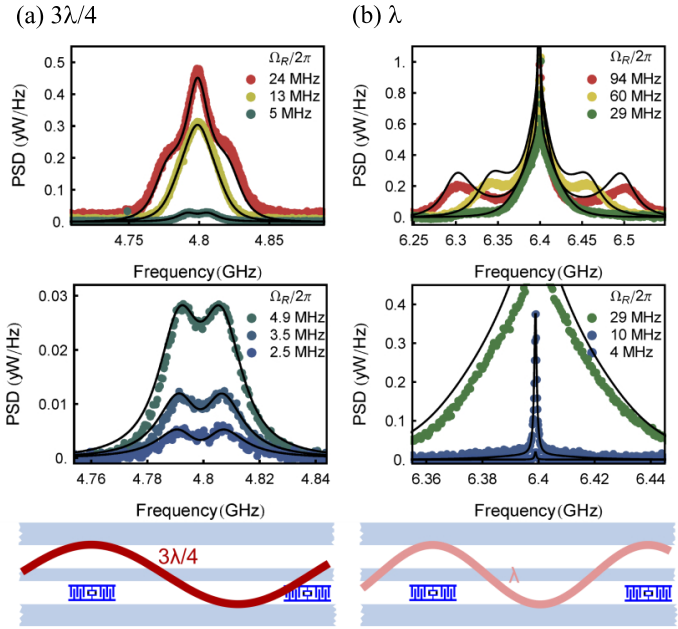

Figure 7.9: Interaction effects are revealed when measuring resonance fluorescence. An exchange splitting is seen at qubit separations of $3\lambda_r/4$ (a), while super- and subradiant states with drastically different lifetimes form for qubits separated by λ_r (b).

Furthermore, when the qubits are separated by odd multiples of $\lambda_r/4$, an exchange interaction between the qubits emerges which is mediated by the vacuum fluctuations of the 1D continuum at all frequencies. To our knowledge, our

work presents the first observation of an exchange-type interaction mediated by photons over larger distances, i.e. the first instance of quantum systems interacting coherently at a distance, in a free space [1]. We find good agreement of our experimental findings with the theory [2].

[1] A. F. van Loo, A. Fedorov, K. Lalumière, B. C. Sanders, A. Blais, and A. Wallraff, *Science* **342**, 1494-1496 (2013)

[2] K. Lalumière, B. C. Sanders, A. F. van Loo, A. Fedorov, A. Wallraff, and A. Blais, *Phys Rev A* **88**, 043806 (2013)

Chapter 8

Semiconductor Quantum Materials

(http://www.mbe.ethz.ch/)

Head
Prof. Dr. W. Wegscheider

Guest Professor
Prof. Dr. W. Dietsche

Academic Staff

Ch. Charpentier	Dr. S. Fält	Dr. T. Feil
Ch. Lehner	A. Maier	S. Peters
Ch. Reichl	S. Riedi	Dr. W. Stumpf
Dr. L. Tiemann	T. Tschirky	W. Wüster

Master Students
M. Locher (FS2013)
T. Tschirky (FS2013)
D. Wenzler (HS2013)

Technical Staff

J. Gmür	S. Heider	M. Sturzenegger

Secretaries

C. Egli	C. Vinzens

8.1 Raman spectroscopy in the quantum Hall regime

T. Feil, S. Fält, W. Wegscheider

In order to investigate correlated electron states via optical excitations it is necessary to develop semiconductor heterostructures that show stable electron properties under constant weak illumination. This stability can for example be monitored by simultaneous measurement of the electron system's transport properties. In principle, the optical excitation power is low enough that for reasonable recombination times the electron density of the system should stay unchanged for all practical purposes. However, trap states in the molecular-beam-epitaxy grown samples can lead to charging effects where constant charge accumulation leads to significant, time dependent changes in the electron density. We have studied different procedures for cooling and illuminating samples in order to achieve stable sample properties under illumination. Fig.8.1 compares a specially designed heterostructure with transparent backgate during two different cooling and illumination procedures. Procedure 1, as shown in Fig.8.1a, results in an optimal situation. Under illumination, the positions of quantum Hall plateaus and of the longitudinal resistance minima are unchanged with respect to the not illuminated case. The difference in width of the Hall plateaus and the less pronounced longitudinal resistance minima are consistent with an expected heating of the electron system under illumination. However, Fig.8.1b shows that the sample history plays a vital role in reaching a stable configuration. Here, transport measurements in the dark and under illumination show a strong shift in electron density during optical excitation. This change in density is usually intensity dependent.

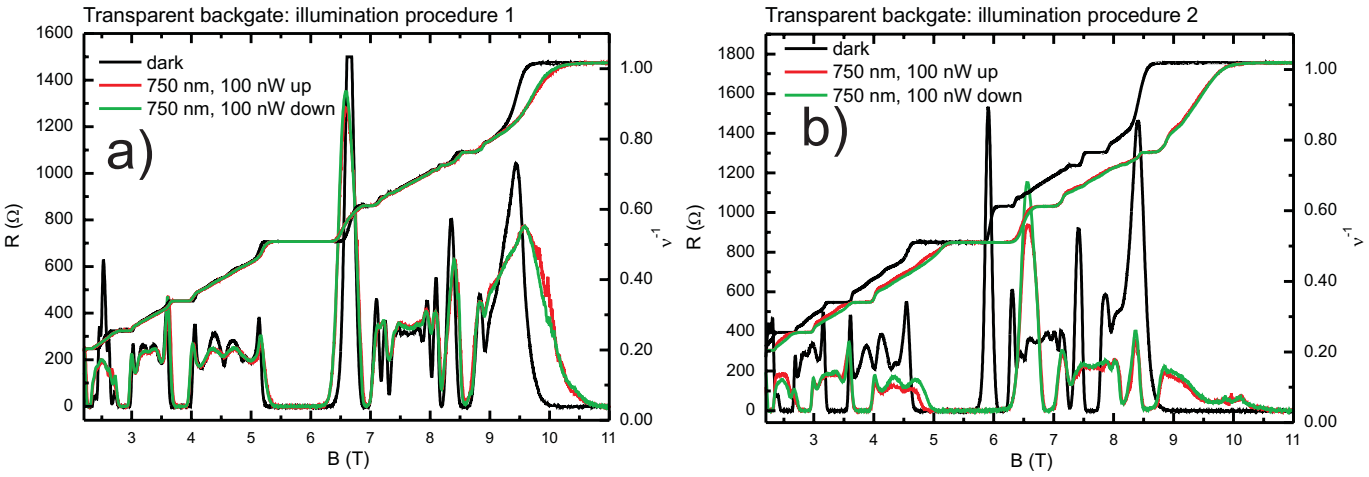

Figure 8.1: Comparison of transport traces in the dark and under illumination of the same sample under two different cooling/illumination procedures.

8.2 Quantum Hall effects in Aluminium Gallium Arsenide

L. Tiemann, C. Reichl, W. Wegscheider

In recent years, new materials such as Graphene or ZnO emerged and have been competing with the established GaAs/AlGaAs heterostructures in studying the quantum Hall effects. Growth of these new materials, however, is often challenging and in the case of Graphene for example, it still often relies on mechanical ablation of single 2D sheets by hand. In contrast, a quantum well of pure aluminium arsenide (AlAs) can be grown with little adjustment in the same MBE systems being used for standard high-mobility GaAs growth. Like in silicon, electrons populating a AlAs quantum well occupy degenerate valleys at the edge of the Brillouin zone. The resulting anisotropic effective electron mass make AlAs an interesting material for mesoscopic physics and collective phenomena.

Within the past 12 months, AlAs growth has been established and quickly improved, currently yielding top electron mobilities exceeding 500,000 cm^2/Vs. A remarkable aspect of AlAs is the ability to lift the valley degeneracy and tune the valley population via application of strain to the sample. Figure 8.2 illustrates the underlying concept, where strain is applied by a piezoelectric element. The adjacent energy level diagram shows the valley splitting E_{Valley} which intrinsically depends on the amount of strain applied to the sample.

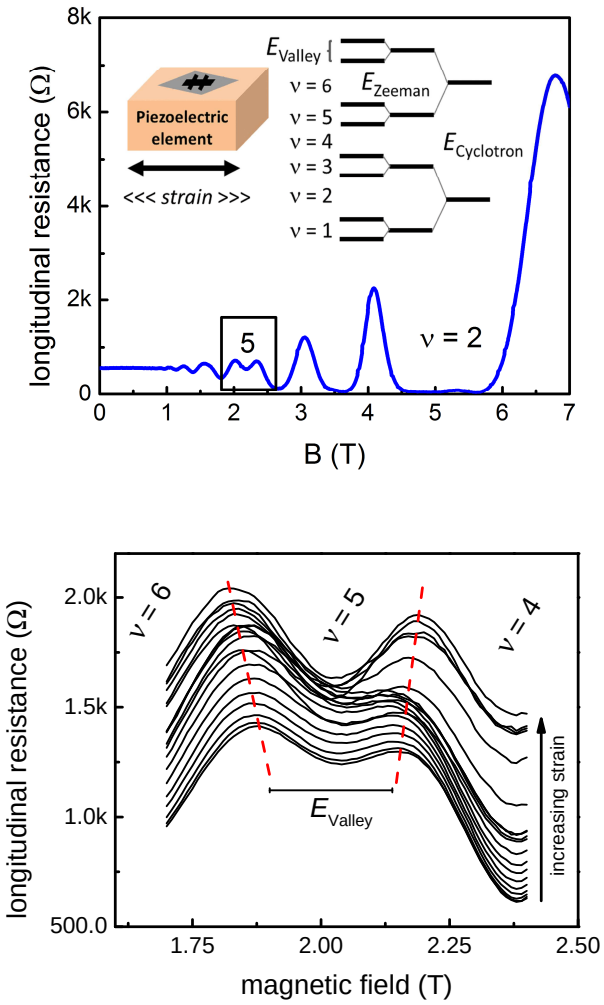

Figure 8.2: top: Magneto-transport on a thinned and back-gated AlAs sample. The inset shows the setup and a simplified energy diagram. bottom: magnification of the range between filling factors ν=4 through 6, i.e., the valley splitting, which depends on the applied strain by the piezoelectric element underneath the sample.

8.3 Optimizing cleaved edge overgrowth for charge and spin transport devices

A. Maier, S. Riedi, D. Wenzler, W. Wegscheider

We employ the cleaved edge overgrowth technique (CEO) to fabricate ballistic GaAs quantum wires and lateral pn-junctions for spin transport measurements defined by MBE precision. Although the method was introduced some years ago, the fabrication of in-situ cleaved atomically flat interfaces remains highly challenging. In order to control and improve the quality of the cleaved surfaces, it is necessary to have a comprehensive understanding of the complex features of the scratching and cleaving process in III-V semiconductors. Extensive lab studies and discussions with K. Wasmer, fracture mechanics expert of EMPA Thun, helped to identify relevant parameters and depicted technical

measures for improvement within the boundaries given by the setup. In principle, it is also conceivable to apply the CEO technique on heterostructures based on different III-V materials than GaAs, e.g. the InAs/AlSb system. To our knowledge, no efforts have been made so far in this direction. Chemical thinning of the wafer material to less than 100 μm is typically achieved using a bromine-methanol solution. This process is well established for GaAs and shows good results for GaSb, although edge rates are much higher. However, it seems to be more difficult to realize good quality cleaving with GaSb, despite the fact that fracture toughness values are smaller than for GaAs.

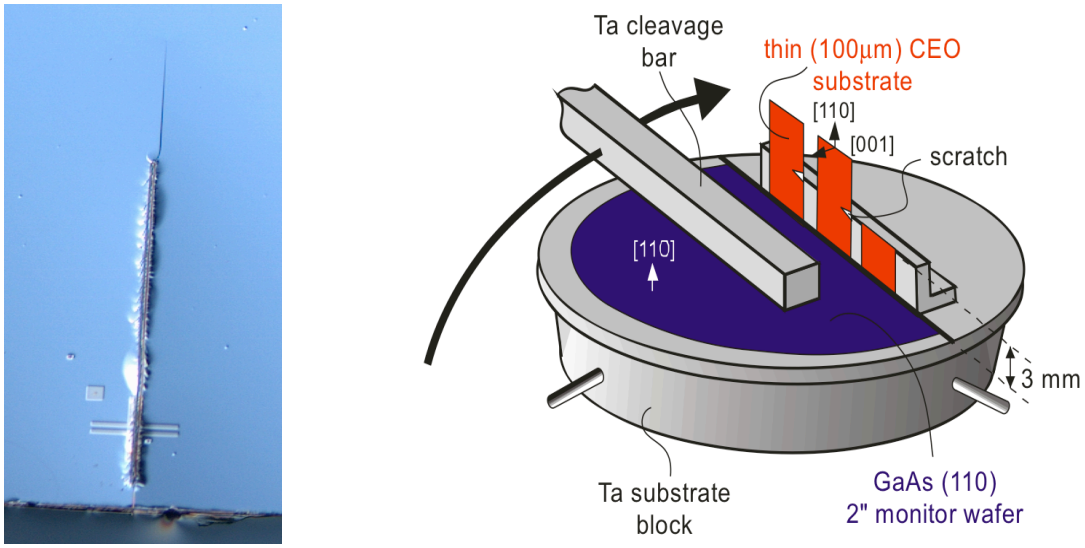

Figure 8.3: left: A scratch mark (1 mm long) on a GaAs sample initiates a fine median crack along the $\{110\}$ preferential cleveage plane. right: Scheme of cleaving process inside the MBE chamber at the predetermined breaking points.

8.4 GaAs/AlGaAs heterostructures for optical devices

S. Fält, W. Dietsche, D. Wenzler, F. Schläpfer, W. Wegscheider

For highly confined photons strongly interacting with an active medium, the excitations in the active medium cannot be distinguished from the photons. The combined state is then rather described as polaritons. This system is commonly realized in semiconductors by monolithically integrating a number of quantum wells (QWs) in a microcavity, where the cavity mirrors are distributed Bragg reflectors (DBR) grown from the same material as the QWs. We produce these microcavity structures with GaAs/AlGaAs QWs and AlGaAs/AlAs DBRs. It requires a high number of relatively thick layers, resulting in high consumption of source material. A new MBE system has been installed with the same design as the other high-mobility MBE in the group. In this system, significantly more of the high-purity Ga was loaded, allowing us to compensate for the high material consumption. While the highest mobility of a structure grown so far is 8E6 cm^2/Vs, we have grown undoped GaAs/AlGaAs QWs with this chamber having a photoluminescense peak with full width at half maximum (FWHM) of 130 μm (to be compared to the same structure with FWHM of 220 μm, reported by J. R. Jensen et. al. APL 76, 3262). This shows that we have good control of the optical emission properties of the material. It is also crucial to optimize the growth of the passive part of the structure, i.e. the DBR. This is mainly determined by how well an exact growth rate can be maintained. For this, we are currently building up an optical monitoring system to measure the growth rate in-situ.

8.5 Cavity quantum electrodynamics in the quantum Hall regime

W. Wüster, S. Smolka, F. Haupt, S. Fält, A. Imamoglu, W. Wegscheider

By embedding a high mobility two dimensional electron gas (2DEG) into a cavity defined by a stack of MBE grown distributed Bragg reflectors (DBR), we combine the fields of quantum Hall physics and cavity quantum electrodynamics. Tuning the cavity into resonance with the optical interband transitions between spin resolved Landau levels of the electron conduction band and the hole valence band, leads to the emergence of polariton modes in the strong coupling regime. We term these modes "quantum Hall polaritons" and observe a dependence of the normal mode splitting (NMS) on the electron filling factor of the 2DEG. We find a strong reduction of the NMS around filling factor $\nu = 1$, where the electrons completely occupy the energetically lowest spin state of the lowest Landau level. We attribute our findings to the degree of spin polarization of the 2DEG, using the NMS as spectroscopical tool of spin polarization.

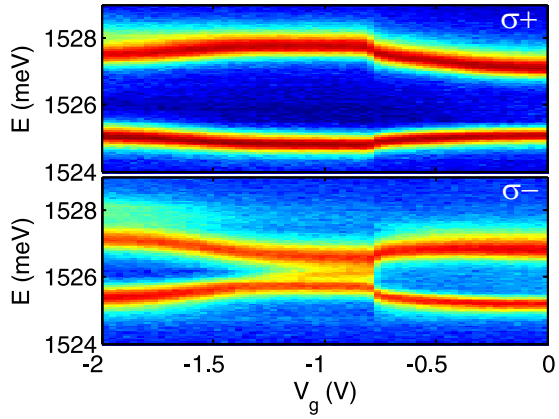

Figure 8.4: Polarization-resolved reflectivity measurements as function of the applied gate voltage between top gate and 2DEG. In the vicinity of filling factor $\nu = 1(-1.5V < V_g < -1V)$ one observes a reduction in the NMS for σ^- and an enhancement for σ^+ polarized light. As the two light polarizations probe different spin occupations of the 2DEG we expect a vanishing NMS in σ^- for a completely spin polarized $\nu = 1$ state and a recovery for filling factors larger and smaller than $\nu = 1$ due to spin depolarization that is caused by skyrmions.

8.6 High-mobility Sb-based III/V semiconductor heterostructures

C. Charpentier, T. Tschirky, C. Lehner, W. Wegscheider

Sb-based III/V semiconductor heterostructures offer a wide range of interesting physical properties like the very high barriers (1.35 eV) and low effective electron mass ($0.023\,m_e$) in InAs/AlSb quantum wells, the broken gap band alignment in InAs/GaSb/AlSb composite quantum wells (CQWs) and the extremely low electron mass ($0.014\,m_e$) and very high g-factor ($g^* = -51$) in InSb/AlInSb quantum wells. In the past year, our group further optimized the fabrication of InAs/GaSb/AlSb composite quantum wells and was able to propose a new scheme for the suppression of bulk conductivity in these structures which is one of the main obstacles to the observation of helical edge channels in the Quantum Spin Hall State [C. Charpentier, S. Fält, C. Reichl, F. Nichele, A. Pal, P. Pietsch, T. Ihn, K. Ensslin, and W. Wegscheider, Appl. Phys. Lett. **103**, 112102 (2013)]. In Figure 8.5, we show the longitudinal resistivity of such structures, measured at 70 mK for different top gate voltages and magnetic fields from 0 to 12 T. Together with the group of Prof. Ensslin, the behavior of the InAs/GaSb/AlSb CQWs at high magnetic fields was studied and strong signs for the helical nature of the edge channels could be found [F. Nichele, A. Pal, P. Pietsch, T. Ihn, K. Ensslin, C. Charpentier, and W. Wegscheider, Phys. Rev. Lett. **112**, 036802 (2014).]. Further achievements of our group in 2013 include the substantial reduction of the surface roughness of InAs/AlSb structures by the optimization of a large set of growth parameters, the investigation of interface sharpness by Fourier Transform Infrared Spectroscopy (Master Thesis of T. Tschirky) and the development of new strategies for the successful fabrication of high-quality InSb/AlInSb quantum wells.

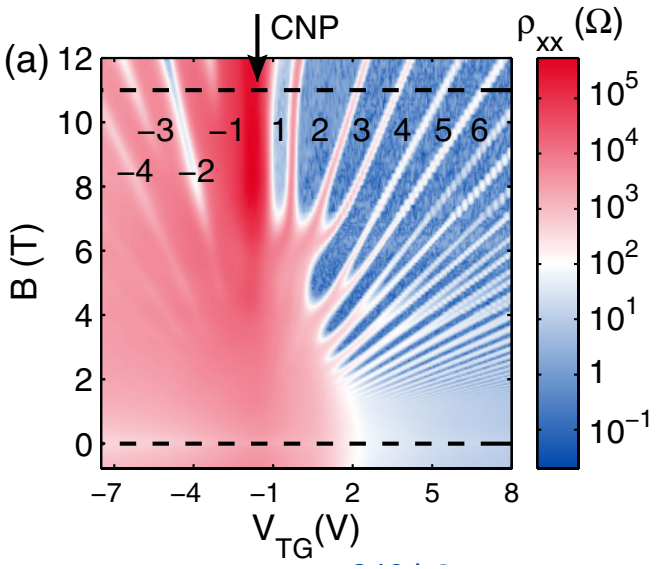

Figure 8.5: Longitudinal resistivity of InAs/GaSb/AlSb QWs, measured at 70 mK for different top gate voltages and magnetic fields from 0 to 12 T. The numbers label the filling factor corresponding to the resp. resistivity minima with positive (negative) numbers indicating electron (hole) transport. The clear visibility of the resistivity minima for electron and especially holes shows the high quality of the samples.

8.7 Characterization of quantum dots for applications in quantum computing

W. Stumpf, W. Wegscheider

Recent experiments on the spin manipulation of carriers confined in a QD have raised their attractivity for solid state quantum information processing. However, any fundamental or applied experiment that utilizes QDs requires a certain tailoring of the QDs' properties such as QD surface density and distribution, size, ensemble emission wavelength and brightness. Indium arsenide (InAs) self-assembly QDs grown by MBE are probably the most appropriate candidate to fulfill these requirements. Material purity and quality are extremely important with respect to applications in quantum computing, such as optical interfaces.

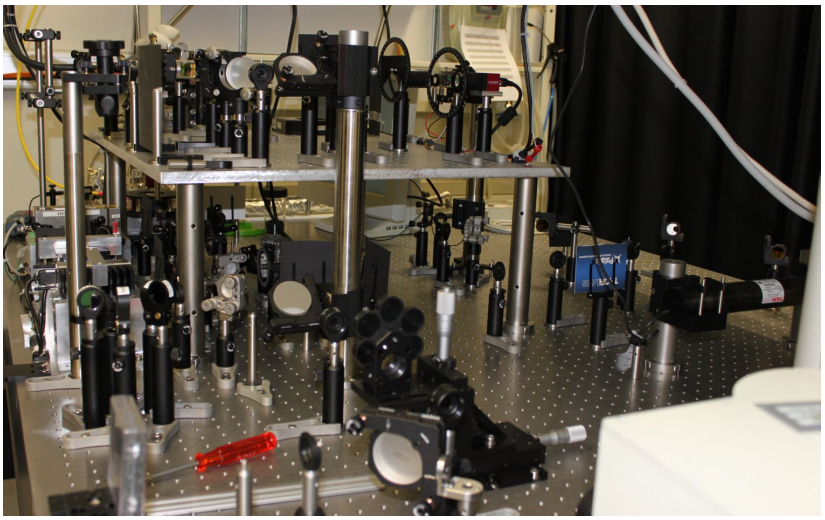

Figure 8.6: Photo of the optical setup

Whereas applications that require high QD densities most characterization techniques offered by the ETH clean room facility FIRST are sufficient, the efficient detection and characterization of single QDs is challenging. Our approach towards gaining this ability is an optical setup which simultaneously realizes high spectral and spatial resolution as

well as a high sensitivity. This also requires very high stability and low drift of mechanical components, which resulted in several major modifications and the need for custom made parts from the ETH workshop. The setup, which has already proven basic operation, is currently at a stage of advanced testing to comply with the severity of stability demands.

8.8 Addressing RI scattering by means of a tunable screening layer

S.Peters, Ch. Reichl, W. Dietsche, W. Wegscheider

It is well known that intentional overdoping leads to an enhancement of the visibility of certain fractional quantum hall effet states, e.g. the $\nu = \frac{5}{2}$ state. In this project we studied a single-sided doped two-dimensional electron system (2DES) grown with intentional parallel conduction in the doping layer. The parallel layer can be separated from the measurement contacts by a so-called pinch-off gate; a top gate allows the tuning of the density in the parallel layer and thus the investigation of its screening effect on the 2DES.

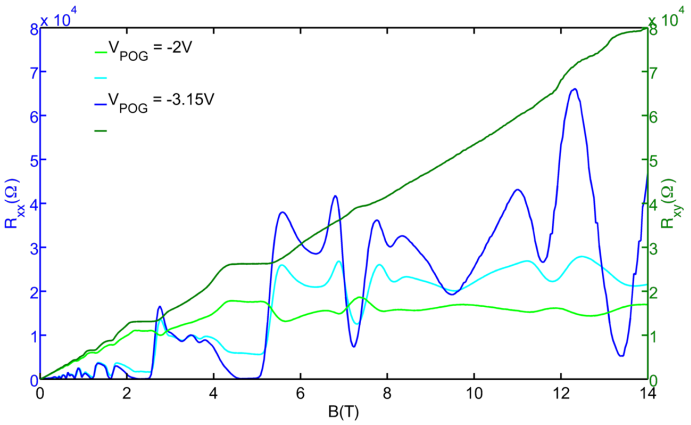

Figure 8.7: Longitudinal and Hall resistance at $V_{POG} = -2\,V$ and $V_{POG} = -3.15\,V$, respectively.

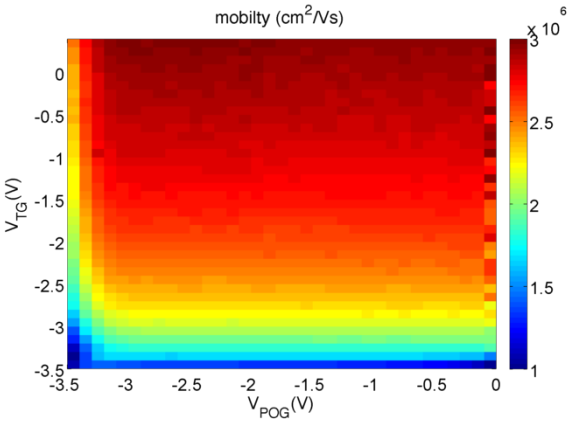

Figure 8.8: Mobility of the 2DES as a function of the density in the parallel layer (expressed in terms of top-gate voltage V_{TG}) and pinch-off voltage.

Figure 8.7 shows the effect of the pinch-off gate; at a pinch-off voltage of $V_{POG} = -2\,V$ the parallel conduction is not suppressed in the transport measurement. However, at $V_{POG} = -3.15\,V$ the parallel conduction layer is separated from the contacts and no longer visible in the longitudinal and Hall resistance. The parallel conduction layer offers screening of the remote ionized impurities but does not negatively affect the transport measurements.

The screening effect of the parallel conduction was investigated by changing its density as a function of top-gate voltage V_{TG}. The observed slight increase in the 2DES mobility with growing top-gate voltage (shown in Fig. 8.8) implies that the screening of the remote ionized impurities is stronger at higher density. The slight increase is in good agreement with the fact that the mobility is dominated by background impurities and not by remote impurities. In future, samples of higher quality in terms of background impurities should enable us to observe more significant impact of reduced RI scattering on transport measurements.

Chapter 9

Neutron scattering and magnetism

(http://www.neutron.ethz.ch/)

Head
Prof. Dr. A. Zheludev

Academic Staff

S. Chillal	Dr. S. Gvasaliya	M. Haelg
Dr. D. Hüvonen	Dr. W. Lorenz	A. Mannig
Dr. K. Povarov	D. Schmidiger	G. Simutis
M. Thede	E. Wulf	

Masters Students

A. Mannig	HS2013
G. Perren	HS2013

Administrative Staff
B. Abt

9.1 P-T Phase Diagram of an Organometallic Quantum Spin Liquid

A. Mannig, M. Thede

As presented in the previous year's report, we have recently discovered a rather unique pressure-induced quantum phase transition in the gapped quantum spin liquid material piperazinium hexachlorodicuprate (PHCC). This result was obtained by muon spin rotation experiments. Long-range magnetic ordering of the initially quantum-disordered PHCC was observed already at a rather low pressure of 10 kBar. This came as a big surprise, considering that previous neutron scattering experiments hinted at the critical pressures of at least 20 kbar [1]. In 2013 we pursued new studies of PHCC under high pressure, aiming to explain this discrepancy, and at establishing the complete $P-T$ phase diagram.

New μ-SR experiments were performed at Paul Scherrer Institut. PHCC powder samples were studied at a total of 15 different applied pressures between ambient pressure and 23 kbar. For each pressure, muon spectra were recorder in zero and weak transversal field at different low temperatures down to 0.27 K (Fig. 9.1, left panel). Having analyzed the data, we were able to identify *three* distinct low-temperature phases. A disordered quantum spin liquid persists in pressures up to $P_c = 4.4$ kbar. Beyond the quantum critical point at P_c, we observed static long range order. Interestingly, for $P_c < P < P1 \sim 14$ kbar, the magnetic structure is an *incommensurate* one. This may be the reason why it was missed by neutron experiments [1], which focused on commensurate spin correlations. Following a second transition at P_1 the structure changes qualitatively, and becomes commensurate with the underlying lattice. Correspondingly, the phase diagram shows a Lifshitz point at (P_1, T_1), $T_1 = 2$ K. The entire experimental phase diagram is visulaized in the right panel of Fig. 9.1 [2].

The result opens new exciting avenues for research. The exact structure of the incommensurate and commensurate phases will now be investigated by neutron scattering. The incommensurate nature of magnetic ordering gives hope that the system will also be ferroelectric, and demonstreate an interplay of magnetic and lattice degrees of freedom at the QCP. Finally, we plan to investigate how the pressure-induced quantum phase transitions in PHCC are affected by disorder, similarly to our previous studies of the field-induced transitions [3].

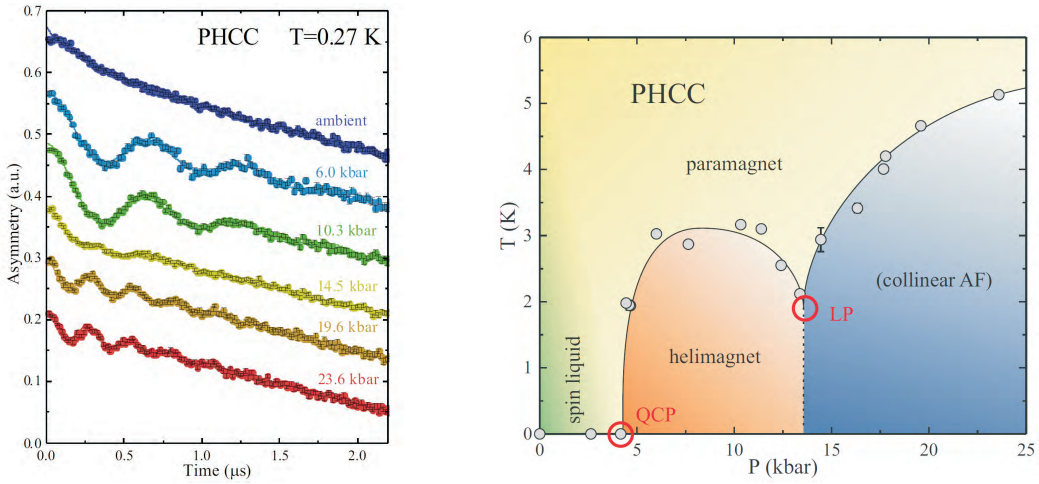

Figure 9.1: Left: μ-SR spectra measured in PHCC for representative pressures at T=0.27 K. right: P-T phase diagram of PHCC with a QCP at 4.4 kbar and a potential Lifshitz point (LP) at 14 kbar.

[1] T. Hong *et al.*, Phys. Rev. B **78**, 224409 (2008).
[2] M. Thede, A. Mannig, M. Mansson,D. Huvonen, R. Khasanov, E. =Morenzoni, and A. Zheludev, Phys. Rev. Lett., in press (2014).
[2] D. Huuvonen *et al.*, Phys. Rev. B 85, 100410 (2012).

9.2 Development of Raman spectroscopy setup and representative results

G. Simutis and S. Gvasaliya

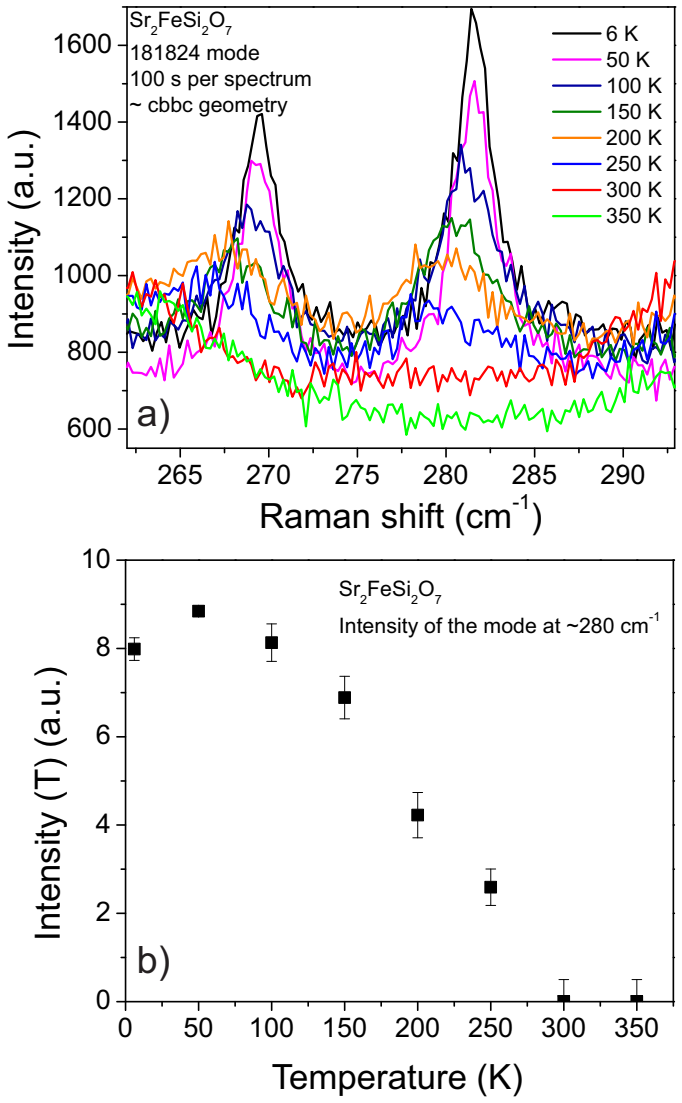

Figure 9.2: a) Raman spectrum of $Sr_2FeSi_2O_7$ at different temperatures across the phase transition. As the temperature is decreased, the symmetry is lowered and a new mode appears at 280 wavenumbers. b) Intensity of the new phonon mode as a function of temperature.

In order to supplement our measurements at large scale facilities and in-house characterization techniques, we have been developing a light spectroscopy setup for studies of excitations and phase transitions. Our Raman spectrometer is based on Princeton Instruments Trivista triple grating setup offering high resolution and good stray light rejection. Over the last year, we have upgraded the setup significantly and obtained several important results.

The biggest change has been the installation of an extra laser in addition to the initial 532 nm wavelength laser. We have chosen the new laser to have wavelength of 660 nm for two reasons. Firstly, the best results are typically obtained for transparent crystals since the signal is collected from a bigger volume of the crystal. However many of the samples that we are studying have electronic bandgap comparable with visible light and hence lead to a high absorption. The new laser with lower photon energy allows us to study more compounds.

The second improvement arising from the new laser is that it allows us to study excitations in the lower energy range. Since the longer wavelength light is dispersed more by the grating, it allows for more effective shielding and rejection of stray light. Additional performance improvement was achieved by updating the optical elements to allow for a better effective luminosity. This enabled us to improve signal to noise ratio and reduce counting times.

By making use of these advances, we performed successful measurements leading to important results. Examples include observation of two magnon scattering in an organic quasi two-dimensional magnet PHCC and quasielastic scattering in a relaxor ferroelectric PMT. In addition, we have studied a structural phase transition in a novel multiferroic $Sr_2FeSi_2O_7$. There have been difficulties to explain the low energy excitation spectrum based on the room temperature symmetry of the crystal. We have performed experiments at different temperatures to study the evolution of the phonon modes. The spectrum changes significantly with lowering of the temperature. The most striking change appears in the spectral range displayed in Figure 1a with a new phonon mode appearing just below the room temperature. The phonon can be approximated as a damped harmonic oscillator to study the intensity of the mode as a function of temperature. The resulting intensity from a fitting procedure to such an approximation is shown in Figure 1b with a clear onset just below room temperature. This is a clear evidence for lowering the symmetry due to a structural phase transition and the spectral calculations are going to be updated to take this into account.

In the upcoming year we will study low energy excitations in different multiferroics, including rare-earth manganites and orthochromates. We expect to observe magnetic modes triggered by the onset of electrical polarization.

9.3 Spin Chains in the Tomonaga Luttinger Liquid Phase: Universality and Scaling

M. Hälg, D. Hüvonen, W. EA. Lorenz

The behavior of one dimensional gapless systems is qualitatively different from the Fermi liquid one and belongs to the universality class of Tomonaga Luttinger liquids (TLL) [1]. All low energy properties of *any* such system are completely characterized by just two constants, the Luttinger parameter K and the Fermi velocity u. TLL theory is not only able to predict the dynamic structure factor of spin chains [2,3] but it can also treat small interchain interactions. Particularly, it presents a model to relate magnetic field and the critical temperature where the system undergoes a phase transition to a 3D-ordered state [3].

One striking result of universality in the TLL phase is that the temperature scaled q-integrated dynamic structure factor $T^{\alpha_K} S(\omega)$ is a universal function of ω/T and K without any sample dependent parameters. In order to recover the universal scaling law, neutron experiments have been performed on two materials, namely NTENP and CuDCl. NTENP is an $S = 1$ chain with anisotropy which is gapless at the quantum critical point (QCP) of a quantum phase transition driven by magnetic field [4]. Precisely at the QCP the system behaves as a TLL [2]. Preliminary data from studies on NTENP on IN14 at ILL and V2 at HZB confirm the scaling hypothesis (fig. 9.3a).

A remarkable property of $S = 1/2$ chains like CuDCl [5] is the possibility to realize a tunable TLL by applying magnetic field. In field the dynamic structure factor retains universality *and* the Luttinger parameter can be tuned continuously from $K = 0.5$ in zero field to $K = 1$ at saturation [3]. The confirmation of the scaling behavior of CuDCl in magnetic field has been prevented so far by the poor energy resolution of the used instruments. Nevertheless, very promising data has been obtained from a recent experiment on OSIRIS at ISIS (fig. 9.3b).

Interchain coupling leads to magnetic order at low temperatures. If the interchain coupling J' is small compared to the intrachain coupling J it can be treated in the mean field approximation. TLL theory can relate the 3D-ordering temperature to the external magnetic field. This relation is universal for all spin $1/2$ chains and only depends on the ratio of inter- and intrachain coupling J'/J. As a test sample the $S = 1/2$ chain KCSBr was chosen which shows a phase transition at 98 mK in zero magnetic field. Its phase diagram was obtained by specific heat measurements and found to be consistent with TLL theory up to 14 T which was the upper limit of accessible magnetic field (fig. 9.3c). Future work will include measurements at high magnetic field facilities in order to obtain the full phase diagram of KCSBr.

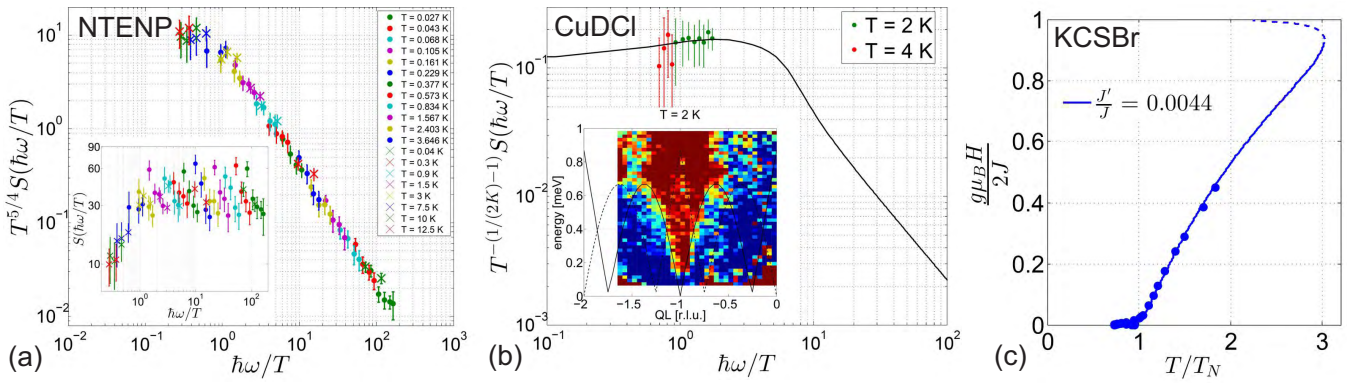

Figure 9.3: (a) Scaled and unscaled (inset) q-integrated structure factor of NTENP measured on IN14/ILL and V2/HZB. (b) Scaling plot of CuDCl at 7.5 T measured on OSIRIS/ISIS (inset: spectrum at 2 K). (c) Phase diagram of KCSBr.

[1] F. D. M. Haldane, PRL **45**, 1358 (1980)
[2] S. Sachdev, *Quantum Phase Transitions* (Cambridge University Press, 1999)
[3] T. Giamarchi, *Quantum Physics in One Dimension* (Oxford University Press, 2003)
[4] M. Hagiwara *et. al.*, PRL **94**, 177202 (2005)
[5] T. Hong, Phys. Rev. B **80**, 132404 (2009)

9.4 Long range magnetic order in the disordered spin chain $BaCu_2(Si_{1-x}Ge_x)_2O_7$

M. Thede

Antiferromagnetic (AF) spin-1/2 Heisenberg chains remain disordered even at zero temperature due to quantum fluctuations and are prototypical quantum spin systems [1]. New exotic quantum phases are induced by bond disorder in such systems [2, 3]. In any real material arbitrary weak interactions between chains will result in 3D long range order at low temperatures [4]. In this study we investigate the effect of intra-chain bond disorder on such 3D ordering in weakly coupled spin chains.

The subject of our investigation are the well-known spin chain compouds $BaCu_2(Si_{1-x}Ge_x)_2O_7$. Random exchange constants in the Cu^{2+} chains are realized by a variation of the Cu-O-Cu bond angle, that in turn are affected by Ge substitution on the Si site. The average in-chain exchange coupling constant varies linear between J=24 meV for the silicate (x=0) and J=50 meV for germanate (x=1). In contrast, the effect of randomness on the ordering temperature is non linear [4]. It decreases for both end materials.

We performed zero field MuSR experiments on seven different concentrations to study the effect of disorder on the magnetic ordered state. Both pure end members show two well defined cosine oscillations (Fig. 9.4) with very different frequencies. These are heavily damped in the presence of 5 % disorder (x=0.05, x=0.95). Even more randomness leads to change from oscillating to a gaussian-like functional form of the spectra. Its decay decreases as a function of concentration and the smallest value is reached for x=0.5 .

The field distribution can be calculated by a Fourier transformation of the μSR time spectra (Fig 9.4). In the pure material two peaks, corresponding to two different moun sites, are observed. These peaks shift to lower fields and merge as disorder is increased. The mean field, which is proportional to the magnetic moment, shifts clearly from B_{mean}=175 G (x=0) to B_{mean}=7 G (x=0.5). The suppression of the ordered moment is more than twice as strong as of the ordering temperature. The overall conclusion is that bond randomness locally modulates the quantum fluctuations in the spin chains and thereby produce an *inhomogeneously* ordered state.

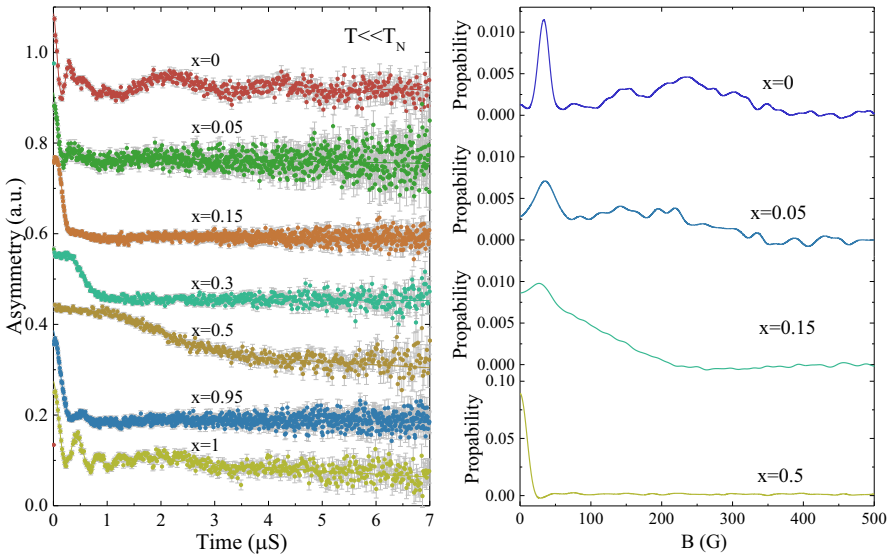

Figure 9.4: left: μSR time spectra for 7 different concentrations well below T_N right: Internal field distribution of 4 different concentrations

[1] T. Giamarchi, Quantum Physics in One Dimension (2004).
[2] C. Dasgupta et al., Phys. Rev. B 22, 1305 (1980).
[3] C. Doty et al., Phys. Rev. B 45, 2167 (1992).
[4] H.J. Schulz, Phys. Rev. Lett. 84 3434, (2000).

9.5 Magnetic short and long range order in a disordered perovskite

S. Chillal, S. Gvasaliya

Last year, an important result obtained in our laboratory was the discovery of microscopic co-existence of antiferromagnetic and spin glass order (AFSG) in the cubic perovskite material $PbFe_{1/2}Nb_{1/2}O_3$ (PFN) [1]. In order to better understand the origin of this peculiar partially disordered state, this year we focused on a similar material with a different non-magnetic substitute on the magnetic Fe^{3+} site, namely $PbFe_{1/2}Ta_{1/2}O_3$ (PFT) [2,3]. We employed bulk measurements, neutron scattering and Mössbauer spectroscopy to establish the magnetic phase diagram of this compound, that to date was poorly understood.

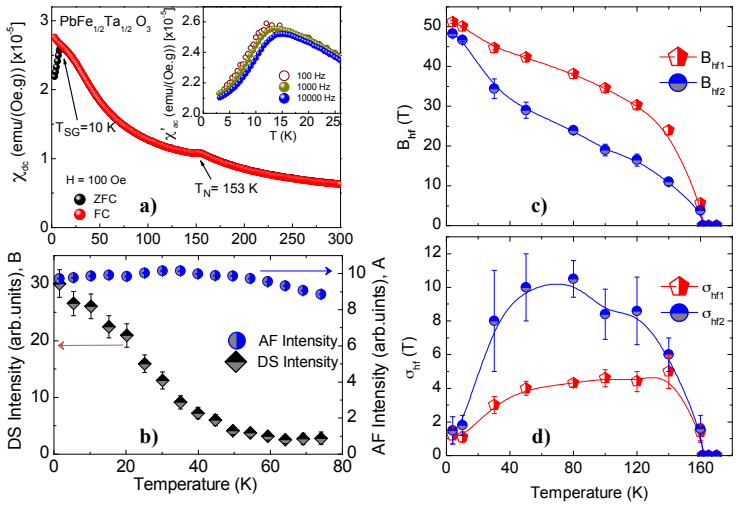

Figure 9.5: a) DC susceptibility of PFT measured in ZFC and FC protocols in a field of 100 Oe. Inset shows the ac susceptibility measured with different frequencies. (b) Temperature dependence of AF Bragg and diffuse scattering intensities in PFT single crystal measured at the wavevector $\mathbf{Q}_{AF} = (\frac{1}{2}, \frac{1}{2}, \frac{1}{2})$. (c) Hyperfine fields at Fe^{3+} ions and d) widths of their distribution probed by Mössbauer spectroscopy. The red and blue lines are guide to the eye.

The measured DC magnetic susceptibility of PFT is shown in Fig. 9.5(a) Two anomalies anomalies are apparent. One inddicates long-range AF ordering at $T_N \sim 153$ K, while the other is related to a spin freezing and formation os a SG state at $T_{SG} \sim 10$ K. The SG nature of the latter transition is confirmed by the frequency dependence of rounded peak in ac-susceptibility (inset of Fig. 9.5(a)). As the SG transition is approached, the emerging short range spin correlations give rise to diffuse neutron scattering (DS)around the AF Bragg peak position. It's temperature dependence is shown in Fig. 9.5(b). We see that the short-range correlations appear already at T$\sim$50 K, well above the SG transition. Notably, in the same temperature range the AF intensity remains virtually unchanged.

The coexistence of AF and SG order at the microscopic level is confirmed in Mössbauer spectroscopy experiments. In paramagnetic state, the spectrum is a doublet with chemical shift corresponding to Fe^{3+} and a non-zero quadrupole splitting. In AF phase, a sextet appears due to the magnetic order in the sample while quadrupole splitting becomes zero. The observed sextet is consistent with two contributions to the hyperfine field distribution at Fe^{3+}, as shown in Fig. 9.5(c). Both contributions, B_{hf1} and B_{hf2} increase smoothly upon cooling below T_N. The increase accelerates below $\sim$50 K. At base temperature, both fields merge, and a full moment is recovered. Notably, the B_{hf} widths σ_{hf1}, σ_{hf2} (Fig. 9.5(d)) demonstrates a plateau between $\sim$120 K and $\sim$50 K. At lower temperatures the widths decreases rapidly, and ultimately merge to zero at base temperature. This behavior suggests that the dynamic effects dominate the broadening of the Mössbauer lines of PFT. The nearly zero value of σ_{hf} obtained at 4 K implies a vanishing contribution of static fluctuations to B_{hf}.

The features of the Mössbauer spectra below T_{SG} unambiguously confirm a homogeneous environment for all Fe^{3+} ions in the system, and a uniformity of the *magnitude* of the ordered moments. Since neutron scattering demonstrated an *increase* of short-range correlations in this regime, we conclude that the disorder at low temperature is purely orientational. This in turn, supports the same scenario for the AFSG phase, that we previously suggested for PFN. Returning to a direct comparison with our previous results on PFN, the magnetic phase diagram of $PbFe_{1/2}B_{1/2}O_3$ materials appear to be largely independent of which non-magnetic ion is substituted at the B-site.

[1] S. Chillal, *et al.*, Phys. Rev. B **87**, 220403 (2013).
[2] N. Lampis *et al.*, J. Phys: Cond. Matt. **11**, 3489(1999).
[3] V. Bonny, Solid State Comm **102** 347(1997).

9.6 Specific heat study of crossover exponent in clean and bond-disordered IPA-$CuCl_3$

G. Perren, W. Lorenz

The effects of disorder on the physics of classical and quantum systems can be very diverse [1]. Among different real materials, organometallic magnetic insulators are ideally suited to study disorder in a well controlled way and in close connection to theory. In these materials, disorder is usually introduced by chemical substitution which randomly alters the superexchange pathways [2]. A topic of great current interest is concerned with the instability of spin liquid phases with respect to external magnetic fields. Such field-induced (*quantum*) phase transitions are best described in terms of Bose-Einstein condensation (BEC). Fisher *et. al* [3] proposed the existence of a novel and exotic short-range ordered quantum phase, called the Bose Glass (BG) which should be observable in a disordered system of interacting bosons. As pointed out in [3], the critical behaviour of the BG-BEC transition is supposed to be much different compared to ordinary BEC.

We continued our study of the BEC and the BG-BEC in the well-known magnetic insulator $(CH_3)_2CHNH_3CuCl_3$ (clean IPA), a spin liquid for $H < H_c$ [4], [5] and in its 5% bond-disordered version IPA-$CuCl_{0.95}Br_{0.05}$ by calorimetric measurements. The magnetic properties of IPA stem from interacting copper ions ($S = 1/2$) that are only bridged by chlorine ions in clean IPA or randomly bridged by the more voluminous bromine ions in disordered IPA, see Fig. 1 a). We traced out the low-temperature phase boundary for both materials within the T-H plane in which all measurements were performed on our PPMS by Quantum Design, see figure Fig. 1 b) and c). Clearly, the phase boundaries do not coincide and the critical crossover exponent ϕ which describes the behaviour "near" the quantum critical point $T_c(H) \sim (H - H_c)^{\phi}$ is different. Very interesting, $\phi = 0.70 \pm 0.02$ for clean IPA which is pretty close to the theoretical predicted crossover exponent for BEC $\phi = 2/3$ [3]. Furthermore, the crossover exponent for disordered IPA amounts to $\phi = 0.93 \pm 0.04$ in good agreement with a recent numerical result where $\phi \sim 1$ [6].

In summary, previous studies on clean IPA ([4], [5]) together with the new calorimetric measurements strongly suggest the existence of a BEC phase. Referring to disordered IPA, the measured phase boundary does point to a BG phase. We are therefore very confident that future neutron diffraction experiments on disordered IPA will underpin the assumption that we found a real material which exhibits a BG phase.

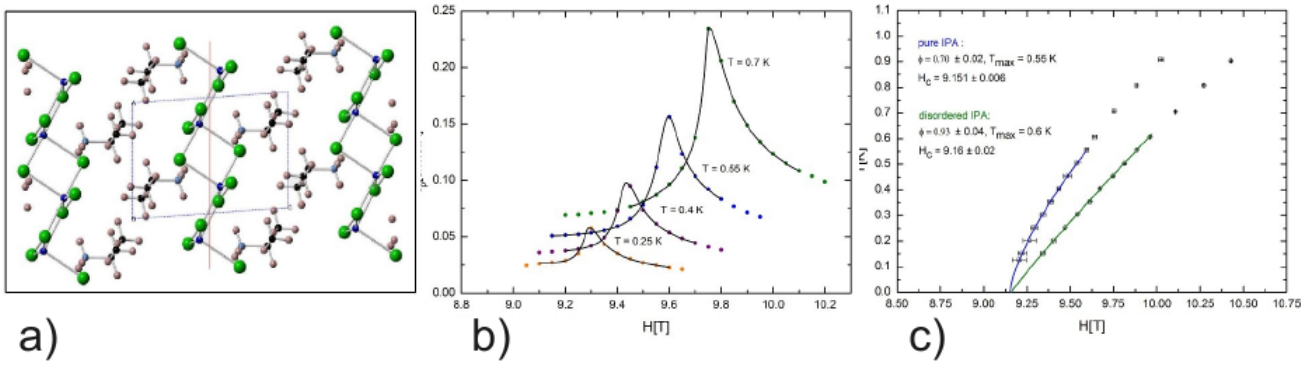

Figure 9.6: a) Crystal structure of IPA directed along the crystallographic *b*-axis. Colour code: Cu^{2+} blue, Cl^- or Br^- green, C black, N cyan, H brown. b) Representative specific heat measurements of clean IPA (molar heat capacity versus field) at different temperatures. The lines are fits to an empirical fit function, where the maximum is identified as the critical field. c) Measured phase diagram of clean and disordered IPA. The blue and green solid line represent power law fits to $(T_c(H) \sim (H - H_c)^{\phi})$. T_{max} determines the fit range from above.

[1] A B Harris J. Phys. C: Solid State Physics, **7**, 1671 (1974)
[2] A. Zheludev and T. Roscilde, arXiv:1305.1194v1
[3] Fisher et al. Phys. Rev. B, **40**, 546 (1989)
[4] H. Manaka et al. JPSJ, **67**, 3913 (1998)
[5] T. Masuda, A. Zheludev Phys. Rev. Lett., **96**, 047210 (2006)
[6] R. Yu et al. Europhys. Lett., **89**, 10009 (2010)

9.7 Properties of a quantum phase transition in presence and absence of disorder

E. Wulf, D. Hüvonen

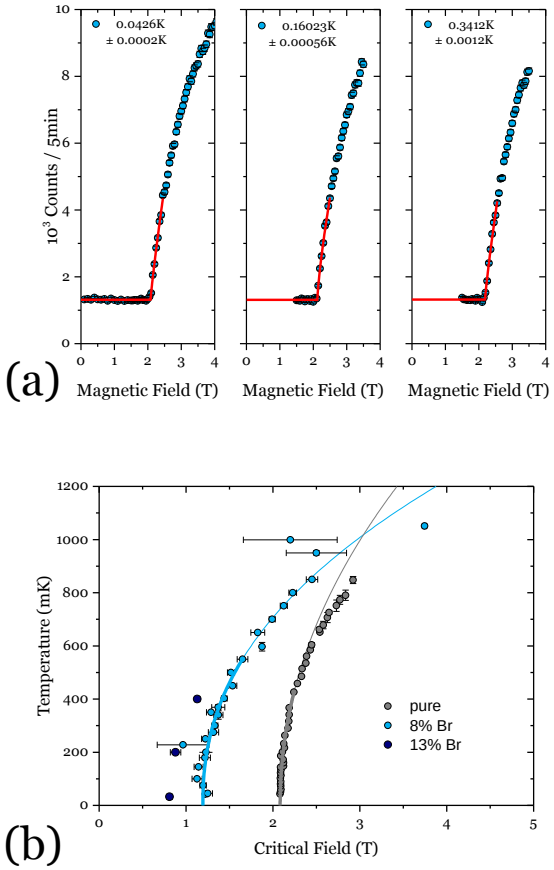

Figure 9.7: (a) Scattered intensity measured around the magnetic $(\frac{1}{2}, \frac{1}{2}, \frac{1}{2})$ reflection on DTN. The red lines illustrate the range were a power law was fitted to the data. (b) Phase diagram derived for the pure reference DTN (gray), 8% DTNX (light blue) and 13% DTNX (dark blue).

Disorder can have a profound effect on quantum spin liquids. For example random potentials introduced by chemical substitution can lead to the appearance of new phases such as the Bose glass phase due to localization of bosons [1]. The Bose glass is a state appearing at zero temperature between the ground state and the Bose-Einstein condensate (BEC) phase. It is characterized by the absence of a common wave function, therefore the absence of long range correlations and local gapless states. In presence of disorder the properties of the BEC quantum critical point change, but how exactly is still hotly debated [2]. To probe the properties of such Bose glass to BEC transitions a good realization of a clean BEC in a quantum magnet is required.

A promising candidate for the realization of a "clean" BEC realization is $NiCl_2 \cdot 4SC(NH_2)_2$, DTN for short [3]. DTN condenses in the body centered tetragonal structure $I4$ (No. 79). The spin $S = 1$ is carried by Ni^{2+} ions and superexchange via the halide ions is the exchange mechanism. At $H_c \approx 2.1$T DTN undergoes a field induced phase transition to an antiferromagnetically ordered state. By substituting nonmagnetic chlorine by nonmagnetic bromine ions random bond disorder is introduced to DTNX, due to modifications of the superexchange paths. A recent publication reported a Bose glass state in DTNX [4]. The phase transition was probed by measurements of AC susceptibility and compared to numerical studies [4] supporting the Bose glass interpretation of DTNX. The simulations predict an order parameter critical exponent of $\beta = 0.95(1)$ [4] and a crossover exponent $\phi = 1.1(1)$ [4] for DTNX with $x = 8\%$.

We probed the field dependence of the antiferromagnetic order parameter by neutron diffraction on bond disordered DTNX samples with two different bromine substitution ratios and the pure reference DTN. Figure 9.7a shows the intensity ($I \propto m^2$) measured around a magnetic Bragg reflection on DTN at three different temperatures. Panel b of figure 9.7 shows the phase boundary determined for the three samples. The fat solid line illustrates the fitting range used to estimate ϕ. For the $x = 8\%$ sample we derived $\beta = 0.50(4)$ at 42mK in a 1T range above H_c and $\phi = 0.44(8)$ for the interval [42mK, 550mK]. On the $x = 13\%$ sample the order parameter critical exponent $\beta = 0.58(4)$ was derived at 32mK [5]. These measurements cast doubt on the predictions from the numerical simulations [4]. From a reference measurement on the disorder free DTN, $\beta = 0.44(2)$ (43mK) and $\phi = 0.49(5)$ ([0mK, 260mK]) were estimated. These values are unexpected as theory predicts $\beta = \frac{1}{2}$ and $\phi = \frac{2}{3}$ for a 3D BEC transition. Reasons for the discrepancy will be clarified in upcoming magnetocaloric and magnetic measurements.

[1] M. P. A. Fisher et al. PRB **40**, pp. 546–570 (1989)
[2] A. Zheludev, T. Roscilde C. R. Phys. **8**, pp. 740–756 (2013)
[3] V. S. Zapf, D. Zocco et al. PRL **96**, pp. 77204 (2006)
[4] R. Yu *et al.*, Nature **489**, 379 (2012); R. Yu *et al.*, PRB **86**, 134421 (2012)
[5] E. Wulf, D. Hüvonen et al. PRB **88**, pp. 174418 (2013)

9.8 Development of macroscopic measurement techniques

K. Yu. Povarov

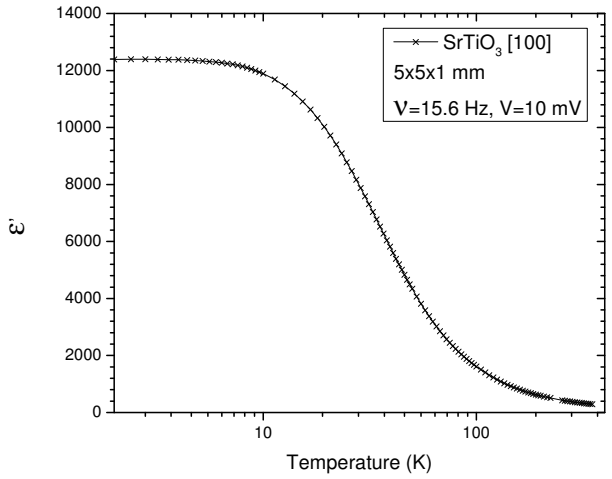

Figure 9.8: Real part of the dielectric permittivity of a single crystal $SrTiO_3$ plate, measured as described in the text.

Our plans for the nearest future are to develop a number of techniques based on standard Quantum Design Physical Properties Measurement System (PPMS), including the use and customization of the Quantum Design Dilution Refrigerator insert. These techniques are dielectric spectroscopy, measurement of magnetoelectric response and measurements of AC susceptibility below 1 K. At the moment we already have a completely functional prototype of PPMS dielectric spectrometer, with a lock-in amplifier operating in an ammeter mode to measure the displacement current. This allows us to capture both real and imaginary parts of dielectric response; we also have an ability to measure higher harmonics (in [1] it is shown, how the higher harmonics are related to the non-linearity of the electrical response of the material investigated). We also have an automated, LabView-based software to control the experiment (external instrumentation and PPMS as well). At Figure 9.8 we present a preliminary result of dielectric permittivity measurement on a single, 1 mm thick, $SrTiO_3$ crystal. We also expect this setup to be easily used together with the dilution refrigerator insert.

Another PPMS-based technique is the magnetoelectric response measurement with the standard PPMS AC magnetometry setup. The idea is similar to described in [2]. Driving voltage of the excitation coil is redirected to the amplifier and applied to the metal plates on sample surface. In this configuration the response of the pick-up coils will be due to the electrically induced magnetic moment of the sample. This project is still at the early stage of the development.

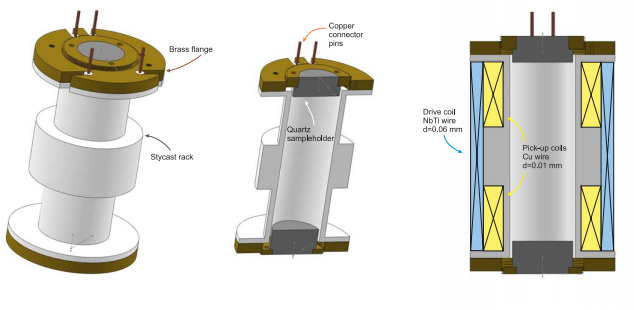

Figure 9.9: Sketches of the low-temperature AC magnetometer. Left to right: assembly without coils, cut view of assembly without coils, cut view of assembly with coils.

The most involved project is the construction of ultralow-temperature device for AC susceptibility measurement. This AC magnetometer is to be used as a custom probe together with the PPMS dilution refrigerator insert, where the total space available is 35 mm in height and 22 mm in diameter. The basic principles of the design follow one described in [3]: magnetometer is composed of a pair of pick-up coils wound in the second-order gradiometer configuration, and an external superconducting drive coil. Thermal contact of a sample with the dilution refrigerator sample stage is achieved with the help of the quartz sampleholder. A few sketches of the future instrument are shown in Figure 9.9. This magnetometer is currently under construction now. We expect it to operate down to 50-100 mK and in fields up to 14 T.

[1] S. Miga, J. Dec and W. Kleemann; Rev. Sci. Instrum. **78**, 033902 (2007).
[2] P. Borisov, A. Hochstrat, V. V. Shvartsman and W. Kleemann; Rev. Sci. Instrum. **78**, 106105 (2007).
[3] L. Yin, J. S. Xia, N. S. Sullivan, V. S. Zapf, A. Paduan-Filho; J. Low Temp. Phys. **158**, 710 (2010).

9.9 Dzyaloshinskii-Moriya induced frustration of inter-chain interactions

W. EA. Lorenz, M. Haelg, K. Povarov

We have studied the magnetic phase diagrams of the isostructural compounds $K_2CuSO_4Cl_2$ and $K_2CuSO_4Br_2$ by means of specific heat measurements. The crystal structure of the chlorine compound was reported previously [1], but the magnetic properties of these inorganic Cu^{2+} salts have hitherto not been investigated. From the magnetism point of view the materials have a fairly interesting structure. It comprises $S = 1/2$ spin-chains along the a-axis, with the (a-c)-plane being a mirror plane and a consequent absence of staggered g-tensor. The intra-chain exchange has an anti-symmetric component with Dzyaloshinskii-Moriya (DM) vector parallel to the b-axis. Our ESR data are in line with the structural analysis, which suggests the existence of anti-symmetric exchange as well as maximal g-factor parallel to the b-axis. From the structure one can also deduce a peculiar pattern of frustration of inter-chain interactions as follows: While the DM vector is uniform for intra-chain exchange, thus supporting incommensurate in-chain correlations, the DM vector in neighboring chains points in opposite direction, thus yielding again incommensurate correlations but with opposing helicity. Assuming DM interactions to dominate the inter-chain exchange, inter-chain correlations will be frustrated with those along the chain.

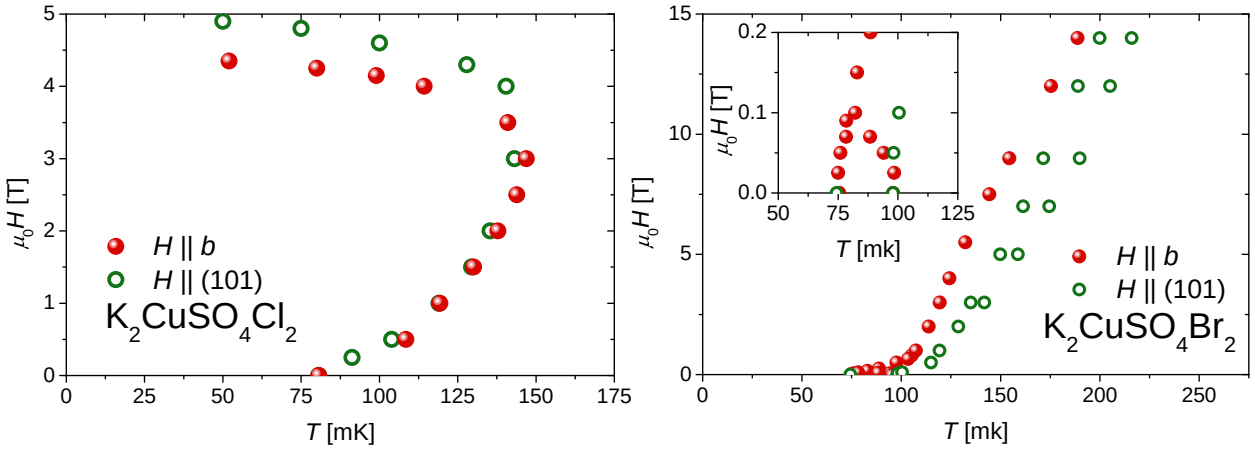

Figure 9.10: Magnetic phase diagrams of $K_2CuSO_4Cl_2$ ((left) and $K_2CuSO_4Br_2$ (right). Data are shown for magnetic field applied along the DM vector (•) and perpendicular (○). Note the additional phase appearing at finite field $||(101)$ in the Br compound. Details of the $K_2CuSO_4Br_2$ phase diagram at low field are shown in the inset.

From analysis of susceptibility, specific heat and inelastic neutron scattering data we find significantly different intra-chain exchange, $J_{\mathrm{Cl}} = 3.2$ K and $J_{\mathrm{Br}} = 20.4$ K for the chlorine and bromine compound, respectively. Magnetic order however sets in at about 100 mK in both compounds. From the ordering temperatures and the intra-chain exchange one can estimate very similar inter-chain couplings $J' \approx 90$ mK [2]. For the Br compound we estimate anisotropic exchange $D \geq 0.3$ K from our ESR data; well larger than J', which should yield the frustration pattern discussed above. Assuming a similar J/D ratio, frustration should be less relevant in the chlorine compound. Indeed, the magnetic phase diagrams (see fig. 9.10) of both compounds differ significantly, whereat the bromine material shows a number of additional phases not present in the chlorine material. Most notably, there is an additional phase at finite temperature quickly suppressed by magnetic field, in particular if applied perpendicular the the DM vector. We have not observed a spin-flop transition, but instead an additional phase stable at finite temperatures and field only. We suggest frustration to be the underlying mechanism to stabilize these unconventional phases.

[1] C. Giacovazzo *et al.*, Zeitschr. f. Kristallographie, **144**, 226 (1976).
[2] H. J. Schulz, Phys. Rev. Lett. **77**, 2790-2793 (1996).

Chapter 10

Spin Physics and Imaging

(www.spin.ethz.ch/)

Head
Prof. Dr. C. Degen

Academic Staff

J. Boss	K. Chang	Dr. A. Dussaux
Dr. A. Eichler	U. Grob	M. Loretz
B. Moores	Dr. P. Navaretti	T. Rosskopf
Dr. R. Schirhagl	Dr. H. Takahashi	Y. Tao

Master Students
J. Boss (FS2013)

Technical Staff
C. Keck

Academic Guests
Dr. Tina Mueller, Mc Gill Univ. (2.12.2013 - 20.12.2013)
Stefan Bogdanovic, TU Delft (2.12.2013 - 6.12.2013)

10.1 Nanoscale nuclear magnetic resonance with a shallow nitrogen-vacancy sensor

M. Loretz, C.L. Degen

Diamond magnetometry with nitrogen vacancy (NV) centers may provide a route for nanoscale magnetic resonance imaging and spectroscopy with single nuclear spin resolution. The atomic size of the sensor and its high magnetic field sensitivity allow overcoming the two main limitations of conventional, induction-based magnetic resonance: spatial resolution and sensitivity.
Our nanoscale magnetic resonance experiments are enabled by improvements in engineering of NV center with very small sample-to-sensor distance, which is the key factor determining sensitivity. We have used shallow ion implantation followed by a controlled, nanometer-by-nanometer removal of diamond material by oxidative etching in air to produce NV centers at 2-6 nm from the surface. The depth of NV centers was calibrated by performing ^{1}H NMR of an organic calibration sample and relating signal strength to surface-to-sensor distance. The ^{1}H NMR signals were measured using modified Carr-Purcell decoupling sequences at a bias field of 200 mT. The close proximity of NV centers to the surface yielded strong NMR signals of up to 3.5 μT-rms, corresponding to 330 statistically polarized or 10 fully polarized protons in a (1.8 nm)^3 detection volume. Since the measured NMR signals are strong, the number of spins detected in our measurements is limited by the spatial resolution of the NV sensor, and not by detection sensitivity. The present experiment may be extended to single nuclear spin detection, such as by diluting the 1H density or by the application of a strong imaging gradient.

Literature Reference: M. Loretz, S. Pezzagna, J. Meijer and C. L. Degen, 'Nanoscale nuclear magnetic resonance with a 1.9-nm-deep nitrogen-vacancy sensor', Appl. Phys. Lett. 104, 033102 (2014).

10.2 Negatively charged nitrogen-vacancy centers in a 5-nm-thin ^{12}C diamond film

K. Ohashi, T. Rosskopf, H. Watanabe, M. Loretz, Y. Tao, R. Hauert, S. Tomizawa, T. Ishikawa, J. Ishi-Hayase, S. Shikata, C. L. Degen, and K. M. Itoh

Since the experimental demonstrations of single electron- and nuclear-spin manipulation and readout, the negatively charged nitrogen-vacancy (NV^-) center in diamond has been considered one of the most promising solid-state qubits toward quantum information processing and magnetometry. Its spin properties are enhanced when placed in isotopically enriched ^{12}C diamond leading to very long electron spin coherence times ($\sim$ 2 ms) at room temperature. We report successful introduction of NV - centers in a 5 nm thin, isotopically enriched (^{12}C = 99.99 $\%$) diamond layer by CVD. The present method allows for the formation of NV^- in such a thin layer even when the surface is terminated by hydrogen atoms. NV^- centers are found to have spin coherence times of between $T_2 \sim 10 - 100\ \mu s$ at room temperature. We demonstrate the suitability for nano-scale NMR by measuring the fluctuating field from $\sim 10^4$ proton nuclei placed on top of the 5 nm diamond film. Formation of stable NV^- centers within a distance of < 5 nm from the surface constitutes an important step towards single nuclear spin detection, to provide sufficient dipolar coupling between the NV^- electron spin and a target nuclear spin. Such small distances are also required to achieve a spatial resolution approaching the atomic level.

Literature Reference: K. Ohashi, T. Rosskopf, H. Watanabe, M. Loretz, Y. Tao, R. Hauert, S. Tomizawa, T. Ishikawa, J. Ishi-Hayase, S. Shikata, C. L. Degen, and K. M. Itoh, "Negatively charged nitrogen-vacancy centers in a 5-nm-thin ^{12}C diamond film", Nano Letters 13, 4733 (2013)

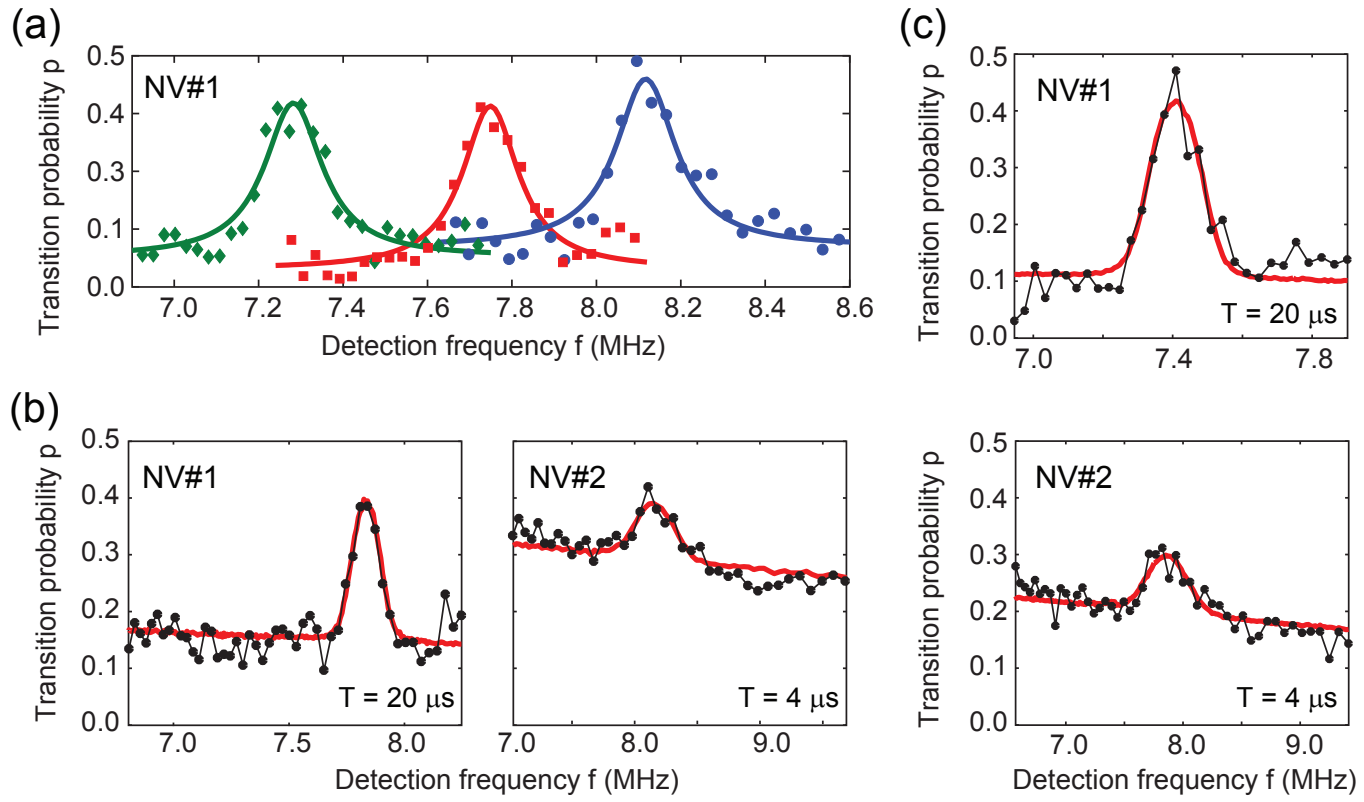

Figure 10.1: (a) Spectra redorded by NV1 at different bias fields B_0 confirm that signals originate from ^1H nuclear spins. (b) ^1H NMR of the organic calibration sample. Dots show experimental data and red curves are numerical simulations to calculate the signal strength. Total evolution time indicated by T. (c) ^1H NMR of molecular adsorbates naturally present on the diamond surface. Spectras were taken at bias fields between $180 - 195$ mT.

10.3 On the surface paramagnetism of diamond

T. Rosskopf, A. Dussaux, K. Ohashi, M. Loretz, R. Schirhagl, H. Watanabe, S. Shikata, K. M. Itoh, and C. L. Degen

With the recent developments in nano-scale magnetic sensing using nitrogen vacancy centers (NV- Centers) in diamond, there is growing evidence that surface-related magnetic noise is one of the main constraints limiting the sensitivity of diamond-based sensors.
By relating the longitudinal relaxation time T_1 and the rotating frame relaxation time $T_{1\rho}$ of shallow NV-Centers to the magnetic noise power spectral density, we were able to derive information about surface spin density and a characteristic correlation time of the surface related magnetic noise. Our results yield a surface spin density of $0.01-0.1\mu_B/\text{nm}^2$ and a correlation time of 0.3 ± 0.1ns. No major variations are found for different surface terminations and samples. This suggests that the surfaces states are related to the diamond‘s top carbon layer rather than terminating surface atoms or adsorbate molecules.
In the light of these findings, several illuminating experiments could be conceived to more precisely pinpoint the underlying atomistic mechanism responsible for surface magnetic states. Altogether, a precise understanding of diamond surface magnetic states will be crucial for further improving the sensitivity and resolution of diamond magnetic sensor heads and sensor arrays.

Literature Reference: T. Rosskopf, A. Dussaux, K. Ohashi, M. Loretz, R. Schirhagl, H. Watanabe, S. Shikata, K. M. Itoh, and C. L. Degen, ”On the surface paramagnetism of diamond”, arXiv:1311.2036 (2013)

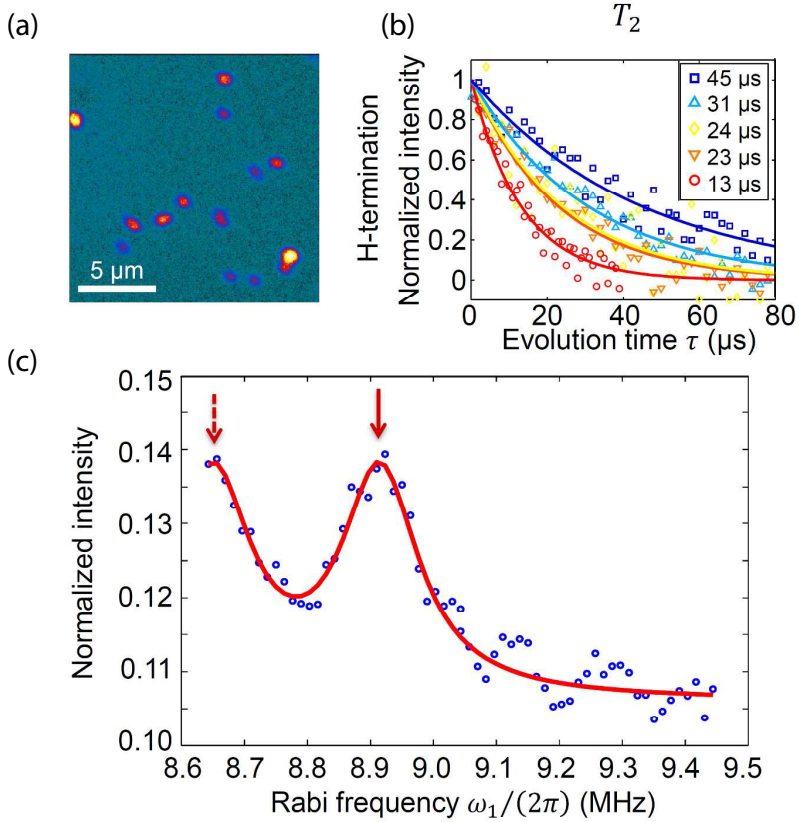

Figure 10.2: (a) Confocal photoluminescence (PL) scan image over the surface (XY) area of $16\times16\ \mu m^2 2$, showing single nitrogen-vacancy-centers. (b) Example dataset (Hydrogen termination) of room temperature spin echo and spin relaxation measurements of several NV-centers. (c) Example of detection of a small ensemble of proton spins on top of the present 5 nm diamond film, showing the suitability for nuclear spin sensing. The main proton peak at 8.915 MHz is indicated by a red arrow. Blue dots are experimental data, red curve is a calculation using an rms-magnetic field of 780 nT and a linewidth of 140 kHz.

10.4 Facile Fabrication of Single-Crystal-Diamond Nanostructures with Ultrahigh Aspect Ratio

Y. Tao, C.L. Degen

Compatibility with batch fabrication is a technological challenge facing many promising materials for NEMS applications,including carbon nanotubes, graphene nanoribbons,nanowires of various material compositions, and single-crystal diamond. Often, multiple reasons prevent a promising material system from “going batch”, such as low yield during material synthesis, difficulty in controlling geometry, placement, and orientation during growth and processing, as well as poor consistency in the quality of finished devices. Single-crystal diamond is one of such promising materials with unparalleled material properties, which have not yet been fully unlocked due to difficulties associated with its growth and processing.

Here, a robust and facile approach for making single-crystal-diamond MEMS and NEMS devices is presented. The approach relies entirely on commercial diamond material and standard cleanroom processes. As an example, batch fabrication of cantilever beams of thickness down to 45 nm and aspect ratios exceeding 2000:1 is demonstrated.

Literature Reference: Y. Tao and C. L. Degen, “Facile Fabrication of Single-Crystal-Diamond Nanostructures with Ultrahigh Aspect Ratio”, Advanced Materials 25, 3962 (2013).

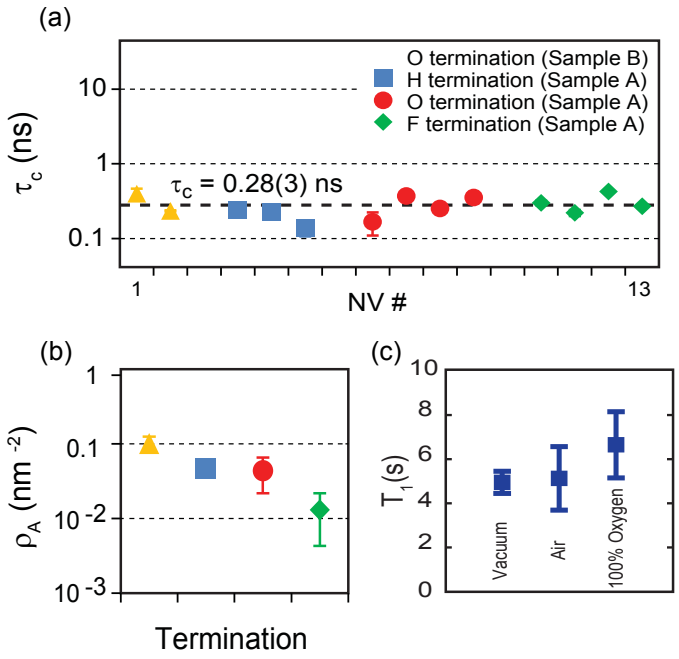

Figure 10.3: Spin relaxation time measurements of 13 shallow NV centers for different samples, surface terminations and atmospheres. (a) Autocorrelation time t_c of surface fluctuations for the same NV centers, organized by sample and surface termination. (b) Density of surface impurities ρ_A for samples and surface terminations. (e) T_1 Relaxation time under vacuum, air and oxygen atmosphere

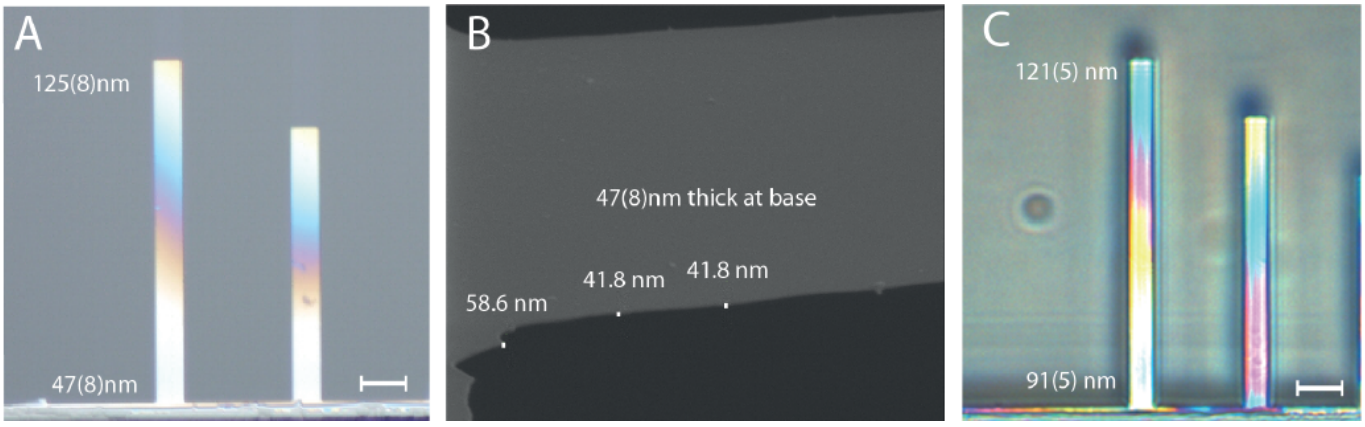

Figure 10.4: Examples of thin single-crystal diamond cantilevers fabricated using the method. A) Optical image of two sub-100-nm thick cantilever devices. The longer cantilever is 240 μm in length and has a thickness of 47(8) nm at the base and 125(8) nm at the tip, respectively. B) Scanning electron microscopy image of the same cantilever, measuring a base thickness of about 50 nm. C) Optical image of two other cantilever devices exhibiting a sub-100-nm thickness at the base. Scale bars are 20 μm

Chapter 11

Publications

A.A. Abdumalikov, J.M. Fink, K. Juliusson, M. Pechal, S. Berger, A. Wallraff, and S. Filipp
Experimental Realization of Non-Abelian Non-Adiabatic Geometric Gates
Nature **496**, 482 (2013)

S. Baer, C. Rössler, T. Ihn, K. Ensslin, C. Reichl, and W. Wegscheider
Cyclic Depopulation of Edge States in a large Quantum Dot
N. J. Phys. **15**, 023035 (2013)

A. Kozikov, C. Rössler, T. Ihn, K. Ensslin, C. Reichl, and W. Wegscheider
Interference of electrons in backscattering through a quantum point contact
N. J. Phys. **15**, 013056 (2013)

J. Basset, D.-D. Jarausch, A. Stockklauser, T. Frey, C. Reichl, W. Wegscheider, T. Ihn, K. Ensslin, and A. Wallraff
Single-electron Double Quantum Dot Dipole-Coupled to a Single Photonic Mode
Phys. Rev. B **88**, 125312 (2013)

F. Bauer, J. Heyder, E. Schubert, D. Borowsky, D. Taubert, B. Bruognolo, D. Schuh, W. Wegscheider, J. von Delft, and S. Ludwig
Microscopic Origin of the 0.7-Anomaly in Quantum Point Contacts
Nature **501**, 73 (2013)

R. Bergamaschini, F. Isa, C.V. Falub, P. Niedermann, E. Müller, G. Isella, H. von Känel, and L. Miglio
Self-aligned Ge and SiGe epitaxy on dense Si pillar arrays
Surf. Sci. Rpts. **68**, 390-417 (2013)

S. Berger, M. Pechal, A.A. Abdumalikov Jr., C. Eichler, L. Steffen, A. Fedorov, A. Wallraff, and S. Filipp
Exploring the effect of noise on the Berry phase
Phys. Rev. Lett.**87**, 060303(R) (2013)

S. Bietti, A. Scaccabarozzi, C. Frigeri, M. Bollani, E. Bonera, C.V. Falub, H. von Känel, L. Miglio, and S. Sanguinetti
Monolithic integration of optical grade GaAs on Si (001) substrates deeply patterned at a micron scale
Applied Physics Letters **103**, 262106 (2013)

D. Bischoff, A. Varlet, P. Simonet, T. Ihn, and K. Ensslin
Electronic triple-dot transport through a bilayer graphene island with ultrasmall constrictions
N. J. Physics **15**, 083029 (2013)

L. Bockhorn, A. Hodaei, D. Schuh, W. Wegscheider, and R.J. Haug
Magnetoresistance in a High Mobility Two-dimensional Electron System as a Function of Sample Geometry
Journal of Physics Conference Series **456**, UNSP012003 (2013)

F.R. Braakman, P. Barthelemy, C. Reichl, W. Wegscheider, and L.M.K. Vandersypen
Photon- and Phonon-assisted Tunneling in the Three-dimensional Charge Stability Diagram of a Triple Quantum Dot Array
App. Phys. Lett. **102**, 112110 (2013)

F.R. Braakman, P. Barthelemy, C. Reichl, W. Wegscheider, and L.M.K. Vandersypen
Long-distance Coherent Coupling in A Quantum Dot Array
Nature Nanotechnology **8**, 432-437 (2013)

A.A. Bush, N. Büttgen, A.A. Gippius, V.N. Glazkov, W. Kraetschmer, L.A. Prozorova, L.E. Svistov, A.M. Vasiliev, A. Zheludev, and A. M. Farutin
Magnetic structure of the frustrated S-1/2 chain magnet $LiCu_2O_2$ doped with nonmagnetic Zn
Phys. Rev. B **88**, 104411 (2013)

Ch. Butschkow, E. Reiger, A. Rudolph, S. Geissler, D. Neumaier, M. Soda, D. Schuh, G. Woltersdorf, W. Wegscheider, and D. Weiss
Origin of Negative Magnetoresistance of GaAs/(Ga,Mn)As Core-shell Nanowires
Phys. Rev. B **87**, 245303 (2013)

P. Butti, I. Shorubalko, U. Sennhauser, and K. Ensslin
Finite element simulations of graphene based three-terminal nanojunction rectifiers
J. Appl. Phys. **114**, 033710 (2013)

F. Casola, T. Shiroka, A. Feiguin, S. Wang, M.S. Grbic, M. Horvatic, S.Kraemer, S. Mukhopadhyay, K. Conder, C. Berthier, H.-R. Ott, H.M. Ronnow, Ch. Ruegg, and J. Mesot
Field-Induced Quantum Soliton Lattice in a Frustrated Two-Leg Spin-1=2 Ladder
Phys. Rev. Lett. **110**, 187201 (2013)

J. Chang, M. Mansson, S. Pailhes, T. Claesson, O.J. Lipscombe, S.M. Hayden, L. Patthey, O. Tjernberg, and J. Mesot
Anisotropic breakdown of Fermi liquid quasiparticle excitations in overdoped $La_{2-x}Sr_xCuO_4$
Nature Communications **4**, 2559 ,doi:10.1038/ncomms3559 (2013)

Ch. Charpentier, S. Fält, Ch. Reichl, F. Nichele, A.N. Pal, P. Pietsch, T. Ihn, K. Ensslin, and W. Wegscheider
Suppression of Bulk Conductivity in InAs/GaSb Broken Gap Composite Quantum Wells
Appl. Phys. Lett. **103**, 112102 (2013)

S. Chillal, M. Thede, F.J. Litterst, S.N. Gvasaliya, T.A. Shaplygina, S.G. Lushnikov, and A. Zheludev
Microscopic Coexistence of Antiferromagnetic and Spin-Glass States
Phys. Rev. B **87**, 220403(R) (2013)

M.J.G. Cottet, M. Cantoni, B. Mansart, D.T.L. Alexander, C. Hebert, N.D. Zhigadlo, J. Karpinski, and F. Carbone
Quantitative imaging of flux vortices in the type-II superconductor MgB_2 using cryo-Lorentz transmission electron microscopy
Phys. Rev. B **88**, 014505 (2013)

I.L. Drichko, V.A. Malysh, I.Yu. Smirnov, A.V. Suslov, O.A. Mironov, M. Kummer, H. von Känel
Acoustoelectric effects in very high-mobility p-SiGe/Ge/SiGe heterostructure.Part II
J. Appl. Phys. **114**, 074302 (2013)

A. Dusza, A. Lucarelli, J.-H. Chu, I.R. Fisher, and L. Degiorgi
Distribution of optical spectral weight in detwinned $Ba(Fe_{1-x}Co_x)_2As_2$
J. Supercond. Nov. Magn. **26**, 2603 (2013)

H.-M. Eiter, M. Lavagnini, R. Hackl, E.A. Nowadnick, A.F. Kemper, T.P. Devereaux, J.-H. Chu, J.G. Analytis, I.R. Fisher, and L. Degiorgi
Alternative route to charge density wave formation in multiband systems
Proc. Natl. Acad. Sci. USA **110**, 64 (2013)

C.V. Falub, M. Meduna, D. Chrastina, F. Isa, A. Marzegalli, T. Kreiliger, A. G. Taboada, G. Isella, L. Miglio, A. Dommann, and H. von Känel
Perfect crystals grown from imperfect interfaces
Scientific Reports **3**, 2276 (2013)

C.V. Falub, T. Kreiliger, F. Isa, A. G. Taboada, M. Meduna, F. Pezzoli, R. Bergamaschini, A. Marzegalli, E. Müller, D. Chrastina, G. Isella, A. Neels, P. Niedermann, A. Dommann, L. Miglio, and H. von Känel
3D Heteroepitaxy of Mismatched Semiconductors on Silicon
Thin Solid Films (2013)

L. Fang, Y. Jia, V. Mishra, C. Chaparro, V.K. Vlasko-Vlasov, A.E. Koshelev, U. Welp, G.W. Crabtree, S. Zhu, N.D. Zhigadlo, S. Katrych, J. Karpinski, and W.K. Kwok
Huge critical current density and tailored superconductivity anisotropy in $SmFeAsO_{0.8}F_{0.15}$ by low-density columnar-defect incorporation
Nature Communications **4**, 2655 (2013)

A. Fognini, and Y. Acremann
Free Electron Lasers, Magnetism and Synchrotron Radiation: Towards the Fourth Generation Light Sources
Springer Proceedings in Physics **151**, 139 (2013)

R.S. Gonnelli, M. Tortello, D. Daghero, P.Pecchio, S.Galasso, V.A. Stepanov, Z.Bukowski, N.D. Zhigadlo, J. Karpinski, K. Iida, and B. Holzapfel
The Order-Parameter Symmetry and Fermi Surface Topology of 122 Fe-Based Superconductors: A Point-Contact Andreev-Reflection Study
J. Supercond.Nov.Magn. **26**, 1331-1337(2013)

R.T. Gordon, N.D. Zhigadlo, S. Weyeneth, S. Katrych, and R. Prozorov
Conventional superconductivity and hysteretic Campbell penetration depth in single crystals $MgCNi_3$
Phys. Rev. B **87**, 094520 (2013)

C.E. Graves, A.H. Reid, T. Wang, B. Wu, S. de Jong, K. Vahaplar, I. Radu, D.P. Bernstein, M. Messerschmidt, L. Müller, R. Coffee, M. Bionta, S.W. Epp, R. Hartmann, N. Kimmel, G. Hauser, A. Hartmann, P. Holl, H. Gorke, J.H. Mentink, A. Tsukamoto, A. Fognini, J.J. Turner, W.F. Schlotter, D. Rolles, H. Soltau, L. Strüder, Y. Acremann, A.V. Kimel, A. Kirilyuk, Th. Rasing, J. Stöhr, A. O. Scherz, and H. A. Dürr
Nanoscale spin reversal by non-local angular momentum transfer following ultrafast laser excitation in ferrimagnetic GdFeCo
Nature Materials **12**, 293 (2013)

N. Harrison, P.J.W. Moll, S.E. Sebastian, L. Balicas, M.M. Altarawneh, J.-X. Zhu, P.H. Tobash, F. Ronning, E.D. Bauer, and B. Batlogg
Magnetic field-tuned localization of the 5f-electrons in URu_2Si_2
Phys. Rev. B **88**, 241108(R)(2013)

D. Hüvonen, G. Ballon, and A. Zheludev
Field-concentration phase diagram of a quantum spin liquid with bond defects
Phys. Rev. B **88**, 094402 (2013)

F. Isa, A. Marzegalli, A.G. Taboada, C.V. Falub, G. Isella, F. Montalenti, H. von Känel, and L. Miglio
Onset of vertical threading dislocations in Si1-xGex/Si(001) at a critical Ge concentration
Appl. Phys. Lett. Materials **1**, 052109 (2013)

M. Jeong, H. Mayaffre, C. Berthier, D. Schmidiger, A. Zheludev, and M. Horvatic
Attractive Tomonaga-Luttinger Liquid in a Quantum Spin Ladder
Phys. Rev. Lett. **111**, 106404 (2013)

B. Küng, C. Rössler, M. Beck, M. Marthaler, D.S. Golubev, Y. Utsumi, T. Ihn, and K. Ensslin
Test of the fluctuation theorem for single-electron transport
J. Appl. Phys. **113**, 136507 (2013)

S. Katrych, K. Rogacki, A. Pisoni, S. Bosma, S. Weyeneth, R. Gaal, N.D. Zhigadlo, J. Karpinski, and L. Forro
$Pr_4Fe_2As_2Te_{1-x}O_4$: A layered FeAs-based superconductor
Phys. Rev. B **87**, 180508(R) (2013)

E.M. Kendirlik, S. Sirt, S.B. Kalkan, W. Dietsche, W. Wegscheider, S. Ludwig, and A. Siddiki
Anomalous Resistance Overshoot in the Integer Hall Effect
Scientific Reports **3**, 3133 (2013)

Y. Komijani, T. Choi, F. Nichele, K. Ensslin, T. Ihn, D. Reuter and A. D. Wieck
Counting statistics of hole transfer in a p-type GaAs quantum dot with dense excitation spectrum
Phys. Rev. B **88**, 035417 (2013)

Y. Komijani, M. Csontos, T. Ihn, K. Ensslin, Y. Meir, D. Reuter, and A. D. Wieck
Origins of conductance anomalies in a p-type GaAs quantum point contact
Phys. Rev. B **87**, 245406 (2013)

Y. Komijani, M. Csontos, I. Shorubalko, U. Zuelicke, T. Ihn, K. Ensslin, D. Reuter, and A. D. Wieck
Anisotropic Zeeman shift in p-type GaAs quantum point contacts
Europhys. Lett. **102**, 37002 (2013)

K. Korzekwa, C. Gradl, M. Kugler, S. Furthmeier, M. Griesbeck, M. Hirmer, D. Schuh, W. Wegscheider, T. Kuhn, C. Schüller, T. Korn, and P. Machnikowski
Spin Dynamics in p-doped Semiconductor Subject to a Magnetic Field Titled from the Voigt Geometry
Phys. Rev. B **88**, 155303 (2013)

A.A. Kozikov, C. Rössler, T. Ihn, K. Ensslin, C. Reichl, and W. Wegscheider
Interference of Electrons in Backscattering Through a Quantum Point Contact
N. J. Phys. **15**, 013056 (2013)

A.A. Kozikov, D. Weinmann, C. Rössler, T. Ihn, K. Ensslin, C. Reichl, and W. Wegscheider
Imaging Magnetoelectric Subbands in Ballistic Constrictions
N. J. Phys. **15**, 083005 (2013)

A. Kriisa, R.G. Mani, and W. Wegscheider
Topological Hall Insulator
AIP Conf. Proc. **1566**, 195 (2013)

D. Kutnyakhov, P. Lushchyk, A. Fognini, D. Perriard, M. Kolbe, K. Medjanik, E. Fedchenko, S.A. Nepijko, H.J. Elmers, G. Salvatella, C. Stieger, R. Gort, T. Bahler, T. Michlmayer, Y. Acremann, A. Vaterlaus, F. Giebels, H. Gollisch, R. Feder, C. Tusche, A. Krasyuk, J. Kirschner, and G. Schonhense
Imaging spin filter for electrons based on specular reflection from iridium (001)
Ultramicroscopy **130**, 63 (2013)

K. Lalumière, B.C. Sanders, A.F. van Loo, A. Fedorov, A. Wallraff, and A. Blais
Input-output theory for waveguide QED with an ensemble of inhomogeneous atoms
Phys. Rev. Lett.**A** 88, 043806 (2013)

G. Lamura, T. Shiroka, P. Bonfà, S. Sanna, F. Bernardini, R. De Renzi, R. Viennois, E. Giannini, A. Piriou, N. Emery, M. R. Cimberle, and M. Putti
A magnetic glassy phase in $Fe_{1-y}Se_xTe_{1-x}$ single crystals
Journal of Physics: Condensed Matter **25**, 156004 (2013)

G. Lamura, T. Shiroka, P. Bonfà, S. Sanna, R. De Renzi, C. Baines, H. Luetkens, J. Kajitani, Y. Mizuguchi, O. Miura, K. Deguchi, S. Demura, Y. Takano, and M. Putti
s-wave pairing in the optimally doped $LaO_{0.5}F_{0.5}BiS_2$ superconductor
Phys. Rev. B **88**, 0005xx(R) (2013)

C. Lang, C. Eichler, L. Steffen, J.M. Fink, M.J. Woolley, A. Blais, and A. Wallraff
Correlations, indistinguishability and entanglement in Hong-Ou-Mandel experiments at microwave frequencies
Nature Physics **9**, 345-348 (2013)

G. Li, G. Grissonnanche, B.S. Conner, F. Wolff-Fabris, C. Putzke, N.D. Zhigadlo, S. Katrych, Z. Bukowski, J. Karpinski, and L. Balicas
Vortex lock-in transition and evidence for transitions among commensurate kinked vortex configurations in single-layered Fe arsenides
Phys. Rev. B **87**, 100503(R) (2013)

E. Liarokapis, A. Antonakos, N.D. Zhigadlo, S. Katrych, and J. Karpinski
Lattice Effects Across the Phase Diagram of Pnictides
J. Supercond. Nov. Magn. **26**, 4, 1325-1330 (2013)

E. Liarokapis, M. Calamiotou, N.D. Zhigadlo, S. Katrych, and J. Karpinski
Non-linear lattice response of Sm oxypnictides to hydrostatic pressure
J. Phys.: Chem. Solids **74**, 1465-1469 (2013)

M. Lieberherr, A. Vaterlaus und C. Wagner
Zähmen der Unendlichkeit
Bulltin VSMP **122**, 15 (2013)

A.F. van Loo, A. Fedorov, K. Lalumière, B.C. Sanders, A. Blais, and A. Wallraff
Photon-Mediated Interactions Between Distant Artificial Atoms
Science **342**,1494-1496, (2013)

M. Loretz, T. Rosskopf, C.L. Degen
Radio-frequency magnetometry using a single electron spin
Physical Review Letters **110**, 017602 (2013)

J.C. Loudon, C.J. Bowell, N.D. Zhigadlo, J. Karpinski, and P.A. Midgley
Magnetic structure of individual flux vortices in superconducting MgB_2 derived using transmission electron microscopy
Phys. Rev. B **87**, 144515 (2013)

T. Müller, T. Choi, S. Hellmüller, K. Ensslin, T. Ihn, and S. Schön
A circuit analysis of an in situ tunable radio-frequency quantum point contact
Rev. Sci. Instrum. **84**, 083902 (2013)

C. Maissen, G. Scalari, F. Valmorra, C. Reichl, D. Schuh, W. Wegscheider, M. Beck, S. De Liberato, D. Hagenmüller, C. Ciuti, and J. Faist
Influence of Resonator Design on Ultrastrong Coupling Between a Two-dimensional Electron Gas and a THz Metamaterial
Proceedings of SPIE **8623**, 86231M (2013)

R.G. Mani, A.N. Ramanayaka, T. Ye, M.S. Heimbeck, H.O. Everitt, and W. Wegscheider
Terahertz Photovoltaic Detection of Cyclotron Resonance in the Regime of Radiation-induced Magnetoresistance Oscillations
Phys. Rev. B **87**, 245308 (2013)

R.G. Mani, A. Kriisa, and W. Wegscheider
Size-dependent Giant-magnetoresistance in Millimeter Scale GaAs/AlGaAs 2D Electron Devices
Scientific Reports **3**, 2747 (2013)

R.G. Mani, A.N. Ramanayaka, and W. Wegscheider
Observation of Linear-polarization-sensitivity in the Microwave-Radiation-Induced Magnetoresistance Oscillations
AIP Conf. Prof. **1566**, 235 (2013)

A. Marzegalli, F. Isa, H. Groiss, E. Müller, C. V. Falub, A.G. Taboada, P. Niedermann, G.Isella, F. Schäffler, F. Montalenti, H. von Känel, and L. Miglio
Unexpected dominance of vertical dislocations in high-misfit Ge/Si(001)films and their elimination by deep substrate patterning
Advanced Materials **25**, 4407 (2013)

M. Medarde, M. Mena, J.L. Gavilano, E. Pomjakushina, J. Sugiyama, K. Kamazawa, V.Yu. Pomjakushin, D. Sheptyakov, B. Batlogg, H.R. Ott, M. Mansson, and F. Juranyi
1D to 2D Na+ Ion Diffusion Inherently Linked to Structural Transitions in $Na_{0.7}CoO_2$
Phys. Rev. Lett. **110**, 266401 (2013)

T. Mertelj, L. Stojchevska, N.D. Zhigadlo, J. Karpinski, and D. Mihailovic
Normal state bottleneck and nematic fluctuations from femtosecond quasi-particle relaxation dynamics in Sm(Fe,Co)AsO
Phys. Rev. B **87**, 174525 (2013)

T.U. Michlmayr, A. Fognini, T. Bühler, G. Salvatella Orgilles, C. Wetli, A. Vaterlaus, and Y. Acremann
A mobile UHV-system designed for femtosecond time, energy and spin resolved photoelectron spectroscopy
Journal of the Korean Physical Society **62**, 2202 (2013)

P.J.W. Moll, L. Balicas, V. Geshkenbein, G. Blatter, J. Karpinski, N.D. Zhigadlo, and B. Batlogg
Transition from slow Abrikosov to fast moving Josephson vortices in iron pnictide superconductors
Nature Materials **12**, 134-138 (2013)

B. Nafradi, T. Keller, H. Manaka, U. Stuhr, A. Zheludev, and B. Keimer
Bond Randomness Induced Magnon Decoherence in a Spin-1/2 Ladder Compound
Phys. Rev. B **87**, 020408(R) (2013)

F. Nichele, Y. Komijani, S. Hennel, C. Gerl, W. Wegscheider, D. Reuter, A.D. Wieck, T. Ihn, and K. Ensslin
Aharonov-Bohm rings with strong spin-orbit interaction: the role of sample-specific properties
N. J. Physics **15**, 033029 (2013)

F. Nissen, J.M. Fink, J.A. Mlynek, A. Wallraff, and J. Keeling
Collective Suppression of Linewidths in Circuit QED
Phys. Rev. Lett.**110**, 203602 (2013)

K. Ohashi, T. Rosskopf, H. Watanabe, M. Loretz, Y. Tao, R. Hauert, S. Tomizawa, T. Ishikawa, J. Ishi-Hayase, S. Shikata, C. L. Degen, and K. M. Itoh
Negatively Charged Nitrogen-Vacancy Centers in a 5 nm Thin 12C Diamond Film
Nano Letters **13**, 4733 (2013)

G. Petersen, E.A. Hoffmann, D. Schuh, W. Wegscheider, G. Giedke, and S. Ludwig
Large Nuclear Spin Polarization in Gate-Defined Quantum Dots Using a Single-Domain Nanomagnet
Phys. Rev. Lett. **110**, 177602 (2013)

G. Prando, O. Vakaliuk, S. Sanna, G. Lamura, T. Shiroka, P. Bonfà, P. Carretta, R. De Renzi, H.-H. Klauss, C.G.F. Blum, S. Wurmehl, C. Hess, and B. Büchner
Role of in-plane and out-of-plane dilution in CeFeAsO: Charge doping versus disorder
Phys. Rev. B **87**, 174519 (2013)

C. Rössler, T. Krähenmann, S. Baer, T. Ihn, K. Ensslin, C. Reichl, and W. Wegscheider
Tunable Charge Detectors for Semiconductor Quantum Circuits
N. J. Phys. **15**, 033011 (2013)

N. Ramanayaka, R.G. Mani, and W. Wegscheider
Electron Heating Due to Microwave Photoexcitation in the High Mobility GaAs/AlGaAs Two Dimensional Electron System
AIP Conf. Proc. **1566**, 233 (2013)

C. Rastovski, K.J. Schlesinger, W.J. Gannon, C.D. Dewhurst, L. DeBeer-Schmitt, N.D. Zhigadlo, J. Karpinski, and M. R. Eskildsen
Persistence of metastable vortex lattice domains in MgB_2 in the presence of vortex motion
Phys. Rev. Lett. **111**, 107002 (2013)

E. Razzoli, G. Drachuck, A. Keren, M. Radovic, N.C. Plumb, J.Chang, Y.-B. Huang, H. Ding, J. Mesot, and M.

Shi
Evolution from a Nodeless Gap to $d_{x^2-y^2}$-Wave in Underdoped $La_{2-x}Sr_xCuO_4$
Phys. Rev. Lett. **110**, 047004 (2013)

M. Richter, E. Uccelli, A.G. Taboada, D. Caimi, N. Daix, M. Sousa, C. Marchiori, H. Siegwart, C.V. Falub, H. von Känel, F. Isa, G. Isella, A. Pezous, A. Dommann, P. Niedermann, and J. Fompeyrine
Heterointegration by molecular beam epitaxy: (In,Ga)As/GaAs quantum wells on GaAs,Ge,Ge/Si and Ge/Si pillars
J. Cryst. Growth **378**, 109-112 (2013)

A.T. Romer, J. Chang, N.B. Christensen, B.M. Andersen, K. Lefmann, L.Mahler, J. Gavilano, R. Gilardi, Ch. Niedermayer, H.M. Ronnow, A. Schneidewind, P. Link, M. Oda, M. Ido, N. Momono, and J. Mesot
Glassy low-energy spin fluctuations and anisotropy gap in $La_{1.88}Sr_{0.12}CuO_4$
Phys. Rev. B **87**, 144513 (2013)

H. Saadaoui, T. Shiroka, A. Amato, C. Baines, H. Luetkens, E. Pomjakushina, V. Pomjakushin, J. Mesot, M. Pikulski, and E. Morenzoni
μSR and NMR study of the superconducting Heusler compound YPd_2Sn
Phys. Rev. B **88**, 094518 (2013)

G.A. Salvatore, N. Münzenrieder, C. Barraud, L. Petti, C. Zysset, L. Büthe, K. Ensslin, and G. Tröster
Fabrication and Transfer of Flexible Few-Layers MoS_2 Thin Film Transistors to Any Arbitrary Substrate
ACS Nano **7**, 8809 (2013)

S. Sanna, P. Carretta, R. De Renzi, G. Prando, P. Bonfà, M. Mazzani, G. Lamura, T. Shiroka, Y. Kobayashi, and M. Sato
Onset of magnetism in optimally electron-doped $LFe_{1-x}Ru_xAsO_{1-y}F_y$ (L = La, Nd, or Sm) superconductors around x = 1/4
Phys. Rev. B **87**, 134518 (2013).

G. Scalari, C. Maissen, D. Hagenmueller, S. De Liberato, C. Ciuti, C. Reichl, W. Wegscheider, D. Schuh, M. Beck, and J. Faist
Ultrastrong Light-matter Coupling at Terahertz Frequencies with Split Ring Resonators and Inter-Landau Level Transitions
Journal of App. Phys. **113**, 136510 (2013)

D. Schmidiger, P. Bouillot, G. Ehlers, S. Mühlbauer, A. M. Tsvelik, C. Kollath, T. Giamarchi, and A. Zheludev
Symmetric and asymmetric excitations of a strong-leg quantum spin ladder
Phys. Rev. B **88**, 094411 (2013)

D. Schmidiger, P. Bouillot, T. Guidi, R. Bewley, C. Kollath, T. Giamarchi, and A. Zheludev
Spectrum of a magnetized strong-leg quantum spin ladder
Phys. Rev. Lett. **111**, 107202 (2013)

F. Schrettle, S. Krohns, P. Lunkenheimer, A. Loidl, E. Wulf, T. Yankova and A. Zheludev
Multiferroic quantum criticality in a frustrated spin liquid
Phys. Rev. B **87**, 121105(R) (2013)

M. Shafiei, K.C Nowack, C. Reichl, W. Wegscheider, and L.M.K. Vandersypen
Resolving Spin-Orbit- and Hyperfine-Mediated Electric Dipole Spin Resonance in a Quantum Dot
Phys. Rev. Lett. **110**, 107601 (2013)

T. Shiroka, M. Thede, L. Wittenfeld, F.J. Litterst, S. Cahen, H. Rida, N. Emery, J.-F. Marâché, P. Lagrange, and C. Hérold
Competing magnetic interactions in the graphite-intercalation compound $Li_{0.25}Eu_{1.95}C_6$
Carbon **63**, 294 (2013)

T. Shiroka, F. Casola, W. Lorenz, K. Prsa, A. Zheludev, H.-R. Ott, and J. Mesot
Impact of strong disorder on the static magnetic properties of the spin-chain compound $BaCu_2SiGeO_7$
Phys. Rev. B **88**, 054422 (2013)

G. Simutis, S. Gvasaliya, M. Månsson, A. L. Chernyshev, A. Mohan, S. Singh, C. Hess, A. T. Savici, A. I. Kolesnikov, A. Piovano, T. Perring, I. Zaliznyak, B. Büchner, and A. Zheludev
Spin pseudogap in Ni-doped $SrCuO_2$
Phys. Rev. Lett. **111**, 067204 (2013)

L. Steffen, Y. Salathé, M. Oppliger, P. Kurpiers, M. Baur, C. Lang, C. Eichler, G. Puebla-Hellmann, A. Fedorov, and A. Wallraff
Deterministic quantum teleportation with feed-forward in a solid state system
Nature **500**, 319-322 (2013)

R. Stoop, V. Saase, C. Wagner, B. Stoop, and R. Stoop
Beyond Scale-Free Small-World Networks: Cortical Columns for Quick Brains
Phys. Rev. Lett. **110**, 108105 (2013)

A.G. Taboada, T. Kreiliger, C.V. Falub, M. Richter, F. Isa, E. Müller, E. Uccelli, P. Niedermann, A. Neels, G. Isella, J. Fompeyrine, A. Dommann, H. von Känel
Integration of GaAs on Ge/Si towers by MOVPE
Mat. Res. Soc. Symp. Proc. **1538**, 283-289 (2013)

Y. Tao, C. L. Degen
Facile fabrication of single-crystal-diamond nanostructures with ultra high aspect ratio
Advanced Materials **25**, 3962 (2013)

D. Tutuc, A.W. Heine, D. Schuh, W. Wegscheider, and R.J. Haug
Exchange Interaction in Chirally Coupled Quantum Dots
Journal of Physics Conference Series **456**, UNSP012014 (2013)

P. Wachter, and N.D. Zhigadlo
Physical Properties of stoichiometric CeN single crystals
Results in Physics **3**, 235 (2013)

P. Wachter, and B. Bucher
Exciton condensation and its influence on the specific heat
Physica B **408**, 51 (2013)

A. Wallraff, A. Stockklauser, T. Ihn, J.R. Petta, and A. Blais
Comment on Vacuum Rabi Splitting in a Semiconductor Circuit QED System
Phys. Rev. Lett. **111**, 249701 (2013)

M. J. Woolley, C. Lang, C. Eichler, A. Wallraff, and A. Blais
Signatures of Hong-Ou-Mandel Interference at Microwave Frequencies
New J. Phys. **15**, 105025-19 (2013)

E. Wulf, D. Hüvonen, J.-W. Kim, A. Paduan-Filho, E. Ressouche, S. Gvasaliya, V. Zapf, and A. Zheludev
Criticality in a disordered quantum antiferromagnet by neutron diffraction
Phys. Rev. B **88**, 174418 (2013)

W. Xie, K. Willa, Y. Wu, R. Häusermann, K. Takimiya, B. Batloggg, and C.D. Frisbie
Temperature-Independent Transport in High-Mobility Dinaphtho-Thieno-Thiophene (DNTT) Single Crystal Transistors
Advanced Materials **25**, 3478-3484 (2013)

N. Xu, X. Shi, P.K. Biswas, C.E. Matt, R.S. Dhaka, Y. Huang, N.C. Plumb, M. Radovic, J.H. Dil, E. Pomjakushina, K. Conder, A. Amato, Z. Salman, D.McK. Paul, J. Mesot, H. Ding, and M. Shi
Surface and bulk electronic structure of the strongly correlated system SmB_6 and implications for a topological Kondo insulator
Phys. Rev. B **88**,121102(R)(2013)

T. Ye, R.G. Mani, and W. Wegscheider
Remotely Sensed Transport in Microwave Photoexcited GaAs/AlGaAs Two-dimensional Electron System
App. Phys. Lett. **102**, 242113 (2013)

T. Ye, R.G. Mani, and W. Wegscheider
Remote Sensor Response Study in the Regime of the Microwave Radiation-induced Magnetoresistance Oscillations
App. Phys. Lett. **103**, 192106 (2013)

T. Ye, R.G. Mani, and W. Wegscheider
Study of Reflection and Transport in the Microwave Photo-excited GaAs/AlGaAs Two Dimensional Electron System
AIP Conf. Proc. **1566**, 281 (2013)

D. Zanin, M. Erbudak, L.G. De Pietro, H. Cabrera, A. Redmann, A. Fognini, T. Michlmayr, Y. Acremann, D. Pescia, and U. Ramsperger
The topografiner with energy analysis
Vacuum Nanoelectronics Conference (2013)

A. Zheludev, and T. Roscilde
Dirty-boson physics with magnetic insulators (Physique des bosons sales avec des isolants magnétiques)
C. R. Physique **14** 740–756 (2013)

N.D. Zhigadlo
Growth of whisker-like and bulk single crystals of PrFeAs(O,F) under high pressure
J. Cryst. Growth **382**, 75-79 (2013)

Chapter 12

Presentations

(* = invited talk)

***=eingeladen**

12.1 Talks

Abdumalikov, A.
Experimental realization of non-abelian geometric gates with a superconducting three-level system
APS March Meeting, Baltimore, Maryland, USA, 18.03.2013

$\star$ Acremann, Y.
Ultrafast loss of the "classical magnetization"
WUPCOM, Reit im Winkel, Germany, 27.02.2013

$\star$ Acremann, Y.
Ultrafast x-ray sources for magnetism
Workshop on magnetism, Nancy, France, 19.09.2013

$\star$ Allan, M.
Discovery of the Nematic Parent State and the Anisotropic Energy Gap Structure of Iron-based High-T_c Superconductors
APS March Meeting, Baltimore, Maryland, USA, 18.03.2013

$\star$ Allan, M.
Imaging Cooper pairing in iron-based and heavy fermion superconductors
MPI Stuttgart, Germany, 18.04.2013

Allan, M.
Material science on the atomic scale
MRC Graduate Symposium, ETH Zurich, Zurich, Switzerland, 13.06.2013

$\star$ Allan, M.
Electronic nematicity in iron-based superconductors
SNS2013, Berkeley, CA, USA, 24.06.2013

Balthasar, B.
Modeling the Dynamics of Charge Trapping and Release Processes in Organic Semiconductor Devices
MRS Spring Meeting, San Francisco, U.S.A., 01.04.2013

Balthasar, B.
Near-ideal Subthreshold Behavior in Organic Single Crystal Field-Effect Transistors due to Low Interface and Bulk Trap Densities
Int. Semiconductor Device Research Symposium (ISDRS), Washington, USA, 11.12.2013

⋆ Barraud, C.
Transport in BN/graphene heterostructures
CC3DMR, Jeju Island, South Korea, 24.06.2013

Basset, J.
Dipole-coupling a single-electron double quantum dot to a microwave resonator
Les rencontres du Vietnam on Nanophysics: from fundamentals to applications, Quy-Nhon, Vietnam, 04.08.2013

Basset, J.
Single-electron double quantum dot dipole-coupled to a microwave resonator
Frontiers in quantum engineered devices, Obergurgl, Austria, 19.08.2013

⋆ Basset, J.
Single-electron double quantum dot dipole-coupled to a single photonic mode
Lund University, Lund, Sweden, 22.10.2013

⋆ Batlogg, B.
Fe-based superconductors in very high magnetic fields
Intl. Workshop on Novel Superconductors, Donnersbach, Austria,10.02.2013

⋆ Batlogg, B.
Slow Abrikosov- to fast moving Josephson-vortex transition in iron-pnictide superconductors
MaNEP Conference, Les Diablerets, Switzerland, 27.06.2013

⋆ Batlogg, B.
Materials with strong electron correlation: structure and properties
PSI Summer School on Condensed Matter Research, Zuoz, Switzerland, 17.08.2103

⋆ Batlogg, B.
Der Traum von der Supraleitung bei Zimmertemperatur
Volkshochschule Zurich, Switzerland, 11.09.2013

⋆ Batlogg, B.
New materials based condensed matter physics research
Swiss-Japan Workshop, ETH Zurich, Zurich, Switzerland, 21.11.2013

⋆ Batlogg, B.
Organic molecular semiconductors: approaching the trap free limit
NTU Singapore, 08.11.2013

⋆ Batlogg, B.
The power of the periodic table: Solid state chemistry makes solid state physics happen
NTU Singapore, 12.11.2013

⋆ Batlogg, B.
Charge transport and trapping in organic semiconductors
Rutgers University, New Jersey, USA, 27.11.2013

⋆ Batlogg, B.
Fe-based superconductors in extreme magnetic fields: H_{c2}, J_c and vortex dynamics
Rutgers University, New Jersey, USA, 27.11.2013

⋆ Batlogg, B.
Charge transport and trapping in organic semiconductors: approaching the trap-free limit in single-crystal FETs
NIST, Gaithersburg, VA, USA, 02.12.2013

⋆ Batlogg, B.
Charge transport and trapping in organic semiconductors: approaching the trap-free limit in single-crystal FETs
Intl. Workshop on Interface Science for Novel Physical Properties and Electronics, Okayama, Japan, 09.12.2013

Bischoff, D.
Graphene Triple Dots
QSIT Lunch Seminar January 2013, Zürich, Switzerland

⋆ Bischoff, D.
Towards a Better Understanding of Graphene Nanodevices
Graphene Week 2013, Chemnitz, Germany, 03.06.2013

Bischoff, D.
Graphene Nanostrukturen
Tag für Physik und Unterricht, Zürich, Switzerland, 13.11.2013

Casola, F.
Aspects of quantum magnetism in quasi one-dimensional materials
Harvard University, Boston, USA, 04.01.2013

Ch. Charpentier
MBE growth of high purity III/V semiconductor heterostructures
Evaluation D-Phys, ETH Zurich, Switzerland, 22.4.2013

Chillal, S.
Microscopic Coexistence of Antiferromagnetic and Spin-Glass States
APS March meeting, Baltimore, USA, 22.03.2013

Chillal, S.
Microscopic Coexistence of Antiferromagnetic and Spin-Glass States
The International Workshop on Relaxor Ferroelectrics, Saint Petersburg, Russia, 04.07.2013

⋆ Degiorgi, L.
Chasing the nematic phase in detwinned $Ba(Co_xFe_{1-x})_2As_2$ with optical investigations
Internal MaNEP Workshop 2013, Neuchatel, Switzerland, 23.01.2013

⋆ Degiorgi, L.
Chasing the nematic phase in detwinned $Ba(Co_xFe_{1-x})_2As_2$ with optical investigations
Solid State Physics Seminar at Brookhaven National Laboratories, Brookhaven, U.S.A., 14.03.2013

Degiorgi, L.
Chasing the nematic phase in detwinned $Ba(Co_xFe_{1-x})_2As_2$ with optical investigations
March Meeting of the American Physical Society, Baltimore, U.S.A., 18.03.2013

⋆ Degiorgi, L.
Chasing the nematic phase in detwinned $Ba(Co_xFe_{1-x})_2As_2$ with optical investigations
International Conference on Quantum in Complex Matter, Ischia, Italy, 27.05.2013

⋆ Degiorgi, L.
Chasing the nematic phase in detwinned $Ba(Co_xFe_{1-x})_2As_2$ with optical investigations
Condensed Matter Physics Seminar, Department of Physics Stanford University, Stanford, U.S.A., 06.06.2013

⋆ Degiorgi, L.
Chasing the nematic phase in detwinned $Ba(Co_xFe_{1-x})_2As_2$ with optical investigations
Special Condensed Matter Physics Seminar, Department of Physics University of California at San Diego, San Diego, U.S.A., 10.06.2013

⋆ Degiorgi, L.
Chasing the nematic phase in detwinned $Ba(Co_xFe_{1-x})_2As_2$ with optical investigations
Condensed Matter Physics Seminar, Department of Physics University of British Columbia, Vancouver,Canada, 13.06.2013

Eichler, C.
Qubit-Photon Entanglement and Hong-Ou-Mandel Interference with Propagating Microwaves
APS March Meeting, Baltimore, Maryland, USA, 19.03.2013

⋆ Eichler, C.
Probing the quantum properties of microwave radiation emitted from superconducting circuits
Institut fuer Theoretische Physik, Hannover, Germany, 23.04.2013

⋆ Eichler, C.
Photon-Qubit Entanglement and Hong-Ou-Mandel Interference at Microwave Frequencies
Workshop on Frontier between atomic and solid state physics, Ecole Normale Superieure, Paris, France, 17.07.2013

Eichler, C.
Qubit-Photon Entanglement and Hong-Ou-Mandel Interference with Propagating Microwaves
CCQED Conference on Resonator QED, Munich, Germany, 09.09.2013

⋆ Eichler, C.
Exploring quantum microwave radiation emitted from superconducting electronic circuits
Quantum Sciences Seminar, Departement of Physics, Princeton University, USA, 10.12.2013

⋆ Ensslin, K.
Waren Sie schon einmal gleichzeitig an zwei Orten? Quantenmechanik und Informationsverarbeitung
Seniorenkolleg Liechtenstein, Liechtenstein, 17.1.2013

⋆ Ensslin, K.
Charge detection in semiconductor quantum structures
EU network S^3 NANO Winter School, Windsor, United Kingdom, 3.2. 2013

⋆ Ensslin, K.
Confinement in graphene nanostructures
Seminar at Institute for Terahertz Science and Technology, University of California, Santa Barbara, USA, 7.2.2013

⋆ Ensslin, K.
Electronic Properties of Semiconductor Nanostructures
Gordon Research Conference on ”Nanomaterials for Applications in Energy Technology”, Ventura, USA, 3.2.2013

⋆ Ensslin, K.
Waren Sie schon einmal gleichzeitig an zwei Orten? Quantenmechanik und Informationsverarbeitung
Junge Wirtschaftskammer Luzern, Switzerland, 5.3.2013

⋆ Ensslin, K.
Single charge transport in nanostructures
Symposium on “Frontiers in Condensed Matter Sciences”, Fortaleza, Brazil, 8.4. 2013

⋆ Ensslin, K.
Single electrons in quantum structures
Physics colloquium, Federal University of Pernambuco, Recife, Brazil, 12.4.2013

⋆ Ensslin, K.
Quantum shot noise in quantum dots
Workshop at Institute for Nuclear Theory on “Quantum Noise”, Seattle, USA, 6.5.2013

⋆ Ensslin, K.
From quantum science to quantum technology
ABB lunch talk, Baden, Switzerland, 7.5.2013

⋆ Ensslin, K.
Waren Sie schon einmal gleichzeitig an zwei Orten? Quantenmechanik und Informationsverarbeitung
Senioren- und Generationen-Akademie Solothurn, Switzerland, 8.5.2013

⋆ Ensslin, K.
Confinement in graphene nanostructures
Workshop on nanostructured graphene, Antwerp, Belgium, 21.5.2013

Ensslin, K.
Mechanik
Kindervorlesung für 4.-6. Primarschulklasse, ETH Zürich, Switzerland, 4.6.2013

⋆ Ensslin, K.
Imaging of fractional quantum Hall states
School on “Contacts in Nanosystems”, Goslar, Germany, 13.6.2013

⋆ Ensslin, K.
Imaging of integer and fractional quantum Hall states
International conference on “Nanophysics: from fundamentals to applications”, IXth Rencontres du Vietnam, Quy-Nhon, Vietnam, 4.8. 2013

⋆ Ensslin, K.
Electron counting in nanostructures
Colloquium of the PTB Braunschweig, Germany, 28.8.2013

⋆ Ensslin, K.
Local investigation of ballistic transport in semiconductor nanostructures
19th International Vacuum Congress, Paris, France, 9.9.2013

⋆ Ensslin, K.
Graphene quantum devices
1st Erlangen Symposium on Synthetic Carbon Allotropes, Erlangen, Germany, 29.9.2013

⋆ Ensslin, K.
Electron counting in semiconductor nanostructures
Student seminar, Osaka University, Japan, 7.10.2013

⋆ Ensslin, K.
Imaging integer and fractional quantum Hall edge states
Swiss-Japanese Nanoscience Workshop: Materials Phenomena at Small Scale, Tsukuba, Japan, 9.10.2013

⋆ Ensslin, K.
Imaging integer and fractional quantum Hall edge states
Seminar, University of Tokyo, Japan, 11.10.2013

⋆ Ensslin, K.
Quantum point contacts in p-type GaAs
Quantum device center seminar, University of Copenhagen, Denmark, 30.10.2013

⋆ Ensslin, K.
Waren Sie schon einmal gleichzeitig an zwei verschiedenen Orten?
ETH Unterwegs, Gymnasium Brig, Switzerland, 6.11.2013

⋆ Ensslin, K.
InAs/GaSb quantum well as a candidate material for 2D topological insuators: Insulating state and giant non-local response in the quantum Hall regime
Session on “Condensed Matter Physics” of the Swiss-Kyoto Symposium, Zurich, Switzerland, 21.11.2013

⋆ Ensslin, K.
Insulating state and giant non-local response in an InAs/GaSb quantum well in the quantum Hall regime
Gordon Godfrey Workshop 2013 “Spins and Strong Electron Correlations”, Sydney, Australia, 25.11.2013

⋆ Ensslin, K.
Improving confinement in graphene quantum devices
Graphene center seminar, National Univ. of Singapore, Singapore, 28.11.2013

Filipp, S.
Interfacing Rydberg atoms with superconducting circuits
APS March Meeting, Baltimore, Maryland, USA, 19.03.2013

⋆ Filipp, S.
Circuit QED - Quantum Optics with Microwave Photons and Superconducting Circuits on a Chip
Wigner Research Center for Physics, Budapest, Hungary, 26.04.2013

⋆ Filipp, S.
Experimental Realization of Non-Abelian Non-Adiabatic Geometric Gates
Seminar fuer Neutronen-, Festkoerper- und Quantenphysik, TU Wien, Atominstitut, Austria, 07.06.2013

⋆ Filipp, S.
Geometric phases for robust quantum gates in circuit QED
Walther-Meissner-Seminar, Walther Meissner Institut Munich, Germany, 14.06.2013

⋆ Filipp, S.
Manipulating Rydberg states near superconducting chip electrodes
CCQED Conference on Resonator QED, Munich, Germany, 09.09.2013

⋆ Filipp, S.
Exploring Quantum Mechanics with Superconducting Circuits
Volkswagen-Funding Direction Meeting, Germany, 23.10.2013

⋆ Filipp, S.
Non-Abelian Geometric Gates and Shaped Photons: Exploiting Higher Superconducting Qubit Levels
Universität Innsbruck, Innsbruck, Austria, 27.11.2013

⋆ Filipp, S.
Circuit QED: Quantum optics with artificial and real atoms
Symposium on “Complex Systems at the Transition from a Quantum Mechanical to a Classical Description”,Universität Heidelberg, Kirchhoff-Institut für Physik, Heidelberg, Germany, 11.12.2013

Fognini, A.
Ultrafast loss of the classical magnetization
DPG-Frühjahrstagung, Regensburg, Germany, 10.03.2013

Häusermann, R.
Spectral Density of Trap States in Organic n-and p-type Semiconductors: Intrinsic Potential of Small Molecules and Polymers
MRS Spring Meeting, San Francisco, USA 01.04.2013

⋆ Häusermann, R
Charge traps and charge transport in organic semiconductors: Insights from quantitative studies
Seminar at Stanford University, Stanford, USA 07.04.2013

⋆ Hüvonen, D.
Effect of magnetic bond disorder on spin dynamics & field induced ordering transition in gapped spin liquids
International Symposium on Spin Waves 2013, St. Petersburg, Russia, 11.06.2013

⋆ Ihn, T.
Graphene Quantum Circuits
S3NANO Winter School "Few-spin solid-state nanosystems", Windsor, UK, 03.02.2013

⋆ Ihn, T.
Imaging interference as well as integer and fractional quantum Hall edge channels in small constrictions
Workshop on Interferometry and Interactions in Non-Equilibrium Meso- and Nano-Systems, Trieste, Italy, 08.04.2013

⋆ Ihn, T.
Imaging fractional quantum Hall edge channels
Colloquium SFB767, Konstanz, Germany, 16.05.2013

Kanter, J.
$CePt_2In_7$:Focused Ion Beam Sample Preparation for Quantum Oscillation Measurements under High Pressure
March Meeting of the American Physical Society, Baltimore, U.S.A. 18.03.2013

⋆ Kozikov, A.
Coaxial tips for local transport studies of nanostructures
Workshop on nanomechanical sensing, Stanford, Switzerland, 01.05.2013

⋆ Kozikov, A.
Coaxial tips for local transport studies of nanostructures
Stanford, USA, 06.05.2013

⋆ Kozikov, A.
Interference of electrons in backscattering through nanostructures
Stanford, USA, 08.05.2013

⋆ Kozikov, A.
Imaging magnetoelectric subbands in ballistic constrictions
Strasbourg, France, 01.10.2013

⋆ Kozikov, A.
Imaging magnetoelectric subbands in ballistic constrictions
Katowice, Poland, 29.11.2013

Krähenmann, T.
Ballistic electron transfer between quantum dots
EP2DS20, Wroclaw, Poland, 1.7.2013

⋆ Lang, C.
Hong-Ou-Mandel Experiments with Microwaves: Correlations, Indistinguishability and Entanglement
NCCR QSIT Lunch Seminar, ETH Zurich, Switzerland, 06.06.2013

Lichtenberger, A.
A kinematics concept/misconception diagnosis test
ESERA 2013, Nicosia, Cyprus, Greece, 03.09.2013

⋆ Mesot, J.
Perspectives for Science with X-rays in Europe: views from a National Laboratory
CRISP annual meeting, Paul Scherrer Institute, Villigen, Switzerland, 18.04.2013

⋆ Mesot, J.
Strongly correlated materials research at PSI
SWM13-MaNEP Workshop, Les Diablerets, Switzerland, 24.06.2013

⋆ Mesot, J.
Energy storage, podium discussion
World Energy Forum, Daegu, Rep. Korea, 13.10.2013

⋆ Mesot, J.
Strongly correlated materials research at PSI large-scale facilities: recent developments using muon, neutron and photon beams
Joint workshop, Institute of Physics (China)-PSI (CH), Beijing, 16.10.2013

Mirri, C.
Optical Excitation Spectrum in Ni- and Cu-doped $ZrTe_3$
March Meeting of the American Physical Society, Baltimore, U.S.A. 18.03.2013

Mirri, C.
Optical investigation of $Ba(Co_xFe_{1-x})_2As_2$ detwinned by tunable uniaxial applied pressure
The New Generation of Strongly Correlated Electron Systems, Sestri Levante, Italy 01.07.2013

⋆ Moll, P.J.W.
Slow Abrikosov- to fast moving Josephson-vortex transition in iron-pnictide superconductors
March Meeting of the American Physical Society, Baltimore, U.S.A. 18.03.2013

⋆ Moll, P.J.W.
FIB sample preparation for condensed matter physics: an application to pnictides
Condensed Matter Physics Seminar, UC Berkeley, USA. 04.09.2013

⋆ Moll, P.J.W.
FIB sample preparation for condensed matter physics: an application to pnictides
National High Magnetic Field Laboratory Seminar, Los Alamos, NM, USA. 12.09.2013

⋆ Moll, P.J.W.
Slow Abrikosov to fast moving Josephson vortex transition in REFeAs(O,F)
VORTEX 2013 conference, Nanjing, China 20.05.2013

Morf, T.
X-ray Induced Trap States in the Organic Semiconductor Rubrene
March Meeting of the American Physical Society, Baltimore, U.S.A. 18.03.2013

⋆ Navaretti, P.
Next-Generation Ultrasensitive Mechanical Resonators for Magnetic Resonance Force Microscopy
cQOM, Diavolezza, Switzerland, 13.02.2013

⋆ Nichele, F.
Transport experiments in InAs/GaSb double quantum wells
QSIT evaluation, Zürich, Switzerland, 1.12.2013

Nichele, F.
InAs/GaSb: A candidate topological insulator
Swiss-Kyoto Symposium, Zürich, Switzerland, 21.11.2013

⋆ Nichele, F.
Transport experiments in InAs/GaSb double quantum wells
FQMT, Prague, Czech Republic, 29.7.2013

Ott, H.-R.
Field-induced quantum soliton lattice in a frustrated two-leg spin-1/2 ladder
Swiss MaNEP workshop, Les Diablerets, Switzerland, 24.06.2013

Pascher, N.
Imaging quantum Hall edge states
Q-NET mid-term review meeting, Grenoble, France, 22.1.2013

⋆ Pascher, N.
Imaging quantum Hall edge states
QSIT meeting, Arosa, Switzerland, 22.2.2013

⋆ Pascher, N.
Imaging the conductance of integer and fractional quantum Hall edge states
IBM Zürich, 22.10.2013

Rössler, C.
GaAs Nanostructures for Single Electron Experiments
3rd NCCR QSIT General Meeting, Arosa, Switzerland, 30.01.2013

Rössler, C.
Tunable Charge Detectors for Semiconductor Quantum Circuits
EP2DS20 MSS16, Wraclaw, Poland, 01.07.2013

⋆ Rössler, C.
Non-Equilibrium Single Electron Transfer
Swiss-Japanese Nanoscience Workshop, Tsukuba, Japan, 09.10.2013

Rosskopf, T.
Using a Single Nitrogen Vacancy Center in Diamond for Nuclear Magnetic Field Sensing
PASSUGG 7062, Passugg-Araschgen, Switzerland,11.06.2013

Rosskopf, T.
Diamond Surface Paramagnetism Investigated using Spin Relaxation Measurements
QDiamond 2013 Workshop on Quantum Information using NV centers in Diamond, Huangshan, Anhui, China,

12.10.2013

S. Fält
Stacked InAs/GaAs dots for quantum information devices
17th European Molecular Beam Epitaxy Workshop, Levi, Finland, 13.3.2013

Salathé, Y.
Efficient Experimental Characterization of a Feedback Scheme for Qubit Initialization
APS March Meeting, Baltimore, Maryland, USA, 20.03.2013

Schiltz, G.
Classroom Voting on Multiple-Choice-Questions
SWITCH eduhub days 2013, St. Gallen, Switzerland, 31.01.2013

⋆ Schmidiger, D.
Physics of a strong-leg spin ladder
TUM/FRMII Festkörperphysik Seminar, Munich, Germany, 17.06.2013

Schmidiger, D.
Complete spectrum of a magnetized strong-leg spin ladder
International Conference on Neutron Scattering ICNS, Edinburgh, UK, 11.07.2013

Shiroka, T.
Strongly-disordered Heisenberg spin-1/2 chains: An NMR study
Joint European Magnetic Symposia (JEMS 2013), Rhodes, Greece, 29.08.2013

⋆ Shiroka, T.
NMR on disordered/frustrated quantum magnets
Advances in Quantum Magnets Workshop, Kolymbari, Greece, 11.09.2013

⋆ Shiroka, T.
One-dimensional spin systems in magnetic fields: from quantum disorder to magnetic-soliton lattices
CNR and Dipartimento di Fisica, E.R. Caianiello, Universita di Salerno, Salerno, Italy, 14.10.2013

⋆ Shiroka, T.
Investigating competing orders in Fe-based superconductors via μSR
Jozef Stefan Institute, Ljubljana, Slovenia, 07.11.2013

Simonet, P.
High quality graphene nanodevices
Q-NET (Quantum Nano-Electronics Training) yearly meeting, Grenoble, France, 23.01.2013

Simutis, G.
Spin Pseudogap in Ni-Doped $SrCuO_2$
The 2013 Swiss Workshop on Materials with Novel Electronic Properties, Les Diablerets, Switzerland, 25.06.2013

Steffen, L.
Realizing a Teleportation Protocol in Superconducting Circuits
QSIT Arosa Meeting, Arosa, Switzerland, 31.01.2013

Steffen, L.
Realizing a Deterministic Teleportation Protocol in Superconducting Circuits
APS March Meeting, Baltimore, Maryland, USA, 20.03.2013

⋆ Steffen, L.
Deterministic Teleportation with Feed-Forward in a Solid State System
Saturday Science Breakfast, Atomic, Mesoscopic and Optical Physics Group, Dept. of Physics , University of Cambridge, UK, 26.10.2013

T. Tschirky
2D topological insulators in the InAs/GaSb system
Swiss-Kyoto Symposium, Zürich, Schweiz, 22.11.13

Tao, Y.
Single-Crystal Diamond Nanolithography
QDiamond 2013 Workshop on Quantum Information using NV centers in Diamond, Huangshan, Anhui, China, 12.10.2013

Thede, M.
Ordering in weakly coupled random singlet spin chains
APS March Meeting 2013, Baltimore, USA, 19.03.2013

Varlet, A.
Towards dual-gated bilayer graphene nanostructures
S3Nano meeting with industry, Delft, Netherlands, 11.7.2013

Varlet, A.
Dual-gated bilayer graphene nanodevices: confinement and interferences
S3Nano mid-term meeting, Basel, Switzerland, 10.11.2013

⋆ Vaterlaus, A.
Be strong be “wrong”
Promotionsfeier der ETH Zürich, Zürich, Switzerland, 05.07.2013

⋆ Vaterlaus, A.
Schnell speichern - physikalische Grenzen der Datenspeicherung
ETH Unterwegs, Kantonsschule Reussbühl, Luzern, 20.02.2013
und Technikwoche von IngCH, Kantonsschule Burggraben, St. Gallen, 15.02.2013

⋆ Vaterlaus, A.
Rastertunnel-Mikroskopie
Vortrag vor Schülerinnen und Schülern der Kantonsschule Zug, ETH Zürich, Switzerland, 03.09.2013

⋆ Wachter, P.
Localized versus itinerant: towards the limits
43. Journees des Actinides, Sestri Levante, Italy, 07.04.2013

Wagner, C.
Simulation of conceptual change
ESERA 2013, Nicosia, Cyprus, Greece, 04.09.2013

Wagner, C.
Ziele, Überprüfung, Unterricht - die Reihenfolge machts
Konstanzer Wissenschaftsforum, Universität Konstanz und PH Thurgau, Germany, 12.07.2013

Wagner, C.
Kompetenzorientierte Prüfungen
Konstanzer Wissenschaftsforum, Universität Konstanz und PH Thurgau, Germany, 12.07.2013

Wagner, C.
Kompetenzen im Kontext und selbstorganisiertes Lernen
Tagung Bildungsraum Nordwestschweiz, Switzerland, 11.11.2013

Wagner, C.
Projektunterricht und selbstorganisiertes Lernen
Tagung Bildungsraum Nordwestschweiz, Switzerland, 11.11.2013

⋆ Wallraff, A.
Quantum Optics with Propagating Microwave Photons
Physics Colloquium, ENS Paris, France, 17.01.2013

⋆ Wallraff, A.
Exploring Quantum Physics with Superconducting Circuits
24. Edgar Luescher Seminar 2013, Klosters, Switzerland, 04.02.2013

⋆ Wallraff, A.
Exploring the Physics of Superconducting Qubits Strongly Coupled to Microwave Frequency Photons
DPG Spring Meeting, Symposium on Strong Coupling in Solid State Quantum Systems, Regensburg, Germany, 10.03.2013

⋆ Wallraff, A.
Realizing a Deterministic Teleportation Protocol in Superconducting Circuits
Département de Physique, Faculté des Sciences, Université de Sherbrooke, Canada, 25.03.2013

⋆ Wallraff, A.
Cavity Quantum Electrodynamics with Superconducting Circuits
Quantum Physics and Time Measurement by Serge Haroche, College de France, Paris, France, 09.04.2013

⋆ Wallraff, A.
Realizing a Deterministic Teleportation Protocol in Superconducting Circuits
SCALEQIT, RWTH Aachen, Germany, 15.04.2013

⋆ Wallraff, A.
Realizing a Deterministic Teleportation Protocol in Superconducting Circuits
Quantum Cavities 2013 (QC13), Canadian Institute for Advanced Research (CIFAR), Montreal, Canada, 02.05.2013

⋆ Wallraff, A.
Realization of Deterministic Quantum Teleportation with Solid State Qubits
DIAMANT: Artificial Atoms: from Quantum Physics to Applications, Hungarian Academy of Sciences, Budapest, Hungary, 20.05.2013

⋆ Wallraff, A.
Quantum Optics with Propagating Microwave Photons
YES meeting of the EU International Training Network Circuit and Cavity Quantum Electrodynamics (CCQED), ETH Zurich, Zurich, Switzerland, 04.06.2013

⋆ Wallraff, A.
Photon-Qubit Entanglement and Hong-Ou-Mandel Interference at Microwave Frequencies
Oxford University, invited by Peter Leek, Oxford University, U.K., 06.06.2013

⋆ Wallraff, A.
Circuit Quantum Electrodynamics
Introduction to Quantum Systems and Devices, Nuuksio National Park, Finnland, 11.06.2013

⋆ Wallraff, A.
Exploring Hybrid Quantum Systems using Superconducting Circuits
SFB/TRR 21 Colloquium, Physikalisches Institut, Experimentalphysik II, Universität Tübingen, Germany, 05.07.2013

⋆ Wallraff, A.
Quantum Optics with Microwave Photons
2nd International Conference on Quantum Technologies (ICQT 2013), Russian Quantum Center, Moscow, Russia, 15.07.2013

⋆ Wallraff, A.
Deterministic Quantum Teleportation with Feed-Forward in a Solid State System
2nd International Conference on Quantum Technologies (ICQT 2013), Russian Quantum Center, Moscow, Russia, 20.07.2013

⋆ Wallraff, A.
Exploring Quantum Properties of Propagating Microwave Photons
Progress In Electromagnetics Research Symposium (PIERS) 2013, Stockholm, Sweden, 12.08.2013

⋆ Wallraff, A.
Exploring Quantum Physics with Superconducting Circuits
CoQuS Summer School 2013, Quantum Foundations and Manipulations, Atominstitut TU Wien, Austria, 02.09.2013

⋆ Wallraff, A.
Teleportation in a Solid State System
Chalmers University of Technology, Department of Microtechnology and Nanoscience-MC2,Goeteborg,Sweden, 13.09.2013

⋆ Wallraff, A.
Deterministic Teleportation in Solid State Circuits
Departement Physik, Universität Basel, Switzerland, 20.09.2013

⋆ Wallraff, A.
Deterministic Quantum Teleportation with Feed-Forward in a Solid State System
QCCC Workshop, Munich, Germany,17.10.2013

⋆ Wallraff, A.
Waveguide QED with an Ensemble of Two-Level Systems
THEO MURPHY INTERNATIONAL SCIENTIFIC MEETING: Many body quantum optics and correlated states of

light, The Royal Society at Chicheley Hall, home of the Kavli Royal Society International Centre, Buckinghamshire, U.K., 28.10.2013

⋆ Wallraff, A.
From single photon detection to teleportation with microwave frequency electronic circuits
Swiss-Kyoto Symposium 2013, ETH Zurich, Zurich, Switzerland, 21.11.2013

⋆ Wallraff, A.
Quantum Microwave Photonics
Quantum Superconducting Circuits and Beyond, Yale University, New Haven CT, USA, 13.12.2013

⋆ Wegscheider, W.
Engineering of Quantum States Protected by Topology: Perspectives from a Crystal Growers Point of View
Symposium on Quantum Hall Effects and Related Topics, MPI, Stuttgart, Germany, 28.6.2013

⋆ Wegscheider, W.
Quantum States Protected by Topology: Quantum Hall Effects, Topological Quantum Computing and Majorana Fermions
Physical Colloquium, Bremen, Germany, 30.5.2013

⋆ Wegscheider, W.
Highest Purity III/V-compound Semiconductors: Perspectives for Engineering of Quantum States Protected by Topology
MRS 2013 Fall Meeting, Warsaw, Poland, 16.9.2013

⋆ Zheludev, A.
Quantum magnetism
28th workshop on Novel Materials and Superconductors, Planneralm, Austria, 09.02.2013

⋆ Zheludev, A.
The quantum spin ladder: solved!
Colloquium, International Center for Theoretical Physics, Trieste, Italy, 20.02.2013

⋆ Zheludev, A.
The end of the quantum spin ladder problem
Seminar, Physics Department, University of Nijmegen, Netherlands, 30.05.2013

⋆ Zheludev, A.
The end of the quantum spin ladder problem
Seminar, Physics Department, University of Zurich, Switzerland, 16.10.2013

⋆ Zheludev, A.
There ain't no such thing as a magnetic Bose glass
LOTHERM Workshop, Quantum Magnets 2013: Advances in quantum magnets-dynamics, Colymbari, Crete, Greece, 09.09.2013

⋆ Zheludev, A.
Full spectrum of a magnetized quantum spin ladder
JAEA Symposium, Magnetism in Quantum Beam Science, SPring-8, Japan, 11.03.2013

Zhigadlo, N.
Improved growth of Ln1111 superconducting crystals from NaAs/KAs flux
March Meeting of the American Physical Society, Baltimore, U.S.A. 18.03.2013

⋆ Zhigadlo, N.
Improved growth of Ln1111 oxypnictides: tuning structural and physical properties via doping and pressure
Int. Conference Superstripes 2013 “Quantum in Complex Matter”, Ischia, Italy 27.05.2013

Zhigadlo, N.
Recent progress in crystal growth and characterization of 1111 type iron-based superconductors
8^{th} Int.Conference in School Format on “Vortex Matter in Nanostructured Superconductors” Rhodes, Greece 21.09.2013

⋆ Zhigadlo, N.
Crystal growth under extreme conditions
Leibniz-Institute for Solid State and Materials Research, IFW-Dresden, Germany 19.12.2013

⋆ von Känel, H.
3D heteroepitaxy of mismatched semiconductors on silicon
8^{th} Int.Conference on Silicon Epitaxy and Heterostructures (ICSI-8), Fukuoka, Japan, 03.06.2013

⋆ von Känel, H.
X-ray nanodiffraction on epitaxial crystals
4^{th} Int. Conference from Nanoparticles and Nanomaterials to Nanodevices and Nanosystems (IC4N), Korfu, Greece 16.06.2013

⋆ von Känel, H.
Epitaxial Ge-crystal arrays for X-ray detection
15^{th} Int. Workshop on Radiation Imaging Detectors (iWoRID2013), Paris, France, 23.06.2013

⋆ von Känel, H.
Three-dimensional heteroepitaxy on deeply patterned silicon substrates
Seminar am IHP (Innovations for High Performance Microelectronics), Frankfurt(Oder),Germany, 09.12.2013

⋆ von Känel, H.
Three-dimensional heteroepitaxy on deeply patterned silicon substrates
Seminar STMicroelectronics, Agrate, Italy, 13.12.2013

12.2 Posters

Allan, M.
Towards Quantum Simulations with Circuit QED
Many body quantum optics and correlated states of light, The Royal Society at Chicheley Hall, home of the Kavli Royal Society International Centre, Buckinghamshire, 28.10.2013

Baer, S.
Fractional quantum Hall states confined to quantum point contacts
QSIT evaluation, Zurich, Switzerland, 02.12.2013

Baer, S.
Magneto-transport in clean quantum point contacts
QH Symposium, Stuttgart, Germany, 26.06.2013

Barraud, C.
Towards graphene quantum structures with reduced disorder
QSIT general meeting, Arosa, Switzerland, 30.01.2013

Basset, J.
Single electron charge q-bit in a circuit QED architecture
QSIT general meeting, Arosa, Switzerland, 30.01.2013

Berger, S.
Exploring the Effect of Noise on Geometric Phases
CCQED Conference on Resonator QED, Munich, Germany, 09.09.2013

Butti, P.
Efficiency of graphene based rectifiers
Workshop on nanostructured graphene, Antwerp, Belgium, 21.05.2013

C. Charpentier
Al(Ga)Sb/InAs based heterostructures: growth, transport and optical experiments
3rd NCCR QSIT General Meeting, Arosa, Switzerland, 01.02.2013

C. Charpentier
Antimony based III-V semiconductor heterostructures
International Symposium on Quantum Hall Effects and Related Topics, Stuttgart, Germany, 28.06.2013

C. Charpentier
High-purity III-V materials for two-dimensional topological insulators
Deutscher MBE-Workshop 2013, Dresden, Germany, 01.10.2013

Dusza, A.
Optical investigation of $Ba(Co_xFe_{1-x})_2As_2$ detwinned by tunable uniaxial applied pressure
2013 Swiss Workshop on Materials with Novel Electronic Properties, Les Diablerets, Switzerland 24.06.2013

Eichler, C.
Exploring quantum microwave radiation emitted from superconducting circuits
Quantum Cavities 2013 (QC13), Canadian Institute for Advanced Research (CIFAR), Montreal, Canada, 02.05.2013

Fognini, A.
Ultrafast magneto-dynamics: A pathway to ultrafast spintronics
Spintech VII, Chicago, USA, 29.07.2013

Kanter, J.
Electric Transport Measurements on Micro-Structured $CePt_2In_7$ Single Crystals in a Diamond Anvil Cell
Manep Swiss Workshop, Les Diablerets, Switzerland 24.06.2013

Kozikov, A.
Imaging magnetoelectric subbands in ballistic constrictions
Symposium on Quantum Hall Effects and Related Topics, Stuttgart, Germany, 26.06.2013

Kozikov, A.
Imaging magnetoelectric subband depopulation in ballistic constrictions
EP2DS, Wroclaw, Poland, 01.07.2013

Krähenmann, T.
Conditional measurements of semiconductor quantum dots
Winter School of S^3 nano EU network, London, United Kingdom, 03.02.2013

Kreiliger, Th.
Towards Ge X-ray detector monolithically integrated on Si CMOS chip
E-MRS spring meeting, Strasbourg, France 27.05.2013

Lichtenberger, A.
A kinematics diagnosis test as an element of formative assessment
ICPE 2013, Prague, Czech Republic, 05.08.2013

Loretz, M.
NMR experiments with a nitrogen vacancy spin sensor
QSIT Site Visit, ETH Zürich, 02.12.2013

Mirri, C.
Optical investigation of $Ba(Co_xFe_{1-x})_2As_2$ detwinned by tunable uniaxial applied pressure
March Meeting of the American Physical Society, Baltimore, U.S.A. 18.03.2013

Mlynek, J.
The bad cavity regime in circuit QED
NCCR-QSIT Meeting 2013, Arosa, Switzerland, 31.01.2013

Navaretti, P.
Improvements to ultrasensitive mechanical resonators
QSIT Site Visit, ETH Zürich, 02.12.2013

Nichele, F.
Spin-splitting and effective masses in p-type GaAs
EP2DS, Wroclaw, Poland, 01.07.2013

Nichele, F.
Al(Ga)Sb/InAs based heterostructures: growth,transport and optical experiments
QSIT general meeting, Arosa, Switzerland, 30.01.2013

Pascher, N.
Scanning gate experiments on semiconductor quantum structures
QSIT meeting, Arosa, Switzerland, 22.02.2013

Pascher, N.
Imaging Integer and Fractional Quantum Hall Edge States
Symposium on Quantum Hall Effects and Related Topics, Stuttgart, Germany, 26.06.2013

Pascher, N.
Imaging Integer and Fractional Quantum Hall Edge States
EP2DS, Wroclav, Poland, 01.07.2013

Puebla-Hellmann, G.
GHz Frequency Properties of Single Walled Carbon Nanotubes
NCCR-QSIT Meeting 2013, Arosa, Switzerland, 30.01.2013

Rössler, C.
GaAs Nanostructures for Single Electron Experiments
QSIT general meeting, Arosa, Switzerland, 30.01.2013

Rössler, C.
Ballistic electron transfer between quantum dots
Symposium on Quantum Hall Effects and Related Topics, Max Planck Institute for Solid State Research, Stuttgart, Germany, 26.06.2013

S. Fält
Entanglement and coherence of quantum dot spin qubits
3rd NCCR QSIT General Meeting, Arosa, Switzerland, 31.01.2013

Schiltz, G.
Mobile Lab Classes
International Conference on Physics Education (ICPE 2013), Prague, 06.08.2013

Schiltz, G.
Mobile Labs and Mobile Lab Classes
World Conference on Science and Technology Education, WorldSTE2013, Kuching, Malaysia, 30.09.2013

Simonet, P.
Hybrid graphene-GaAs nanostructures
EP2DS (Electronic Properties of 2-dimensional Systems), Wroclaw, Poland, 01.07.2013

Stammeier, M.
Driving Rydberg-Rydberg Transitions with Microwave Cavities
RQI Winterschool Obergurgl, Austria, 10.02.2013

Stammeier, M.
Hybrid Cavity QED in 3D Cavities with Rydberg Atoms and Superconducting Qubits
Conference on Resonator QED, Munich, Germany, 09.09.2013

Steffen, L.
Quantum Teleportation with Superconducting Qubits
NCCR-QSIT Meeting 2013, Arosa, Switzerland, 30.01.2013

Steinacher, R.
Scanning gate investigation of electron transport through ballistic cavities
Swiss Nano-Convention, Basel, Switzerland, 23.05.2013

Stockklauser, A.
Circuit Quantum Electrodynamics with Semiconductor Single-Electron Charge Qubits
CCQED Conference on Resonator QED, Munich, Germany, 09.09.2013

Tschirky. T.
MBE growth of Antimony based semiconductor heterostructures
QSIT Junior Meeting 2013, Passugg, Switzerland, 12.06.2013

Thiele, T.
Coherent Manipulation of Rydberg States Above Surfaces at Cryogenic Temperatures
NCCR QSIT Review Meeting, Arosa, Switzerland, 30.01.2013

Thiele, T.
Towards Driving Rydberg-Rydberg Transitions from a Coplanar Microwave Waveguide in a Cryogenic Environment
CCQED Conference on Resonator QED, Munich, Germany, 09.09.2013

Varlet, A.
Improving confinement in graphene nanostructures
QSIT General Meeting, Arosa, Switzerland, 05.02.2014

Varlet, A.
Towards graphene quantum nanostructures with reduced disorder
QSIT General Meeting, Arosa, Switzerland, 31.01.2013

Varlet, A.
Electronic transport in gate-defined graphene nanostructures
S3Nano Winter School, Windsor, UK, 03.02.2013

Varlet, A.
Electronic transport in gate-defined bilayer graphene nanostructures
Graphene week, Chemnitz, Germany, 02.06.2013

W. Wüster
Light-matter interaction between a two-dimensional electron gas and a micro-cavity
International Symposium on Quantum Hall Effects and Related Topics, Stuttgart, Germany, 28.06.2013

W. Wüster
Light-matter interaction between a two-dimensional electron gas and a micro-cavity
20th International Conference on Electronic Properties of Two-Dimensional Systems (EP2DS-20), Wroclaw, Poland,

05.07.2013

Wagner, C.
Agent Based Simulation of Group Work Performance
ICPE 2013, Prague, Czech Republic, 05.08.2013

Zhigadlo, N.
Improved growth of Ln1111 crystals from NaAs/KAs flux
Swiss Workshop on Materials with Novel Electronic Properties, Les Diablerets, Switzerland, 24.06.2013